



**CHARACTERIZATION OF COMPRESSIVE CREEP BEHAVIOR OF  
OXIDE/OXIDE COMPOSITE WITH MONAZITE COATING  
AT ELEVATED TEMPERATURE**

THESIS

Patrick R. Jackson, 2nd Lt, USAF

AFIT/GAE/ENY/06-M17

**DEPARTMENT OF THE AIR FORCE  
AIR UNIVERSITY**

**AIR FORCE INSTITUTE OF TECHNOLOGY**

---

---

**Wright-Patterson Air Force Base, Ohio**

APPROVED FOR PUBLIC RELEASE; DISTRIBUTION UNLIMITED

The views expressed in this thesis are those of the author and do not reflect the official policy or position of the United States Air Force, Department of Defense, or the U.S. Government.

**CHARACTERIZATION OF COMPRESSIVE CREEP BEHAVIOR OF  
OXIDE/OXIDE COMPOSITE WITH MONAZITE COATING  
AT ELEVATED TEMPERATURE**

THESIS

Presented to the Faculty  
Department of Aeronautics and Astronautics  
Graduate School of Engineering and Management  
Air Force Institute of Technology  
Air University  
Air Education and Training Command  
In Partial Fulfillment of the Requirements for the  
Degree of Master of Science in Aeronautical Engineering

Patrick R. Jackson, BS

2nd Lt, USAF

March 2006

APPROVED FOR PUBLIC RELEASE; DISTRIBUTION UNLIMITED

**CHARACTERIZATION OF COMPRESSIVE CREEP BEHAVIOR OF  
OXIDE/OXIDE COMPOSITE WITH MONAZITE COATING  
AT ELEVATED TEMPERATURE**

Patrick R. Jackson, BS

2nd Lt, USAF

Approved:

/signed/

Dr. Marina Ruggles-Wrenn (Chairman)  
/signed/

\_\_\_\_\_ Date

Dr. Robert Canfield (Member)  
/signed/

\_\_\_\_\_ Date

Dr. Theodore Nicholas (Member)

\_\_\_\_\_ Date

## **Abstract**

Ceramic-matrix composites (CMCs), capable of maintaining excellent strength and fracture toughness at high temperatures are prime candidate materials for aerospace turbine engine applications. In these applications, CMCs will be subjected to mechanical loading in complex environments. Before ceramic matrix composites can be used in high-temperature aerospace engine applications, their structural integrity and long-term environmental durability must be assured. This research investigated compressive stress-strain and compressive creep behavior of the N610/M/A at 900 and 1100 °C. The composite consists of a porous alumina matrix reinforced with Nextel<sup>TM</sup>610 fibers coated with monazite in a symmetric cross-ply (0°/90°/0°/90°)<sub>s</sub> orientation. The addition of monazite coating resulted in loss of compressive strength at both 900 and 1100 °C. Compressive creep behavior was examined at 900 and 1100°C for creep stresses ranging from 50 to 95 MPa. At 900 °C both monazite containing and control specimens produced creep strains ≤ 0.05%. Conversely, at 1100 °C creep strains approached 9%. Creep strain rates were on the order of  $10^{-7}$  s<sup>-1</sup>. Creep run-out, defined as 100 h at creep stress, was achieved in all tests. Composite microstructure, as well as damage and failure mechanisms were investigated. Furthermore, effects of variation in microstructure on mechanical response were examined. While differences in processing and consequently the composite microstructure did not have a significant effect on tensile response of the CMC, effects on the compressive properties were dramatic.

## **Acknowledgements**

I would like to thank Dr. Marina Ruggles-Wrenn for her extensive support and guidance during the entire course of this investigation. Her help was invaluable. I would like to thank Dr. Seungsu Baek for his help preparing cross-sections and his professional assistance analyzing the microstructures. I would like to thank Kristi Keller (AFRL/MLLN) for providing the testing materials, helping obtain some of the SEM images seen in this document, and providing expert opinions on the subject. Much thanks to Dr. Ronald Kerans (AFRL/MLLN) and Dr. Triplicane Parthasarathy (AFRL/MLLN) for their expert opinions and guidance during the course of this work. I would also like to thank Dr. Ronald Kerans, Dr. Joseph. Zelina (AFRL/PRTC), and Dr. Ruth L. Sikorski for sponsoring this research and Barry Page, Andy Pitts, and Jay Anderson for their technical assistance with all the lab equipment. Next I would like to thank Captain John Mehrman and Second Lieutenant John Balaconis for all their help and for keeping me sane during the entire course of this work. Finally, I would like to thank my family, my friends back in Colorado, and all the new friends I have made out here in Ohio for all their support.

## Table of Contents

	Page
<b>Abstract</b> .....	iv
<b>Acknowledgements</b> .....	v
<b>Table of Contents</b> .....	vi
<b>List of Figures</b> .....	viii
<b>List of Tables</b> .....	xiii
<b>I. Introduction</b> .....	1
<b>II. Background</b> .....	3
2.1 Ceramic Matrix Composites .....	3
2.1.1 Fibers.....	3
2.1.2 Matrix.....	4
2.1.3 Interphase.....	6
2.1.4 All-Oxide CMCs.....	9
2.1.5 Fabrication of CMCs.....	11
2.2 Aerospace Applications .....	12
2.3 Tensile vs. Compressive Failure Mechanisms.....	13
2.4 Previous Work .....	16
2.4.1 Off-Axis Behavior of CMCs.....	17
2.4.2 Compression .....	18
2.5 Thesis Objective.....	18
<b>III. Material and Specimen</b> .....	20
3.1 N610/Monazite/Alumina and N610/Alumina Composites.....	20
3.1.1 Nextel <sup>TM</sup> 610 Fiber. ....	20
3.1.2 Alumina Matrix.....	21
3.1.3 Monazite Coating.....	22
3.2 Specimen Development .....	22
3.2.1 Material Processing.....	22
3.2.2 Panel Specifications .....	24
3.2.3 Specimen Geometry.....	26
3.2.3.1 Tensile Specimens .....	26
3.2.3.2 Compressive Specimens .....	27
3.2.4 Specimen Tabbing .....	27

	Page
<b>IV. Experimental Set-Up and Testing Program.....</b>	<b>29</b>
4.1 Test Equipment .....	29
4.1.1 Testing System and Components.....	29
4.1.2 Specimen Components.....	36
4.2 Temperature Calibration .....	36
4.3 Test Procedures.....	37
4.3.1 Monotonic Tension Tests.....	38
4.3.2 Monotonic Compression Tests .....	39
4.3.3 Creep Rupture Tests.....	39
4.4 Post Failure Analysis .....	40
4.4.1 Specimen Preparation .....	40
4.4.2 Optical Microscopy.....	41
4.4.3 Scanning Electron Microscope Analysis.....	44
<b>V. Results and Discussion.....</b>	<b>46</b>
5.1 Fiber Volume Ratio Adjustment.....	46
5.2 Monotonic Tension – $\pm 45^\circ$ Specimens .....	46
5.3 Monotonic Compression – Dogbone-Shaped Specimens, $0^\circ/90^\circ$ Fiber Orientation .....	48
5.4 Monotonic Compression – Straight-Sided Specimens, $0^\circ/90^\circ$ Fiber Orientation ..	52
5.5 Microscopy .....	56
5.5.1 Specimens Tested in Tension.....	56
5.5.2 Specimens Tested in Compression .....	59
5.6 Compressive Creep Behavior .....	67
5.6.1 Effect of Stress Level and Temperature.....	67
5.6.2 Creep Strain Rate as a Function of Applied Stress .....	70
5.6.3 Compressive Versus Tensile Creep Behavior.....	71
5.6.4 Retained Properties .....	72
5.7 Microstructural Analysis of N610/Monazite/Alumina Panel M2.....	75
5.7.1 Stress-Strain Behavior.....	76
5.7.2 Panel M1 and Panel M2 Composite Microstructure.....	77
5.7.3 Montonic Tensile Behavior.....	84
5.8 Composite Microstructure .....	86
5.8.1 Fracture Surfaces .....	86
5.8.2 Microstructure of N610/Alumina Composite .....	89
<b>VI. Observations and Conclusions .....</b>	<b>91</b>
6.1 Observations .....	91
6.2 Conclusions.....	92
<b>Bibliography .....</b>	<b>93</b>

## List of Figures

	Page
Figure 1. “Schematics of the Damage Processes that Enable Damage Tolerance in a) Conventional Dense-Matrix Weak-Interface CMC and b) Porous Matrix CMCs Without Fiber Coatings” [43:15]. .....	6
Figure 2. Monazite Coating is the Bright Areas in the Pictures. (a) Shows Fiber Bridging and (b) Shows Incomplete Fiber Coverage [14:584]. .....	9
Figure 3. Schematic Representation of Oxidation Progression through Matrix Crack of CMC with Fiber Coating .....	10
Figure 4. Schematic of Matrix Cracking and Local Stress Distributions in Composite..	14
Figure 5. Schematic of Microbuckling, which Leads to Excessive Deformation in Ductile Fibers or Fracture Planes in Brittle Fibers .....	15
Figure 6. Schematic of Shear Failure Mode of Unidirectional Composite Under Longitudinal Compression.....	15
Figure 7. Schematic of Transverse of Splitting of Unidirectional Composite Under Longitudinal Compression.....	16
Figure 8. Schematic of $(0^\circ/90^\circ/0^\circ/90^\circ)_s$ Fiber Orientation .....	24
Figure 9. Tensile Specimen.....	26
Figure 10. Compression Specimen .....	27
Figure 11. Tabbed Compressive and Tensile Specimens, Respectively.....	28
Figure 12. 25kN Servo Hydraulic Machine .....	30
Figure 13. Chiller and Controller.....	30
Figure 14. Tubes for Cooling Water Connected to Hydraulic Wedge Grips.....	31
Figure 15. Oven Glows at High Temperatures .....	32
Figure 16. Interior View of Oven Half .....	32
Figure 17. Temperature Controller .....	33
Figure 18. Extensometer Equipped with Alumina Rods .....	34

	Page
Figure 19. Extensometer Mounted Behind the Heat Shield .....	34
Figure 20. Multipurpose Testware Procedure for Creep Testing at Elevated Temperatures .....	35
Figure 21. Specimen Equipped with Anti-Buckling Device .....	36
Figure 22. Tensile Specimen Secured in the Grips of the Servo-Hydraulic Machine .....	38
Figure 23. Pieces of Specimen Mounted in Conductive Resin.....	40
Figure 24. Polishing machine .....	41
Figure 25. Optical Microscope .....	42
Figure 26. Side View of Specimen .....	43
Figure 27. Surface View of Specimen .....	44
Figure 28. Scanning Electron Microscope.....	45
Figure 29. Tensile Stress-Strain Curves for N610/Monazite/Alumina and N610/Alumina Ceramic Composites with $0^\circ/90^\circ$ and $\pm 45^\circ$ Fiber Orientation. Data from References [34,38] are Also Shown. ....	47
Figure 30. Monotonic Tensile/Compressive Behavior of On-Axis Dogbone-Shaped Specimens at $900\text{ }^\circ\text{C}$ .....	49
Figure 31. N610/Monazite/Alumina Specimen Tested in Compression at $900\text{ }^\circ\text{C}$ Shows an Asymmetric Fracture Surface Suggesting Possible Buckling.....	50
Figure 32. Specimen Tested in Compression with Anti-Buckling Device.....	51
Figure 33. Tensile and Compressive Stress-Strain Curves for N610/Monazite/Alumina at $23\text{ }^\circ\text{C}$ . Compression Test Employed Anti-Buckling Device. ....	51
Figure 34. Compression Stress-Strain Curves for N610/Monazite/Alumina and N610/Alumina at $900\text{ }^\circ\text{C}$ .....	53
Figure 35. Side 1 of N610/Monazite/Alumina Specimen Asymmetric Fracture Suggests Buckling.....	55
Figure 36. Side 2 of N610/Monazite/Alumina Specimen Asymmetric Fracture Suggests Buckling.....	55

Figure 37. N610/Monazite/Alumina Specimens with $\pm 45^\circ$ Fiber Orientation Tested in Monotonic Tension at 900 °C .....	56
Figure 38. N610/Alumina Specimens with $\pm 45^\circ$ Fiber Orientation Tested in Monotonic Tension at 900 °C .....	57
Figure 39. N610/Monazite/Alumina Specimen with 0°/90° Fiber Orientation Tested in Tension at 900 °C .....	58
Figure 40. Dogbone-Shaped N610/Monazite/Alumina Specimen with 0°/90° Fiber Orientation Tested in Compression at 900 °C without the Anti-Buckling Device .....	59
Figure 41. Dogbone-Shaped N610/Monazite/Alumina Specimen with 0°/90° Fiber Orientation Tested in Compression at 900 °C without the Anti-Buckling Device .....	60
Figure 42. Dogbone-Shaped N610/Monazite/Alumina Specimen with 0°/90° Fiber Orientation Tested in Compression with the Anti-Buckling Device at 23 °C .....	61
Figure 43. Straight-Sided N610/Monazite/Alumina 0°/90° Specimen Tested in Compression at 900 °C .....	62
Figure 44. Side Views of a Straight-Sided N610/Monazite/Alumina 0°/90° Specimen Tested in Compression at 900 °C .....	62
Figure 45. Straight-Sided N610/Monazite/Alumina 0°/90° Specimen Tested in Compression at 1100 °C .....	63
Figure 46. Side Views of the Straight-Sided N610/Monazite/Alumina 0°/90° Specimen Tested in Compression at 1100 °C .....	64
Figure 47. Straight-Sided N610/Alumina 0°/90° Specimen Tested .....	65
Figure 48. Straight-Sided N610/Alumina 0°/90° Specimen Tested in Compression at 1100 °C .....	66
Figure 49. Compressive Creep Strain as a Function of Time for N610/Monazite/Alumina and N610/Alumina Composites at 1100 °C .....	68
Figure 50. Compressive Creep Strain as a Function of Time for N610/Monazite/Alumina and N610/Alumina Composites at 900 °C .....	69
Figure 51. Compressive Creep Strain Rates as a Function of Applied Stress for N610/Monazite/Alumina and N610/Alumina Composites at 1100 °C .....	70

Figure 52. Creep Curves for N610/Monazite/Alumina Composite at 1100 °C: (a) Compressive Creep and (b) Tensile Creep [34,38].....	72
Figure 53. Effects of Prior Compressive Creep at 1100 °C on Compressive Stress-Strain Behavior of N610/Monazite/Alumina Ceramic Composite .....	73
Figure 54. Effects of Prior Compressive Creep at 1100 °C on Tensile Stress-Strain Behavior of N610/Monazite/Alumina Ceramic Composite .....	75
Figure 55. Compressive Stress-Strain Curves for N610/Monazite/Alumina Specimens from Panels M2 and M3 at 900 °C .....	76
Figure 56. Schematic of Specimen Showing the Type of Cuts made to.....	78
Figure 57. Parallel Cross-Sectional View of Virgin Specimen from Panel M2 .....	79
Figure 58. Backscatter SEM Image of Cross-Section of Panel M2 Showing Matrix-Rich Areas and Large Regions Void of Matrix Material in the 90° Fiber Layer. Bright White Areas on Both Fiber Layers are Monazite Coating. ....	79
Figure 59. Parallel Cross-Sectional View of Virgin Specimen from Panel M1 .....	80
Figure 60. Propagation of Crack through a Specimen from Panel M1 .....	81
Figure 61. Magnified View of a Fracture Surface from Panel M1 Showing Cracks Initiating and Self-arresting in 90° fiber layers .....	81
Figure 62. Crack Propagation through Fibrous 90° Layers of a Specimen from Panel M2. ....	82
Figure 63. Magnified View of a Fracture Surface from Panel M2 Showing Cracks Propagating through 90° Fiber Layers. No Crack Deflection is Observed.....	82
Figure 64. Backscatter SEM Image of Fracture Surface Shown in Figure 62.....	83
Figure 65. Backscatter SEM Images of Representative Crack Propagation in specimens from Panel M1 (a) and Panel M2 (b and c) .....	84
Figure 66. Tensile Stress-Strain Curves for N610/Monazite/Alumina Panels M2 and M3 at 900 °C .....	85
Figure 67. Fracture surfaces of N610/Monazite/Alumina Specimen Tested in Compression-to-Failure at 1100 °C after having achieved a Creep Run-Out at 75 MPa at 1100 °C .....	87

Figure 68. Side View of Fracture Surfaces of a N610/Monazite/Alumina Specimen Tested in Compression-to-Failure at 1100 °C after having achieved a Creep Run-Out at 75 MPa at 1100 °C .....	87
Figure 69. Fracture surfaces of N610/Monazite/Alumina Specimen Tested in Compression-t-Failure at 1100 °C after having achieved a Creep Run-Out at 65 MPa at 1100 °C .....	88
Figure 70. Side View of Fracture Surfaces of a N610/Monazite/Alumina Specimen Tested in Compression-to-Failure at 1100 °C after having achieved a Creep Run-Out at 65 MPa at 1100 °C .....	89
Figure 71. Schematic of Sections Removed from Specimen for Analysis .....	90
Figure 72. Micrograph of N610/Alumina Ceramic Composite. Virgin Material is on the Far Left Followed by Sections of the Specimen Tested in Compressive Creep at 1100 °C. .....	90

## List of Tables

	Page
Table 1. Nextel™ 610 Fiber Properties [1,2] .....	21
Table 2. Fiber Volume Fraction and Density of Panels Used for Compression Tests. ...	25
Table 3. Monotonic Properties of On-Axis and Off-Axis Specimens. V <sub>f</sub> Stands for Fiber Volume Fraction. ....	48
Table 4. Tensile and Compressive Properties of N610/Monazite/Alumina at 900 °C ....	49
Table 5. Tensile and Compressive Properties of N610/Monazite/Alumina at 23 °C. Compression Test Employed Anti-Buckling Device.....	52
Table 6. Compressive Properties of Straight-Sided N610/Monazite/Alumina and N610/Alumina Specimens at 900 and 1100 °C .....	54
Table 7. Retained Properties of N610/Monazite/Alumina Specimens Subjected to Prior Creep at 1100 °C .....	74
Table 8. Compressive Properties of N610/Monazite/Alumina Ceramic Composites ....	77

# **CHARACTERIZATION OF COMPRESSIVE CREEP BEHAVIOR OF OXIDE/OXIDE COMPOSITE WITH MONAZITE COATING AT ELEVATED TEMPERATURE**

## **I. Introduction**

Records of composites date back to Biblical times when straw was used to reinforce clay bricks. Since then man has been using forms of fiber and particle reinforced materials in all sorts of applications. Today, composites can be found almost everywhere and in everything.

The aerospace industry has benefited greatly from the development of composites. Aircraft have been outfitted with composite materials since the 1950s because their high strength-to-weight ratio, low life-cycle cost, and maintainability have made them ideal for use in aviation [12:4-9]. Today, more advanced composites are available, which continue to be ideal materials for the aerospace industry. In fact, the B-2 stealth bomber was made almost entirely of composite materials [12:7].

The latest developments in composites rest in newer metal matrix, ceramic matrix, and carbon/carbon composites for high temperature applications. These materials are of greatest interest to the aerospace industry, which requires not only their ability to withstand high temperatures, but their low weight and high strength properties as well. In the 1990s, the use of these materials in oxidizing environments for long periods of time

prompted the development of a new type of ceramic matrix composite (CMC) that could withstand these conditions [39:1]. This new variety of CMCs is all-oxide CMCs. All-oxide CMCs, unlike non-oxide CMCs, are less likely to degrade at higher temperatures, making them more applicable for long term use in oxidizing environments.

However, even further steps have been taken to enhance all-oxide CMCs so that they can perform at even higher temperatures, above 1250 °C. The step taken has been the addition of a third phase or interphase known as fiber coating. Until recently most coatings had a tendency to weaken the oxide fibers, but lanthanum phosphate ( $\text{LaPO}_4$ ) or monazite has proved compatible with oxide fibers [7,27].

The objective of this thesis was to investigate performance of an all-oxide CMC with monazite coating in compressive creep at high temperatures. The monazite containing CMC was tested along with the control N610/alumina CMC to study the effects of fiber coating on compressive creep resistance. The CMC was a symmetric cross-ply ( $0^\circ/90^\circ/0^\circ/90^\circ_s$ ). Initial focus of this investigation was on the off-axis tensile creep behavior of the same material at high temperatures. Early findings revealed low ultimate tensile stress and suggested that studies into tensile creep of the CMC with  $\pm 45^\circ$  fiber orientation would not be beneficial. The study was then switched to investigate the compressive creep behavior of this material with  $0^\circ/90^\circ$  fiber orientation.

## **II. Background**

This section will discuss the general make-up of ceramic matrix composites including fibers, matrix, and interfaces. It will also include a discussion of all-oxide CMCs, various processes used to fabricate CMCs, and aerospace applications of CMCs. Concluding this chapter will be remarks about the tensile versus compressive failure mechanisms, previous work conducted on similar CMCs, and the objective of this thesis.

### ***2.1 Ceramic Matrix Composites***

#### **2.1.1 Fibers**

The main function of fiber in a composite is to serve as reinforcement. Depending on length, fibers are classified as either continuous or discontinuous. Discontinuous fibers, such as short fibers or whiskers, are no more than few millimeters in length. Continuous fibers, also called filaments or monofilaments depending on their aspect ratio span the length of the material. Continuous fibers are laid out in the material in what are called tows, which are simply bundles of continuous fibers. Tows can vary in the number of fibers they contain.

Ceramics fibers, like the ones used in this investigation, are ideal for high strength and high temperature applications. Some fibers, such as Nextel<sup>TM</sup>610 developed by the 3M Corporation, are used because of their high strength at temperatures around 1000 °C [43:18]. They also exhibit a high modulus of elasticity and generally do not undergo environmental degradation [10:47].

Ceramic fibers fall under the category of a synthetic fiber. Other synthetic fibers include metallic and polymeric fibers. There are various types of ceramic fibers.

Zirconia ( $\text{ZrO}_2$ ), alumina ( $\text{Al}_2\text{O}_3$ ), silica-based glasses, Boron (B), silicon carbide (SiC), Carbon (C), silicon nitride ( $\text{Si}_3\text{N}_4$ ), and boron nitride (BN) are all examples of ceramic fibers. Of the eight mentioned the latter five are non-oxide fibers. Non-oxide fibers are more likely to undergo environmental degradation when exposed to oxidative environments, which compromises the strength of the fiber by changing its chemical make-up [39:2]. Until recently, ceramic fibers were not ideal for applications which required high strength and creep resistance, but fully crystalline fibers developed by the 3M corporation known as Nextel<sup>TM</sup>610, 650, and 720 demonstrated high strength and resistance to creep [40:2]. If the fiber is fully crystalline, it contains no silica or glassy phases. These phases become viscous at high temperatures and affect creep resistance [1,40:6]

Creating oxide fibers is generally accomplished using a sol-gel method, which consists of these basic steps: formulate sol, concentrate to form a viscous gel, spin the precursor fiber, and calcine to obtain the oxide fiber [10:66]. Non-oxide fibers of the silicon carbide type are made by one of two methods. They are made either by chemical vapor disposition (CVD) or from polymeric precursors. The latter method was explored as an alternate route of making fibers in order to obtain finer and more flexible fibers than those created by CVD [10:78].

### **2.1.2 Matrix**

The matrix of a composite is the material that the fiber reinforces. The matrix serves a couple of purposes. It provides a structure for the fibers and protection from the environment. Steel reinforced concrete is a great example of this fiber/matrix

relationship. Concrete, the matrix, provides both a solid structure and environmental protection for the steel bars that reinforce it.

Ceramic fibers most commonly serve to reinforce ceramic matrices, but can be used to reinforce metal matrices as well. Ceramic materials such as alumina ( $\text{Al}_2\text{O}_3$ ), silica ( $\text{SiO}_2$ ), mullite ( $3\text{Al}_2\text{O}_3\text{-}2\text{SiO}_2$ ), silicon carbide (SiC), boron nitride (BN), Carbon (C), and Boron (B) are all possible candidates for ceramic matrix materials. Ceramic matrix materials like their fiber counterparts are chosen for their high strength, modulus of elasticity and ability to withstand very high temperatures

Ceramic matrix materials, just as the fiber, can be designated as oxide or non-oxide. Alumina and silica are common oxides that are to some extent oxidation resistant. Common non-oxide ceramic matrix materials include boron carbide and silicon carbide. Just as with fiber selection, when the application exposes the material to high temperatures for long periods of time, it is important to choose a ceramic matrix that has been oxidized.

Ceramic materials are known to be very brittle. Why CMCs have become so appealing is that the introduction of continuous fiber reinforcement can make ceramics behave in a less brittle manner and make them more damage tolerant [4:565]. As the density of a ceramic increases so do its mechanical properties. Unfortunately, testing has shown that in CMCs porosity in the matrix plays a vital role in crack deflection [28,43:15]. Figure 1 shows the two known crack deflection mechanisms for CMCs.

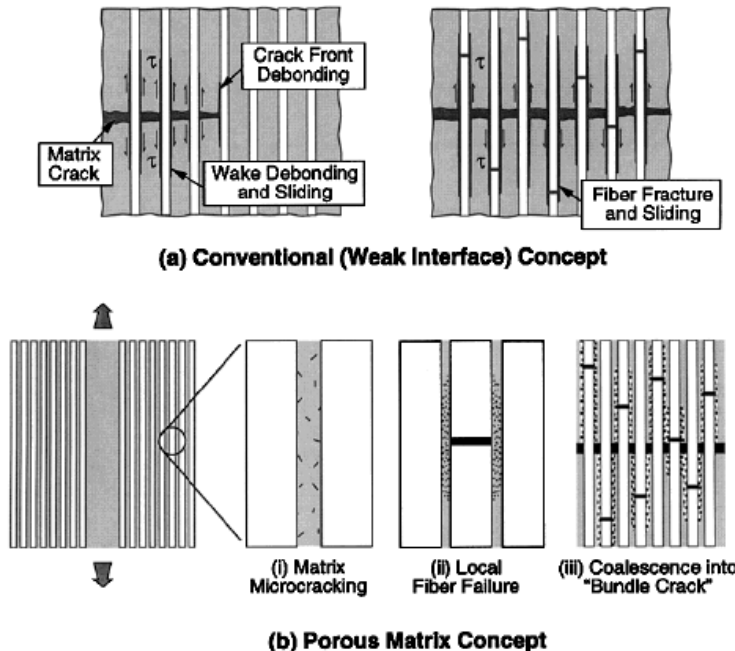


Figure 1. “Schematics of the Damage Processes that Enable Damage Tolerance in a) Conventional Dense-Matrix Weak-Interface CMC and b) Porous Matrix CMCs Without Fiber Coatings” [43:15].

“A ‘weak’ interface between the matrix and fiber provides the path for crack deflection, thus allowing the crack to propagate along the fiber/matrix interface instead of through the fiber” [21:607]. Therefore it is actually detrimental to the CMCs mechanical properties if the matrix is dense. It is known that porous fiber coatings provide a path for crack deflection [13,31] and in the same manner a porous matrix accomplishes the same [37:2]. In most cases when dealing with a porous matrix, the crack must actually originate from within the fiber itself [21:608] because the matrix lacks the strength to cause high enough stress concentrations on the fiber to cause failure [28:2622].

### 2.1.3 Interphase

Interphase, also known as a fiber coating, between matrix and fibers plays an extremely important role in the strength and toughness of a ceramic matrix composite.

However, coatings can degrade the strength of the fiber if the fiber and coating are not compatible. The addition of this third phase has two main purposes, to “fail before the fiber fails, thereby removing matrix-imposed stress concentrations on the fiber” and to “allow some sliding along the fiber/matrix debond after deflection” [28:2606]. Coating can also serve to protect the fibers from the affects of oxidation. There are two methods for dissipating a crack’s energy in a ceramic matrix composite: a weak matrix or a ceramic fiber coating. A weak matrix, mentioned in the previous section, relies on porosity to deflect crack growth. Ceramic fiber coatings rely on “mechanisms that permit the development of multiple matrix cracks, which in turn produce inelastic strain during tensile loading. Furthermore, they provide a means for mechanically decoupling the fibers from one another and hence allow the fibers to fail in an uncorrelated manner” [43:15].

The most common types of ceramic fiber coatings used are C, BN, lanthanum phosphate (monazite,  $\text{LaPO}_4$ ), yttrium phosphate ( $\text{YPO}_4$ ), and cesium phosphate ( $\text{CePO}_4$ ). The latter three are used for their oxidation resistant properties at high temperatures [28,29]. When choosing a coating for a CMC, it is important that it be “oxidation-resistant at high temperatures, thermally and chemically compatible with the fibers, and weakly bonded” [29:2] to the fibers.

It is important that the fiber/matrix bond is weak in order to ensure a weak interface in a composite. If the interface is strong, a crack can propagate through the fiber/coating/matrix interface and cause the material to fail. Just as in the porous matrix, a weak interface promotes crack energy absorbing schemes within the matrix and fibers. The schemes proceed with debonding at the interface, followed by crack deflection, crack

bridging, fiber fracture, and then fiber pullout [10:147]. In CMCs with uncoated fiber, there is often very little or no fiber pullout because the fibers are bonded directly to the matrix and will fail with the matrix along that crack plane. It has been known that mixed rare-earth and alkaline earth phosphates, tungstates, and vanadates all bond weakly to oxide fibers [14:584]. Pyrocarbon (PyC) and BN are common coatings for non-oxide fibers [9:1179,28].

The application of fiber coatings is a difficult process and has become a large field of study. Two common problems associated with fiber coatings are fiber bridging and poor fiber coverage (see Figure 2). The former can lead to poor matrix infiltration into fiber bundles and the latter allows fiber and matrix to bond together making the composite more brittle [14:584,28:2624]. There are three gas-phase deposition techniques for applying coatings to ceramic fibers: CVD, physical vapor deposition (PVD), and combustion CVD. Of the three, the latter two unfortunately do not work well when applying coatings to filaments, because they essentially rely on line-of-sight and therefore it is difficult to apply the coating to all the fibers [28:2623-24]. Using liquid-phase processes is a cost-effective option, but very little work has been done on applying ceramic coatings to ceramic fibers [28:2624]. One technique used is the sol-gel technique, which was used in this investigation to apply the coating to the fiber. In the course of this process the fiber is passed through a tank containing a sol and wound on a wheel, where sol-gel transition occurs. Finally the gel-coated fiber is subjected to controlled heating to densify the gel [10:24,10:126]. Some of the work that has been done applied vacuum enhanced dip-coating [29]. All of the above the processes are

expensive and difficult to execute properly and require highly sophisticated equipment and techniques.

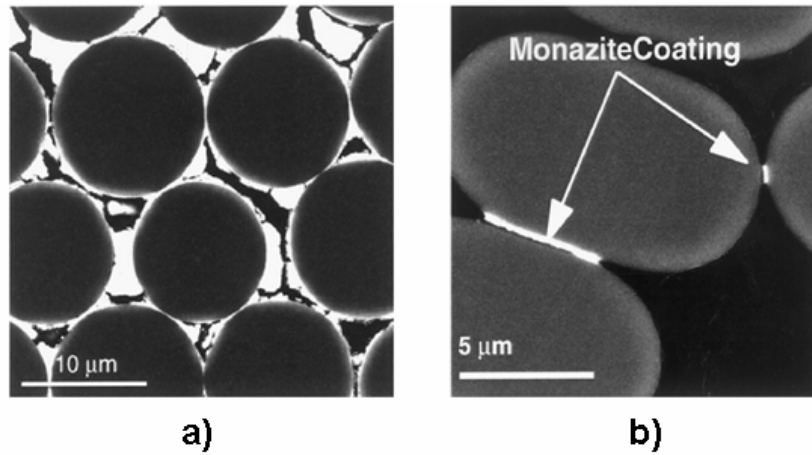


Figure 2. Monazite Coating is the Bright Areas in the Pictures. (a) Shows Fiber Bridging and (b) Shows Incomplete Fiber Coverage [14:584]

#### 2.1.4 All-Oxide CMCs.

If a CMC is all-oxide, it implies that all the phases contained within the composite have been oxidized. Non-oxides are classified by either containing no phases that are oxidized or a combination of oxidized and non-oxidized phases. Until recently, most CMCs were based on SiC fibers in oxide or non-oxide matrices [9,40]. The problem with these CMCs is that when cracks occur within the matrix at high temperatures, over a period of time oxidants like water vapor and oxygen can proceed through them, which in turn causes degradation of the fibers [11:193,18,24]. Figure 3 shows how this process can take place.

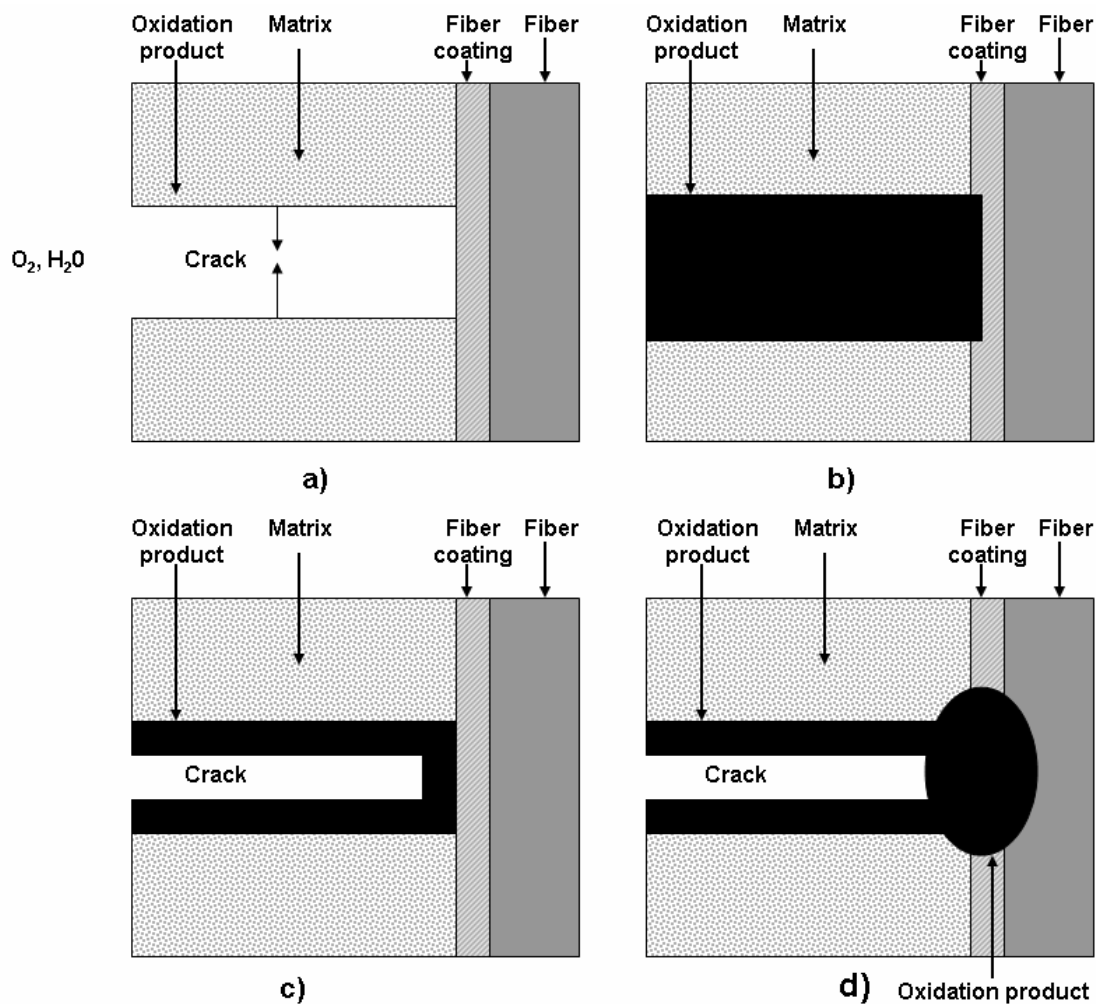


Figure 3. Schematic Representation of Oxidation Progression through Matrix Crack of CMC with Fiber Coating

As seen in Figure 3a, the oxidants enter the crack and then products of the oxidation reduce the width of the crack as seen in Figure 3c. Two things occur at this point. The products either seal the crack preventing damage to the fiber/coating/matrix interface as seen in Figure 3b or as shown in Figure 3d the crack may not seal before the oxidant seeps into the coating and through to the fiber where it oxidizes the fiber. For this exact reason, all-oxide CMCs have been developed for use in long-term, high-temperature environments.

All-oxide CMCs can be designed two different ways. One design uses a weak interface, or fiber coating [28,30,36:214]. The second relies on porosity within the matrix to provide crack deflection [30,36:214,43]. For this investigation, a CMC with a weak interface was used. The three oxidized phases were the alumina fiber, the alumina matrix, and the monazite fiber coating.

### **2.1.5 Fabrication of CMCs**

Fabrication of the CMCs is the most critical step in the life of a CMC. After carefully selecting the fiber and matrix, the fibers can be incorporated into the unconsolidated matrix followed by laying up of the fibers in the desired orientation. These two steps can occur in reverse order depending upon the technique used. Finally, the process ends with consolidating the matrix. Coating the fiber is an additional step that can occur before or in-situ with consolidation.

Choosing fiber, matrix, and coating (if desired) is a very critical step in the CMC fabrication process. The application of the CMC will dictate which materials will be chosen. However, the matrix and fiber materials must be thermally and chemically compatible. If the matrix and fiber have different coefficients of thermal expansion, then heat up or cool down of the CMC produces residual stresses between fiber and matrix causing matrix cracking [22:554]. This type of matrix cracks is sometimes referred to as shrinkage cracks, which can be more exaggerated depending on the porosity of the matrix, dispersion of matrix material, orientation and form of fibers, and processing control and methodology. However, some CMCs are specifically designed to contain a thermal mismatch. For example, the Nextel 720 fiber laid up in an alumina-mullite matrix creates a thermal mismatch at room temperature, but at higher temperatures the

thermal mismatch between fibers and matrix is reduced and so are the residual stresses. Chemical incompatibility between fibers and matrix will tend to damage the fibers degrading their properties.

Incorporation of the unconsolidated matrix into the fiber for ceramic matrix composites is done through various techniques. Only the most common techniques will be considered. There is cold pressing followed by sintering, hot pressing and its variations, infiltration, in-situ chemical reactions, sol-gel, and many others. Hot pressing is probably the most common technique used and is often used with the other processes, although it can be done as a single step. Hot pressing simultaneously applies pressure and high temperatures to densify the matrix. The result, if thermal compatibility exists between fiber and matrix, is a compact and a pore-free CMC [10:100]. Hot pressing was used to consolidate the matrix material in this investigation. Often hot pressing is used with slurry infiltration, as it was in this investigation. Slurry infiltration integrates the reinforcement phase into a slurry of the unconsolidated matrix, then the matrix is consolidated by hot pressing. In-situ chemical reactions are another common method used to produce CMCs. These techniques, like chemical vapor infiltration (CVI), are used to infiltrate fibrous preforms into a solid shape. Sol-gel technique is great for producing multiphase matrix materials and reducing processing temperatures, but often is associated with large amounts of shrinkage [10:125]. When the matrix shrinks, the material exhibits significant matrix cracking.

## ***2.2 Aerospace Applications***

The aerospace field is an exciting area for the application of ceramic matrix composites. Their desirable thermomechanical properties and strength to weight ratio

make CMCs prime candidates for aerospace components. The aerospace industry is always looking for ways to increase efficiency of aircraft, reduce costs, achieve higher operating temperatures, and cut back on maintenance [10:399].

The most applicable areas for CMCs in the aerospace field are components of turbine engines, space satellites and vehicles. The need to increase operating temperatures within the engine in order to create an efficient combustion process has led scientists to consider monolithic ceramics [39:3]. However, the lack of structural integrity of monolithic ceramics has made CMCs a more viable choice for use in aero-engines [35:489]. All-oxide CMCs are even more applicable in this area because of the environmental degradation that would occur at high temperatures produced by both nozzles and combustors of turbine engines. In turbine engines, CMCs can be used for many parts. CMCs have been tested for use as blisks (bladed disks), nozzle flaps, exhaust nozzles, combustor, and turbine vane nozzles [35]. The ultimate goal for this material's use in turbine engines is to operate at 1400 °C without cooling [6:17,36:214].

### ***2.3 Tensile vs. Compressive Failure Mechanisms***

As with monolithic materials, ceramic matrix composites fail in different manners when exposed to different types of loading. Composites fail when the phase with the lower ultimate strain does and in the case of CMCs that phase is commonly the matrix. Under tension CMCs, like other brittle-matrix composites, first develop multiple matrix cracks. “These cracks create local stress distributions with high interfacial shear stresses and increased tensile stress in adjacent fibers” [12:90]. This is schematically shown in Figure 4.

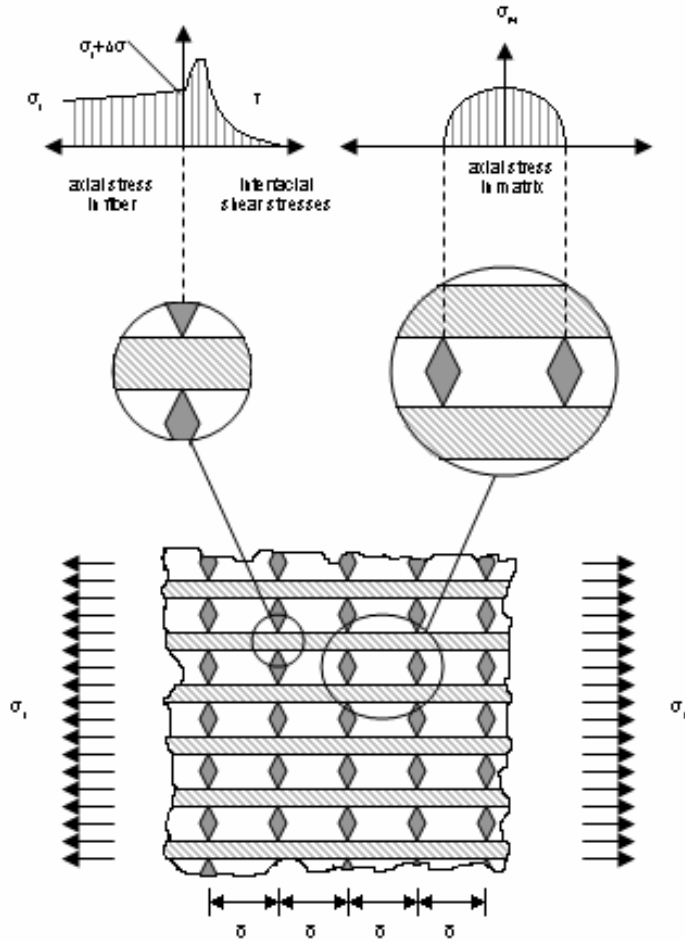


Figure 4. Schematic of Matrix Cracking and Local Stress Distributions in Composite under Longitudinal Tension

However, in compression a reinforced fiber composite has a much different failure mechanism. Compression introduces what is called microbuckling or kinking of the fibers within the matrix. These form kink zones, which cause fracture planes in brittle fibers. Figure 5 illustrates microbuckling and Figure 6 shows the possible shear failure mode for composites containing high fiber volume ratios. Figure 7 shows the final mode of failure that a CMC can experience in compression, which can be referred to as transverse splitting. In this mode of failure the matrix splits apart causing delamination.

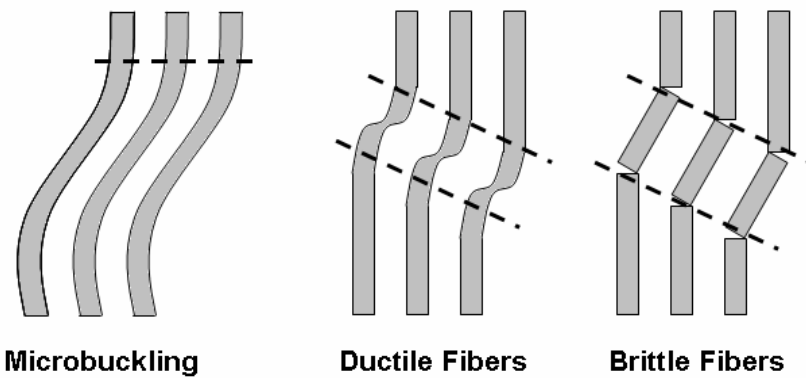


Figure 5. Schematic of Microbuckling, which Leads to Excessive Deformation in Ductile Fibers or Fracture Planes in Brittle Fibers

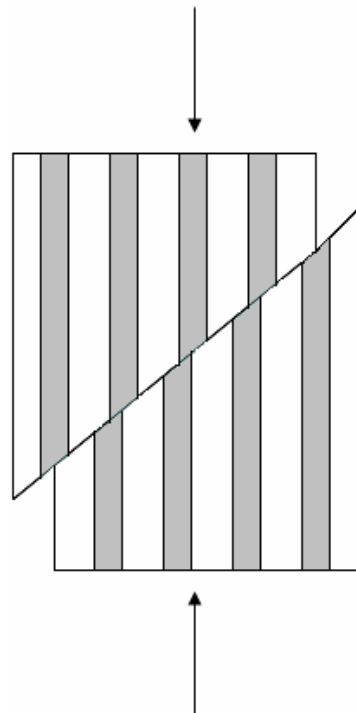


Figure 6. Schematic of Shear Failure Mode of Unidirectional Composite Under Longitudinal Compression

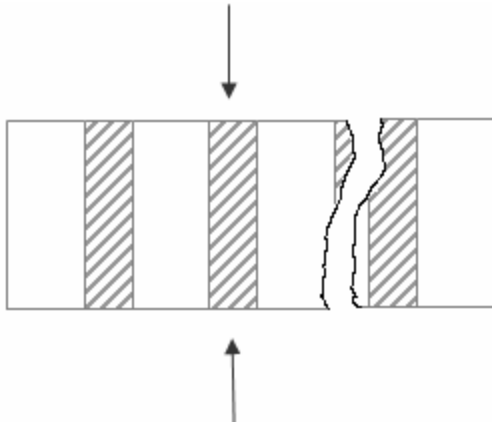


Figure 7. Schematic of Transverse of Splitting of Unidirectional Composite Under Longitudinal Compression

#### 2.4 Previous Work

There has been a lot work done in the area of ceramic matrix composites since their inception. Numerous studies investigated thermal and mechanical properties, interface, and fiber selection. Work concerning the N610 and N720 fibers is very abundant. Currently, the N720 fiber is being looked at more seriously because of its superior creep resistance at high temperatures. Interface design is of interest to a lot of researchers, because it is the primary mechanism for crack deflection in CMCs. Some of the research efforts regarding interface have explored effects of coating deposition temperature [23], porosity [43], design for oxidation-resistant ceramic composites [28], the influence of fiber coating conditions on the mechanical properties [9], and fiber coating conditions effect on the mechanical properties of a CMC [29].

There has been only a small amount of work regarding the specific materials explored in this report. One report concerning N610 fiber engages in the examination 8-harness satin weave of N610 fibers infiltrated with a slurry of alumina/lanthanum phosphate that created a porous matrix composite [15]. It was found by Davis et al [15] that this oxide

composite exhibits “greater nonlinear response and notch insensitivity than other porous matrix composites” and this improvement in its properties is due to “weak bonding between the fibers and the LaPO<sub>4</sub> phase, which allowed the extensive fiber pullout” [15]. This investigation explores LaPO<sub>4</sub> as a coating, but its nature to bond “weakly” to the fibers and/or matrix will be of much interest. The only data collected regarding the CMC studied in this thesis was reported by Musil et al [34,38], who investigated the on-axis monotonic tensile and tensile creep behavior of N610/monazite/alumina and N610/alumina composites. The only other study reported in literature was conducted by Keller et al [27], who investigated the effectiveness of monazite coating by comparing response of N610/monazite/alumina and N610/alumina composites exposed to temperatures of 1100 °C and 1200 °C for varying lengths of time. Coated fiber composites showed smaller reduction in strength compared to the uncoated fiber CMCs exposed to 1200 °C for a short period of time [27].

The following two sections will discuss the work done regarding CMCs in the two areas of interest, monotonic tensile and tensile creep off-axis behavior of CMCs and monotonic compressive and compressive creep on-axis behavior of CMCs.

#### **2.4.1 Off-Axis Behavior of CMCs**

Off-axis behavior of materials is studied because it is rare that a material will only be subjected to on-axis forces. There has been little to no work done on the off-axis tensile behavior of N610/monazite/alumina and N610/alumina prior to this investigation. However, there have been several investigations into the off-axis tensile behavior of CMCs reinforced with N610 and N720 fibers [4,5,8,21,28,30,43]. Results reported by Levi et al [30] on the tensile behavior of two-dimensional woven preforms of N610 in an

alumina-mullite matrix without interphase showed a decrease in modulus, increased strain at fracture, and a lower fracture strength at room temperature when compared with results produced by the same CMC with 0°/90° fiber orientation. Two other studies of off-axis behavior explored a 12 layer uncoated plain weave and an 8 harness satin weave [4,8]. The former showed similar results to those seen for the N610 reinforced composite, but the latter reported that the 8 harness satin weave CMC exhibited similar moduli in both the 0°/90° and the ±45° fiber orientations.

#### **2.4.2 Compression**

Preceding this investigation, monotonic compressive and compressive creep behavior of N610/monazite/alumina and N610/monazite/alumina composites had not been studied. As mentioned earlier, Musil et al [34,38] explored the tensile properties of this material. Some previous efforts regarding compressive properties of CMCs were concerned with behavior of in-situ single-crystal alumina/yttrium aluminum garnet eutectic composite with an on-axis fiber orientation [19] and behavior of SiC fiber reinforced mullite matrix composite [17]. Both studies were conducted at elevated temperatures. Harada et al [19] and Deng [17] showed that creep strain rates decreased for fiber orientations in the direction of loading. Harada et al (19:2221) reported that the ceramic exhibited a short primary creep stage common of compression creep.

#### **2.5 Thesis Objective**

The objective of this thesis is to explore the compressive creep behavior of the N610/monazite/alumina and N610/alumina composites at temperatures of 900 and 1100 °C. The effect of coating, stress levels, and temperature on the material response will be explored. The initial objective of this thesis was to study the tensile creep

behavior of N610/monazite/alumina and N610/alumina with  $\pm 45^\circ$  fiber orientation at 900 °C. However, early findings revealed very low ultimate tensile strength, implying low creep resistance for this fiber orientation. Consequently further investigation of the off-axis tensile creep was deemed unnecessary.

### **III. Material and Specimen**

This chapter will discuss the material and its specifications. It will begin with the discussion of the fiber, matrix, and interphase materials used and conclude with the description of processing, specimen geometry, and specimen preparation.

#### ***3.1 N610/Monazite/Alumina and N610/Alumina Composites***

The materials under investigation, N610/monazite/alumina and N610/alumina composites, were both developed by the Materials and Manufacturing Directorate of the Air Force Research Lab, AFRL/MLLN, located on Wright-Patterson Air Force Base, Ohio.

##### **3.1.1 Nextel<sup>TM</sup>610 Fiber.**

The Nextel<sup>TM</sup>610 ceramic fiber serves as the reinforcement for the materials under investigation. It was developed along with the Nextel<sup>TM</sup>720 fiber for load bearing applications. Within the last few years, Nextel<sup>TM</sup>650 was also introduced as a viable ceramic fiber. These fibers can be used in metals, ceramics, and polymers. The N610 fiber is 99% alumina, which is an oxide of aluminum. The fiber is a fine grained single-phase composition of alumina. However, since it is single-phase, strength does steadily decrease at temperatures above 1000 °C due to grain growth [1:8]. The addition of mullite in the Nextel<sup>TM</sup> 720 fiber reduces grain boundary sliding at high temperatures, which in turn inhibits grain growth. Nextel<sup>TM</sup> 650 fiber also has better properties in creep because of the addition ZrO<sub>2</sub> [40]. However, both types of fibers have a lower tensile strength than that of Nextel<sup>TM</sup> 610 fiber [40]. The properties of the N610 ceramic fiber are summarized in Table 1.

Table 1. Nextel<sup>TM</sup> 610 Fiber Properties [1,2]

Composition (wt%)	
Al <sub>2</sub> O <sub>3</sub>	>99
SiO <sub>2</sub>	0.2-0.3
Fe <sub>2</sub> O <sub>3</sub>	0.4-0.7
Average Grain Size (μm)	0.1
Filament Diameter (μm)	10.0 - 12.0
Density (g/cm <sup>3</sup> )	3.88
Tensile Elastic Modulus (GPa)	373
Tensile Strength (MPa)	3100

### 3.1.2 Alumina Matrix

Alumina is the matrix material used in this investigation. It has only one thermodynamically stable form, which is  $\alpha$ -Al<sub>2</sub>O<sub>3</sub>. Alumina can be toughened by zirconia particles [10:35]. Unfortunately, densifying takes place by sintering at 1500 °C. This process would damage the fibers by inducing grain growth. Fine-grained alumina is good for use at low temperatures because both strength and toughness increase with decreasing grain size, but for the high temperatures seen in this investigation a larger grain size alumina was used in order to improve high-temperature properties.

As mentioned before, alumina is an oxide of aluminum and was chosen because of its resistance to oxidation. Alumina has a density of 3.9 g/cc. Its coefficient of thermal expansion ranges from  $7 - 8 \times 10^{-6}$  / °C. The Young's Modulus of alumina 380 GPa and its strength ranges from 300 to 900 MPa depending on grain size.

### **3.1.3 Monazite Coating.**

Monazite ( $\text{LaPO}_4$ ) was the fiber coating used in the CMC in this investigation. In early efforts monazite fiber coatings degraded both Nextel<sup>TM</sup>610 and Nextel<sup>TM</sup>720 fibers. However, recently the appropriate slurry composition was found that retained the strength of the fibers after sintering [7,14]. Monazite is refractory, thermochemically stable with refractory oxides like alumina [32,33], bonds weakly to other oxides [25], and was demonstrated to be machineable [16]. Its melting point is over 2000 °C and it is already oxidized so it is stable in air and water-containing environments. Other properties of monazite include a thermal expansion coefficient of  $9.6 \times 10^{-6} / ^\circ\text{C}$  and a density of 5.13 g/cc. Monazite can be applied as coating to fibers or formed in-situ between fiber and matrix during processing.

In this investigation, the former technique was used. The monazite was applied to the N610 fiber using a sol-gel dip coating technique. Although fiber bridging is often associated with liquid-phase precursors [28:2624], this method was used because of its low processing temperatures [7]. This way the fiber was not damaged during coating procedure.

## **3.2 Specimen Development**

### **3.2.1 Material Processing**

All material used in this research was processed by AFRL/MLLN, Wright Patterson Air Force Base. The following procedure was used to fabricate CMC panels for this investigation. Note that the fabrication procedure is slightly different for the control and the coated fiber composites. The N610 fiber to be coated was first desized at 1100 °C, then coated with  $\text{LaPO}_4$  using a sol-gel technique with a 20 g/l sol. Coating speed was

approximately 5 cm/sec at a temperature of 1100 °C. The coated fiber was then spooled onto a take-up wheel. No sizing was applied over the coating.

Two slurries were prepared. The slurry prepared for the uncoated fiber composite was comprised of 15 vol.% alumina powder (AKP-53, Sumitomo Corp.) and 85 vol.% alumina sol (aluminum nitrate + deionized water + citric acid + ethylene glycol). The slurry for the coated fiber composite contained 12.5 vol.% alumina powder and 87.5 vol.% sol. The fibers were then drawn through their respective slurries and then wound onto a drum, forming a tape. The wound tape was cut and stacked in [0°/90°/0°/90°/90°/0°/90°/0°] sequence as seen in Figure 8. The composite stack was sealed in a vacuum bag and placed in an autoclave. The sample was evacuated and then heated to approximately 85 °C. This temperature was held for 1 h under 100 psig. The sample was removed after it had cooled and allowed to air-dry overnight. Next the sample was heat treated at 1200 °C in a box furnace for 5 h in air.

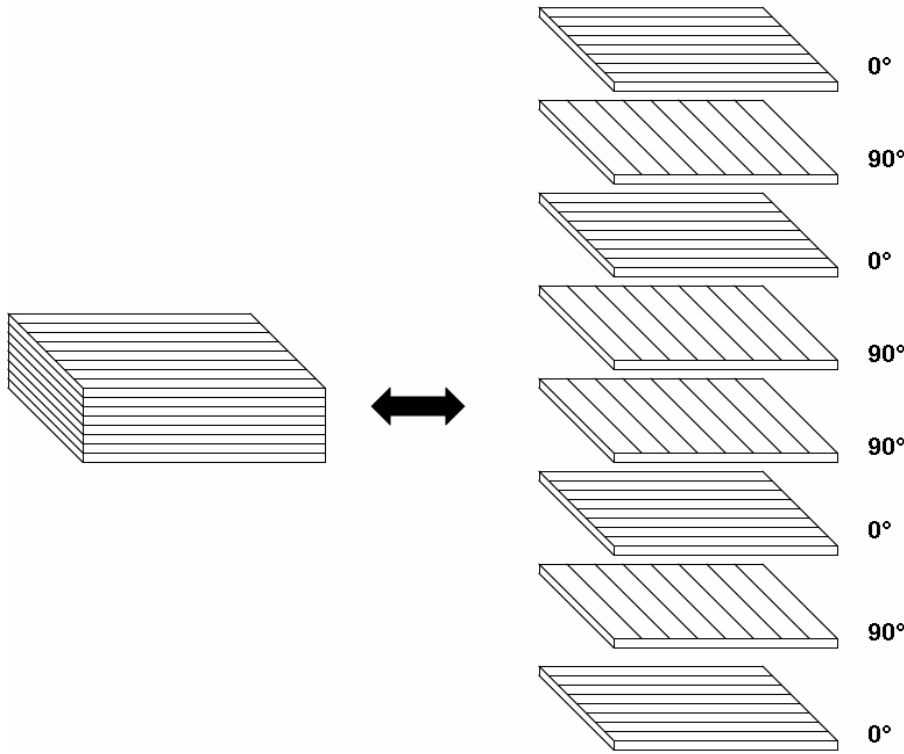


Figure 8. Schematic of  $(0^\circ/90^\circ/0^\circ/90^\circ)_s$  Fiber Orientation

The specimens were cut from the panels using waterjet machining. A sheet of aluminum was laid on top of each panel to prevent frayed edges on the specimens. After the specimens were cut, they were cleaned in an ultrasonic bath. Then the specimens were immersed in alcohol for about 15 minutes, to pull the moisture out of the specimens. The specimens were then removed from the alcohol and placed in an oven for 1 h at 250 °C. After the specimens cooled they were ready for testing.

### **3.2.2 Panel Specifications**

There were a total of 8 panels made. Of those eight, five were N610/monazite/alumina and three were N610/alumina. The tensile specimens were cut from three different panels. The two monazite containing panels were labeled A1 and B1

and had fiber volume fractions of approximately 30.0% and 29.1%, respectively. Fiber volume fractions were obtained by counting the number of filaments wound per the number of the revolutions. The control panel, labeled C1, had a fiber volume fraction of 35.0%. The average densities of A1, B1, and C1 panels were 2.68, 2.55, and 2.73 g/cc, respectively. For all panels, density was found by dividing weight over the volume of the specimens after they were cut from the panel.

The compressive specimens were cut from the five remaining panels. The panels were referred to in this report as monazite panels M1, M2, and M3 and control panels N1 and N2. Panel specifications are given in Table 2. All fiber volume fraction and density values were obtained in the same manner described above.

Specimens from the first three panels were labeled in the following manner: panel designation, fiber orientation, and number. Therefore, specimen 2 from panel B1 with 0°/90° fiber orientation would be marked as B1-0-2. Specimens from the remaining panels were marked with panel number, but did not contain a reference to fiber orientation. Specimen 6 from monazite panel M2 would be designated as M2-6. Note that all specimens from panels 4-8 were cut with the 0°/90° fiber orientation.

Table 2. Fiber Volume Fraction and Density of Panels Used for Compression Tests.

<b>Material</b>	<b>Panel #</b>	<b>Designation</b>	<b>Vf</b> (%)	<b>Density</b> (g/cc)
N610/LaPO <sub>4</sub> /Al <sub>2</sub> O <sub>3</sub>	1	M1	26.40	2.58
N610/LaPO <sub>4</sub> /Al <sub>2</sub> O <sub>3</sub>	2	M2	29.00	2.53
N610/LaPO <sub>4</sub> /Al <sub>2</sub> O <sub>3</sub>	3	M3	26.00	2.47
N610//Al <sub>2</sub> O <sub>3</sub>	1	N1	36.00	2.79
N610//Al <sub>2</sub> O <sub>3</sub>	2	N2	34.50	2.82

### 3.2.3 Specimen Geometry

#### 3.2.3.1 Tensile Specimens

When referring to the specimens it is important to specify their various fiber orientations. The specimens with  $\pm 45^\circ$  fiber orientation were referred to as such or as “off-axis” specimens. It was necessary to refer to the on-axis specimens in two ways because not all were oriented along the same direction in the panel and the fiber direction of the surface layer appeared to play a direct role in the strength of the material. Therefore, the specimens that had the surface layer with  $0^\circ$  fiber orientation were referred to as  $0^\circ$  specimens and those that had the surface layer with the  $90^\circ$  fiber orientation were referred to as  $90^\circ$  specimens. Tensile specimens were cut to specifications in Figure 9. Standard dog-bone shape was used to promote failure in the gage section.

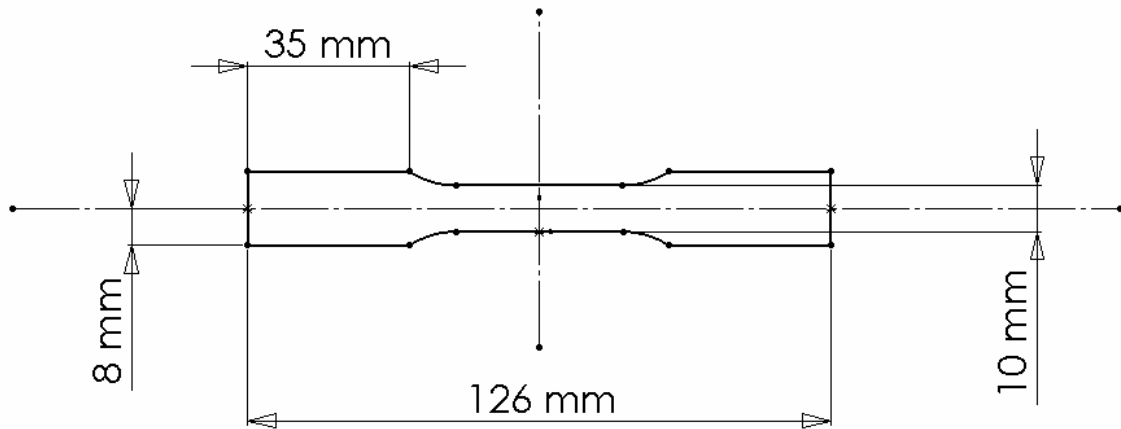


Figure 9. Tensile Specimen

### *3.2.3.2 Compressive Specimens*

The specimens had to be no less than 126 mm in length to accommodate the oven for high-temperature testing. Ideally, a shorter, wider specimen is wanted for compression testing, but a shorter specimen could not be used with the testing equipment involved. A specimen width of 20 mm was chosen due to constraints imposed by the size of the oven. Figure 10 shows a compressive test specimen.

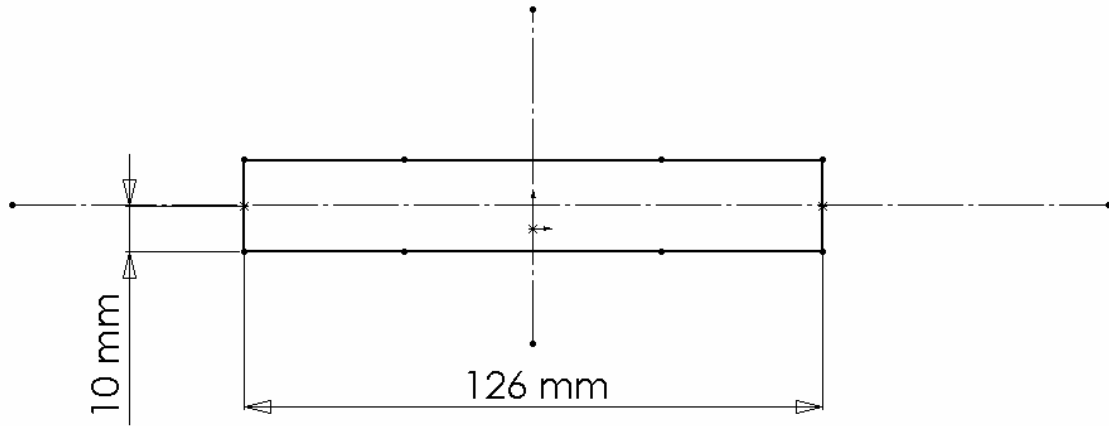


Figure 10. Compression Specimen

### **3.2.4 Specimen Tabbing**

Due to the high pressure applied to the specimen by the grips, all specimens had to be tabbed to ensure that surface was not damaged by the grips. Thin tabs of glass-fiber/epoxy material were bonded at the ends to both sides of the specimen. The tabs were cut to the width of the specimen. The length of the tabs was determined by the length of the specimen to be gripped. The tabs were glued to the specimens using M-Bond 200, which consisted of two components: catalyst and glue. First, the M-Bond catalyst was brushed onto the tabs and then 3 drops of the M-Bond glue was applied to

the tab surface. Then pressure was applied to the tab for one minute to ensure a good bond. Representations of a tabbed specimen can be seen in Figure 11.

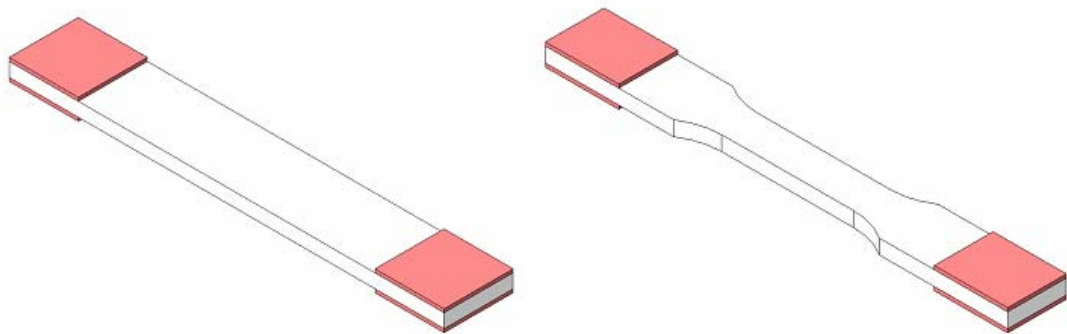


Figure 11. Tabbed Compressive and Tensile Specimens, Respectively

## **IV. Experimental Set-Up and Testing Program**

This chapter provides detailed description of the equipment and the procedures that were used to investigate the behavior of both Nextel 610/Monazite/Aluminum and Nextel 610/Aluminum composites.

### ***4.1 Test Equipment***

#### **4.1.1 Testing System and Components**

The testing system consisted of five main parts: the servo hydraulic machine, the chiller, the high temperature equipment, the extensometer, and the digital controller with associated computer software. The monotonic tension and compression tests, as well as the creep rupture tests, were performed using this equipment.

Two servo hydraulic machines were used to test the material. Both were manufactured by Material Testing Systems (MTS) Corporation. The axial 810 Material Testing System with a 25 kN (5.5 kip) capacity was used to conduct the initial testing of the off-axis specimens and some of the initial compression work (see Figure 12). However, because of the piston size, the machine load capacity was limited to 13 kN (3 kip), which was not sufficient to cause failure of a compression specimen. Another 810 Material Testing System, with a 100 kN (22 kip) capacity was used for the compression tests. Both machines were equipped with hydraulic wedge grips that could apply pressures ranging from 0-20 MPa.



Figure 12. 25kN Servo Hydraulic Machine

The chiller was comprised of two units manufactured by NESLAB: the chiller and the controller. The chiller was used to cool water to temperatures of 9.5 °C in order to cool the grips. Figure 13 shows the chiller and the controller. The two controller units are seen resting on top of the chiller.



Figure 13. Chiller and Controller

The chiller system provides cooled water to the hydraulic wedges to prevent them from overheating during high-temperature testing. If the wedges overheat during testing the seals within the wedges could be destroyed, which would cause severe damage to the system. In order to avoid this, the chiller pumped water through a 6.35 mm (0.25 in) outer diameter tubing, which ran through the grips as seen in Figure 14 below. The chiller was filled with distilled water to prevent corrosion. This system was used in all high-temperature tests.

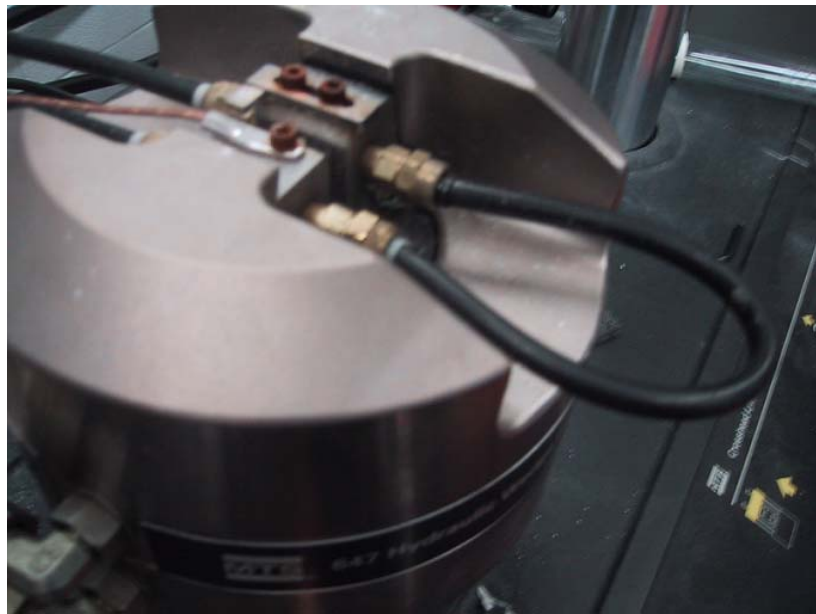


Figure 14. Tubes for Cooling Water Connected to Hydraulic Wedge Grips

The high-temperature equipment consisted of the oven, the temperature controller, and control thermocouples located in the oven. The oven can be seen in Figure 15 during a test. An interior view of an open oven half in Figure 16 shows the heating element and the control thermocouple. The control thermocouples located in the oven are S-type

thermocouples, which provide closed-loop feedback to the temperature controller. The oven was a single zone MTS 653 model. The max operating temperature of the oven is 1400 °C. The temperature controller was a MTS 409.83 model, shown Figure 17.

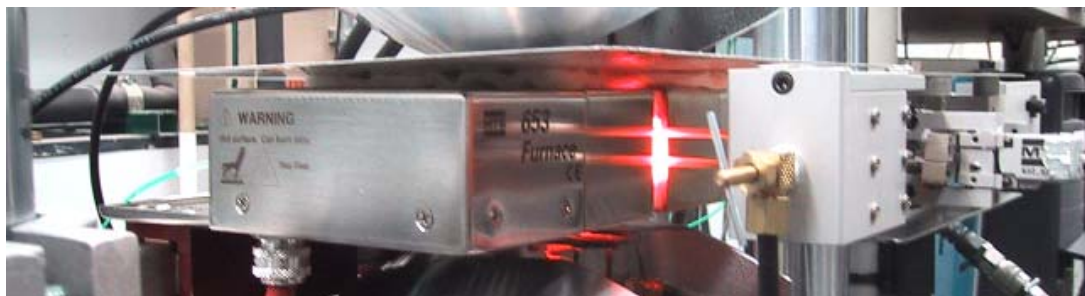


Figure 15. Oven Glows at High Temperatures

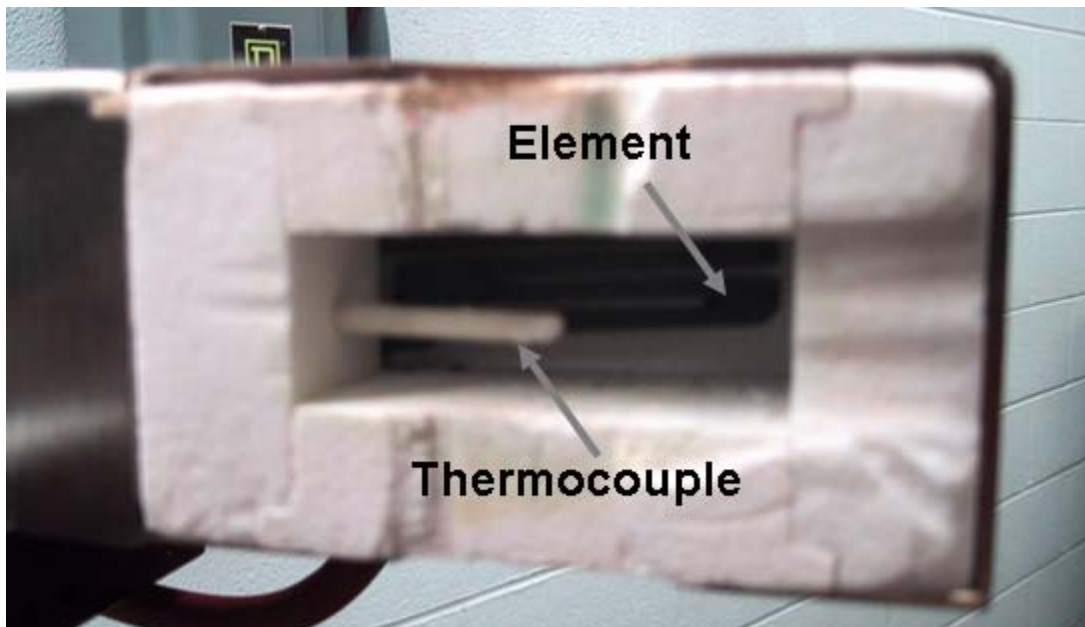


Figure 16. Interior View of Oven Half



Figure 17. Temperature Controller

The extensometer used to gather strain data during testing was an MTS axial high-temperature extensometer, model 632.53E-14 shown in Figure 18. The gage length of the extensometer is 12.7 mm (0.5 in). The extensometer was able to handle high temperatures by using two alumina extension rods of 3.5 mm diameter and 151 mm in length. The tips of the extension rods are cone-shaped in order to ensure firm contact with the specimen during testing. During testing, the extensometer is mounted behind the heat shield seen in Figure 19.



Figure 18. Extensometer Equipped with Alumina Rods

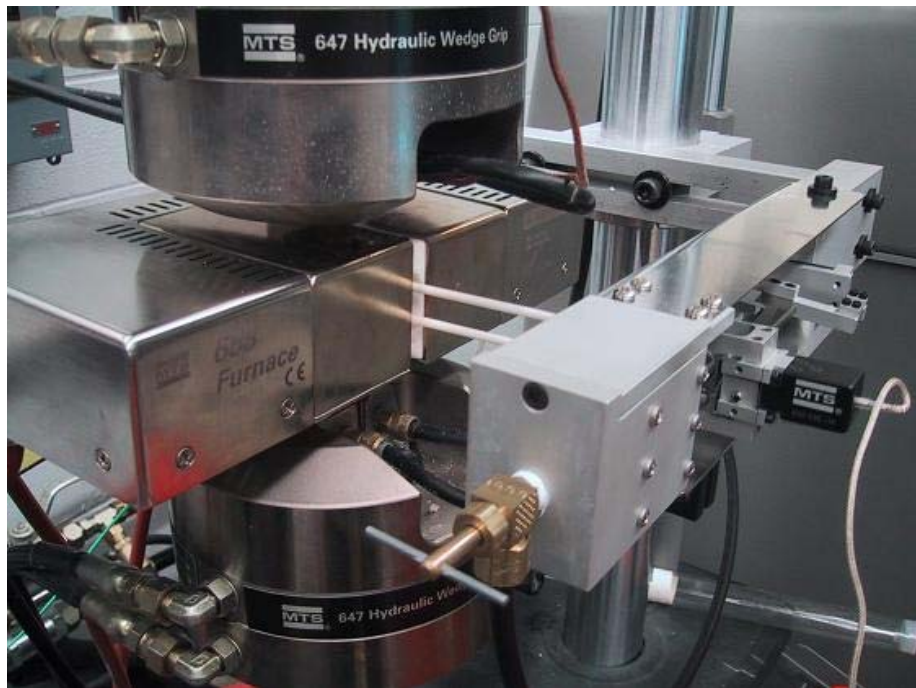


Figure 19. Extensometer Mounted Behind the Heat Shield

As seen in Figure 19, the rods extend through two slots in the furnace to make contact with the specimen. The heat shield and air cooling system prevent the extensometer from being damaged by overheating.

The final component of the testing system is the TestStar IIs digital controller, which was used for both input signal generation and data acquisition. The TestStar controller software controls the servo hydraulic machine and the temperature controller. During tests, displacements, forces, strains, temperature, cycles, and time can be monitored and recorded. Tests can be programmed using the Multipurpose Testware (MPT) software. Shown in Figure 20 is the basic test procedure developed for a high-temperature creep test.

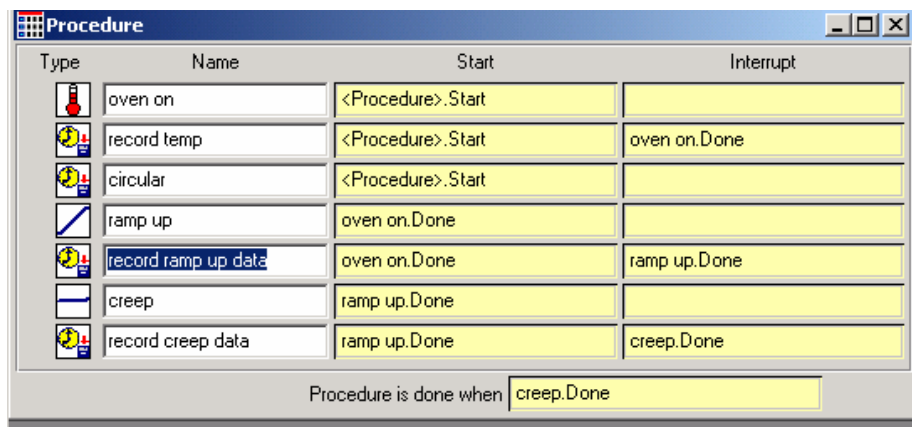


Figure 20. Multipurpose Testware Procedure for Creep Testing at Elevated Temperatures

The test procedure begins with a temperature ramp up and a dwell period to allow the specimen to thermally equilibrate and at the same time, data acquisition begins. After the dwell period, the program proceeds to ramp up the load to reach the specified creep stress at a set stress rate and records the data. Then the test program holds the load at a constant value while recording data.

#### **4.1.2 Specimen Components**

In order to accomplish parts of the testing the actual specimens had to be outfitted with two pieces of equipment, namely the thermocouples and the anti-buckling brackets. In order to perform the temperature calibration, two S-type thermocouples were attached to the gage section on each face of the specimen using high temperature ceramic cement and safety wire. It was extremely important to ensure good contact between the specimen surface and the tip of the thermocouple in order to obtain accurate temperature readings of the specimen surface. The thermocouples were connected to an OMEGA HH202A portable two-channel temperature sensor for read-out. The anti-buckling device, created for a use at room temperature consisted of two pieces of 7075-T6 aluminum bolted together that covered the sides of the specimen as shown in Figure 21 below.

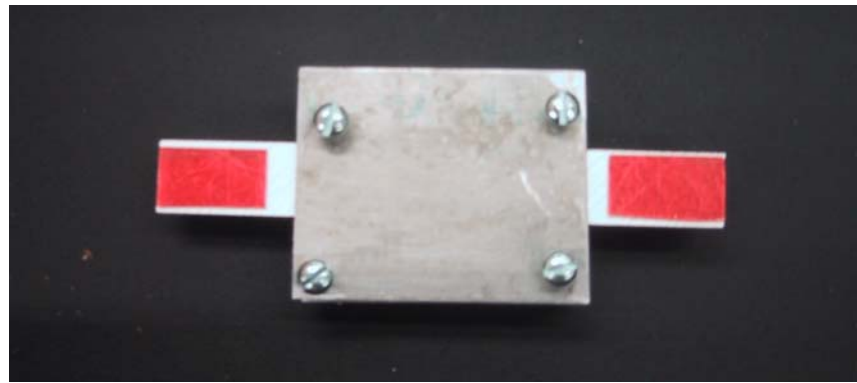


Figure 21. Specimen Equipped with Anti-Buckling Device

#### **4.2 Temperature Calibration**

To perform tests at 900 and 1100 °C, the oven and temperatures controller had to be calibrated. The specimen equipped with 2 S-type thermocouples was mounted in the grips. The thermocouples were connected to the OMEGA HH202A portable two-channel

temperature sensor for read-out. Both ends of the specimen were gripped leaving the machine in force control mode. The oven was closed around the specimen.

Using the MPT software, the oven was raised to about 100 °C below target test temperature at 1°C/s. Then the temperature of the oven was raised manually until the thermocouples on the specimen showed the desired test temperature. The temperature was then allowed to dwell for a period of 1 h. Small manual adjustments were made to ensure the specimen temperature was within ±10 degrees of the target test temperature. The set point of the temperature controller that produced the desired temperature of the specimen was recorded and used in the subsequent tests. To achieve the specimen temperature of 900 °C the temperature controller setting was 889 °C for the heating system on the 25 kN testing machine and 880 °C for the heating system on the 100 kN testing machine. A temperature controller setting of 1080 °C was required to achieve the specimen temperature of 1100 °C.

#### ***4.3 Test Procedures***

Three different types of tests were carried out: monotonic tension and compression tests, and compression creep tests. All three types of tests utilized the same equipment. In all tests, the specimen was mounted in the grips of the servo hydraulic machine. First, the top of the specimen was gripped while in displacement control mode, then the load cell reading was zeroed out, and finally the bottom of the specimen was gripped while in force control mode. This procedure ensured that specimen was not subjected to any tensile or compressive loads during gripping.

#### **4.3.1 Monotonic Tension Tests**

The monotonic tension tests were performed on the N610/alumina and N610/monazite/alumina CMCs with both 0°/90° and ±45° fiber orientations. The tests were conducted in displacement control mode at a rate of 0.05 mm/s at room temperature and at 900 °C. The specimens were placed in the 25 kN servo-hydraulic machine with a grip pressure of approximately 8 MPa (1150 psi). The following, Figure 22, shows a tensile specimen properly secured in the grips of the servo-hydraulic testing machine.

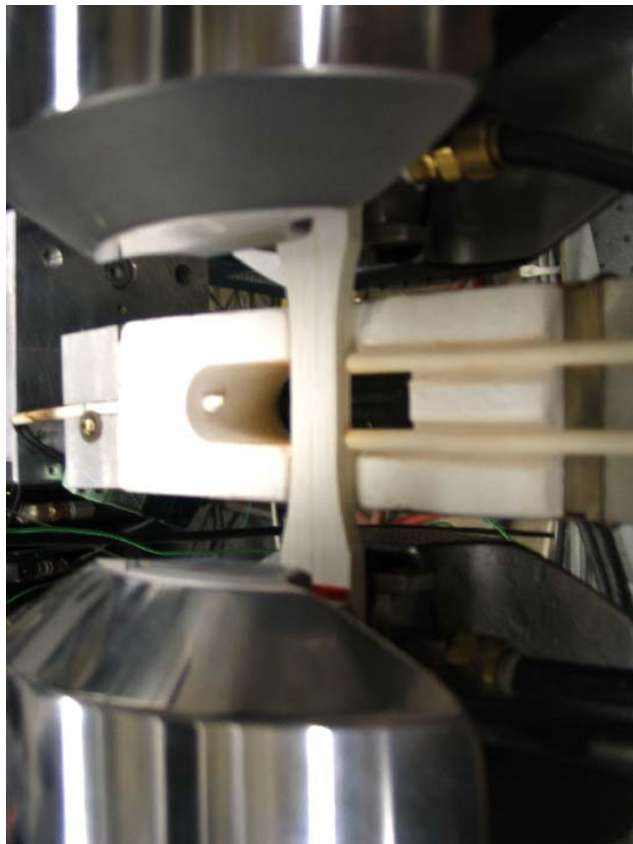


Figure 22. Tensile Specimen Secured in the Grips of the Servo-Hydraulic Machine

For the high temperature tests, the oven was closed around the specimen and temperature was raised at the rate of 1 °C/s. In order to allow the specimen to thermally equilibrate, a

30-minute dwell period was introduced once the test temperature was reached. The same heat-up and dwell procedure was used in all tensile, compressive, and creep tests. After the dwell period, the specimen was subjected to tension to failure. Data collected during temperature ramp up and during the tension test included strain, force, displacement, displacement command, temperature, and time. Displacement command was recorded to ascertain that the feedback was within the acceptable tolerance of the command signal.

#### **4.3.2 Monotonic Compression Tests**

The monotonic compression tests were performed on the N610/alumina and N610/monazite/alumina composites with the 0°/90° fiber orientation. These tests were conducted in displacement control at a rate of 0.05 mm/s. The grip pressure used in the compression tests was 8 MPa (1150 psi) for the 25 kN machine and 5 MPa (750 psi) for the 100 kN (22 kip) machine.

#### **4.3.3 Creep Rupture Tests.**

All creep rupture tests were conducted on the 100 kN (22 kip) with grip pressure of 5 MPa (750 psi). The specimen was loaded to the desired creep stress (load) level at the rate of 2200 N/s, which corresponds to a stress rate of approximately 20 MPa/s. The creep stress levels were chosen to be consistent with those used by Musil et al [34,38] in tensile creep tests. In order to determine the creep load level for each specimen, the desired creep stress level was multiplied by the cross-sectional area of that particular specimen. Creep run-out was set to 100 h. Creep tests were interrupted after 50 h if the creep strain rates remained less than  $10^{-9} \text{ s}^{-1}$ .

#### **4.4 Post Failure Analysis**

##### **4.4.1 Specimen Preparation**

To obtain optical micrographs and scanning electron microscope (SEM) images presented in subsequent sections, the specimens had to be cut and sometimes permanently mounted in a resin mold for polishing of the cut surface. A dicing saw was used to cut the specimens. A water cooling system was used in order to keep the blade cool and eliminate the dust from cutting the specimen. Specimens were cut to permit SEM observation of the fracture surfaces and to view cross-sections of certain specimens under both the optical microscope and the SEM.

The specimens prepared to view cross-sections required polishing. To accomplish this, the specimens were mounted in a resin mold using the Simplimet 2000 manufactured by Buehler. The resin mold was conductive to allow better viewing with the SEM. The molding process was set for a total of five minutes and thirty seconds. The mount was then removed and ready for polishing. Figure 23 shows two mounts containing cross-sections of a specimen.



Figure 23. Pieces of Specimen Mounted in Conductive Resin

The polishing process consisted of five steps using grits of 240 (60  $\mu\text{m}$ ), 400 (30  $\mu\text{m}$ ), and 600 (15  $\mu\text{m}$ ). The final polishing steps used diamond pastes of 0.10 and 0.05  $\mu\text{m}$ . Between each of the grits, the specimen was placed in an ultra sonic bath in order to remove the many resin particles, which sometimes get embedded in the surfaces of the specimens. Polishing was accomplished manually using the PowerPro 5000, manufactured by Buelher (see Figure 24).



Figure 24. Polishing machine

#### 4.4.2 Optical Microscopy.

Optical microscopy was carried out using a Zeiss Stemi SV II Optical Microscope incorporating a Zeiss AxioCam HRc digital camera (see Figure 25). The microscopy was performed at varying levels of magnification. Settings were determined by the best

image that could be retrieved while capturing the information needed. Due to constraints of the equipment some specimens had to be viewed in multiple photos. This was caused by the length of delaminations and/or large fracture surfaces of some specimens. Figure 26 and Figure 27, show the setups used for viewing the specimens.

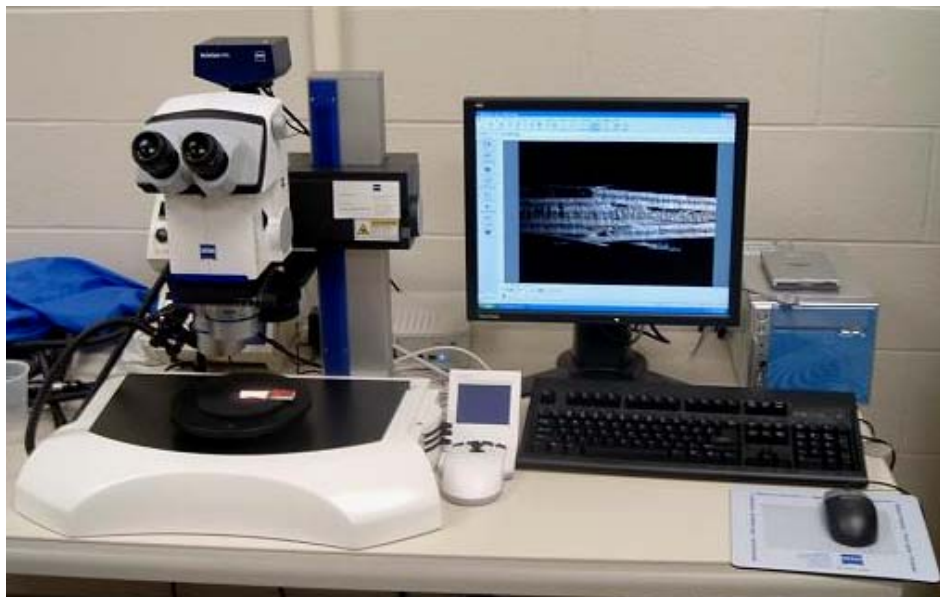


Figure 25. Optical Microscope

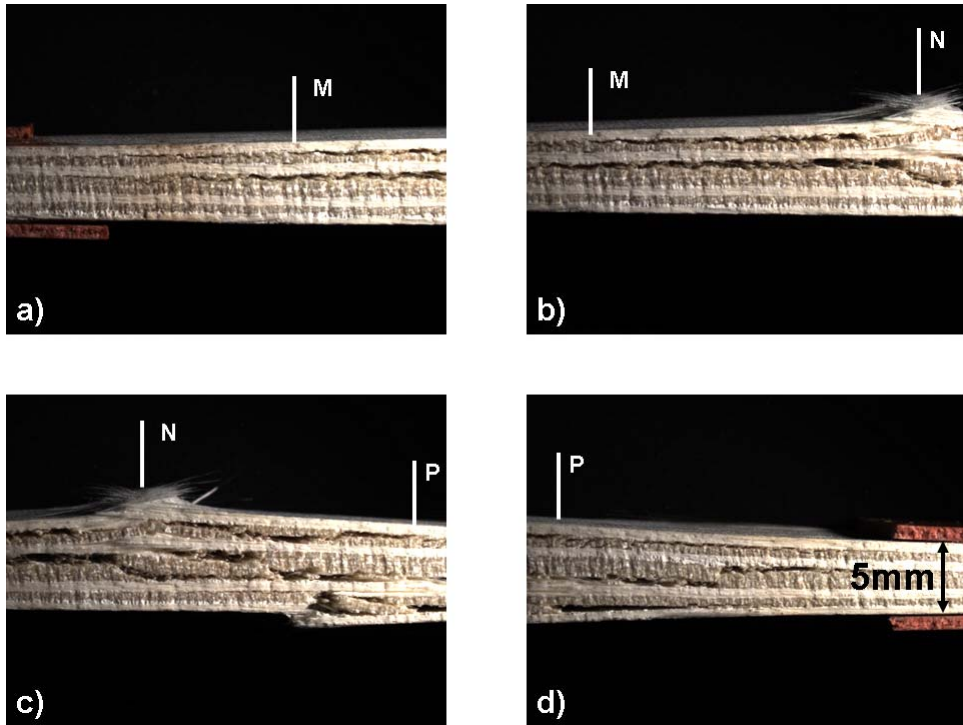


Figure 26. Side View of Specimen

Note a set of markers denoted M, N, and P in Figure 26. These markers represent the points where the views of the specimen needed to be pieced together to form a complete picture. Also seen is the dimension marker. In some cases, not all the photos in a figure set contain scales. However, if there is a single scale in the figure set it applies to all images in a group. A scale was not included with each and every image to avoid crowding. Figure 27, depicts halves of a failed specimen complete with dimensions, a marker ‘F’, and a dimension scale. The marker ‘F’ indicates that fiber pullout can be seen in the optical micrograph. The dimension scale shows the length of the damage zone  $\ell_d$ .

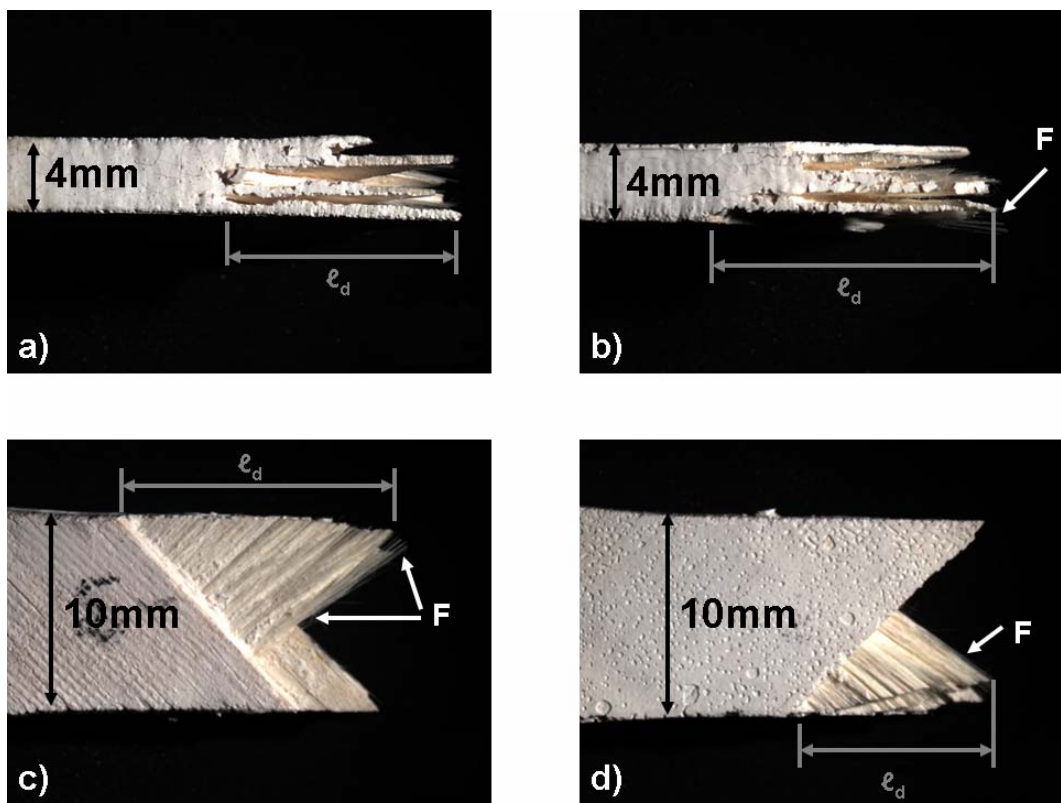


Figure 27. Surface View of Specimen

#### 4.4.3 Scanning Electron Microscope Analysis.

A scanning electron microscope (SEM), seen in Figure 28, can produce high resolution images in three dimensions at high levels of magnification. The SEM works by emitting a beam of electrons, which are focused by two successive condenser lenses into a beam with a spot size of approximately 5 nm [3]. Resolution is dependent on the spot size. The focused primary electrons strike the surface of the sample and are scattered in a non-elastic manner. Interactions in a region created by the scattered electrons, called an interaction volume, lead to the emission of electrons and produce an image [3].

An SEM can have several different modes of operation. Normal high vacuum mode was used with conductive samples. In the case of non-conductive samples, the environmental scanning electron microscopy (ESEM) mode was employed. ESEM operates in what is called a “wet” mode making non-conductive samples conductive. If samples are non-conductive the electrons tend to charge the surface of the sample and make the image really bright and therefore hard to see. To prevent the charging of the specimen surfaces, the specimens were either viewed in ESEM mode or coated with carbon. Sometimes a piece of copper tape was secured to the sides of the specimen to further reduce charging of the specimen surface. Some SEMs are equipped with a back-scatter feature. This feature was used to capture a view of the monazite coating.



Figure 28. Scanning Electron Microscope.

## V. Results and Discussion

This chapter will describe the results of the investigation conducted on the N610/monazite/alumina and N610/alumina specimens. It will begin with a discussion of results of the initial investigation of the off-axis tensile behavior and present the reasons for redirecting the study to focus on the on-axis compression creep behavior. Next, monotonic compression behavior of both the tensile and compression specimens is discussed, followed by discussion of composite microstructure. This chapter concludes with the review of the effects of temperature and fiber coating on creep behavior, as well as, it analyzes problems encountered with some N610/monazite/alumina panels. An in depth analysis, of the monotonic tensile/compressive behavior and microstructure is then reviewed.

### ***5.1 Fiber Volume Ratio Adjustment***

To accurately compare the test data obtained for specimens with different fiber volume fractions, a set fiber volume fraction was selected and then all stress calculations were normalized to that set fiber volume fraction according to the following equation:

$$X_{adj} = X * (V_f \text{ actual} / V_f \text{ set}) \quad (1)$$

where ‘X’ is the quantity being adjusted and  $V_f$  is fiber volume fraction.

### ***5.2 Monotonic Tension – $\pm 45^\circ$ Specimens***

The initial study focused on off-axis tensile creep behavior of N610/monazite/alumina and N610/alumina. In addition to the  $\pm 45^\circ$  specimens, the study

included testing of  $0^\circ/90^\circ$  specimens, which were tested in tension to confirm that the behavior of the panel was consistent that observed earlier. However, both the monazite coated and control specimens with the  $\pm 45^\circ$  fiber orientation produced relatively low values of ultimate tensile strength. Tensile stress-strain curves for specimens with  $0^\circ/90^\circ$  and  $\pm 45^\circ$  fiber orientations are shown in Figure 29. Results presented on Figure 29 were adjusted to the fiber volume fraction of 29.1%. Test results are also summarized in Table 3 where elastic modulus, UTS, strain at UTS, are shown together with the failure stress and failure strain for each fiber orientation.

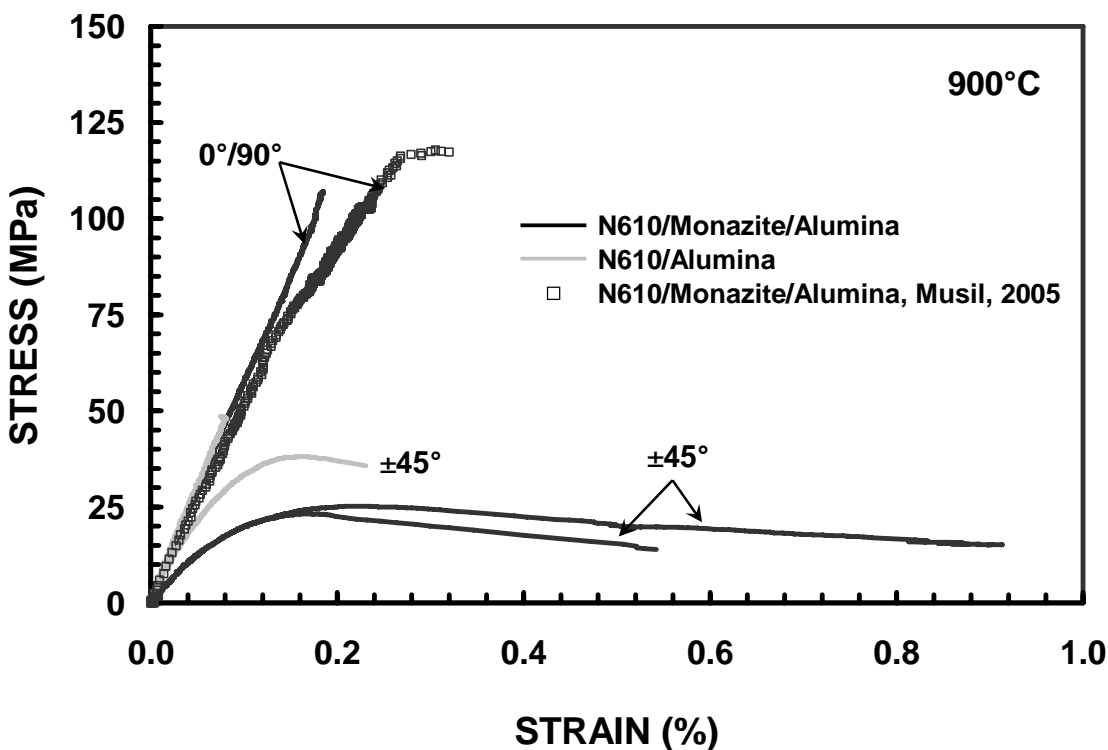


Figure 29. Tensile Stress-Strain Curves for N610/Monazite/Alumina and N610/Alumina Ceramic Composites with  $0^\circ/90^\circ$  and  $\pm 45^\circ$  Fiber Orientation. Data from References [34,38] are Also Shown.

It is seen that the UTS of the  $\pm 45^\circ$  specimens was much lower than that of the  $0^\circ/90^\circ$  specimens. Kerans et al [28:2624] reported similar results for N610 in a porous matrix with  $\pm 45^\circ$  fiber orientation. Table 3, shows the numerical results. It should be noted that this table does not include the data from Musil et al [34,38].

Table 3. Monotonic Properties of On-Axis and Off-Axis Specimens.  $V_f$  Stands for Fiber Volume Fraction.

	<b>Specimen</b>	<b>Material</b>	<b>E</b> (GPa)	<b>UTS</b> (MPa)	<b>Strain<sub>UTS</sub></b> (%)	<b>Strain<sub>f</sub></b> (%)	<b>Stress<sub>f</sub></b> (MPa)
0/90	C1-0-1*	N610/Al <sub>2</sub> O <sub>3</sub>	61.60	52.53	0.47	N/A	N/A
	B1-0-1	N610/LaPO <sub>4</sub> /Al <sub>2</sub> O <sub>3</sub>	55.29	107.00	N/A	0.19	N/A
$-\pm 45$	C1-45-1*	N610/Al <sub>2</sub> O <sub>3</sub>	57.40	38.10	0.16	N/A	27.50
	B1-45-3	N610/LaPO <sub>4</sub> /Al <sub>2</sub> O <sub>3</sub>	27.27	23.19	0.17	0.54	13.90
	B1-45-4	N610/LaPO <sub>4</sub> /Al <sub>2</sub> O <sub>3</sub>	N/A	22.59	N/A	N/A	N/A
	B1-45-5	N610/LaPO <sub>4</sub> /Al <sub>2</sub> O <sub>3</sub>	27.08	25.16	0.22	0.91	N/A

\*: Stress adjusted from  $V_f=35\%$  to  $V_f=29.1$

The low UTS indicated that the off-axis creep behavior could only be investigated for low creep stress levels. With such a low UTS, further investigation of the off-axis creep behavior would not be productive.

### 5.3 Monotonic Compression – Dogbone-Shaped Specimens, $0^\circ/90^\circ$ Fiber Orientation

Results of these tests are presented in Figure 30 and Table 4 and were obtained in compression-to-failure tests on N610/monazite/alumina dogbone-shaped specimens at 900 °C. Compressive stress-strain curves are shown in Figure 30 where the tensile stress-strain curves are also included for comparison. Results in Figure 30 reveal an absolute compressive strength that is almost 40 MPa lower than the UTS. The low compressive strength values suggested that buckling may have been present and, in fact, be the cause

of early failure. Examination of the microstructure of the specimen under an optical microscope confirmed that the specimen experienced buckling, which in turn caused low compressive strength (see Figure 31).

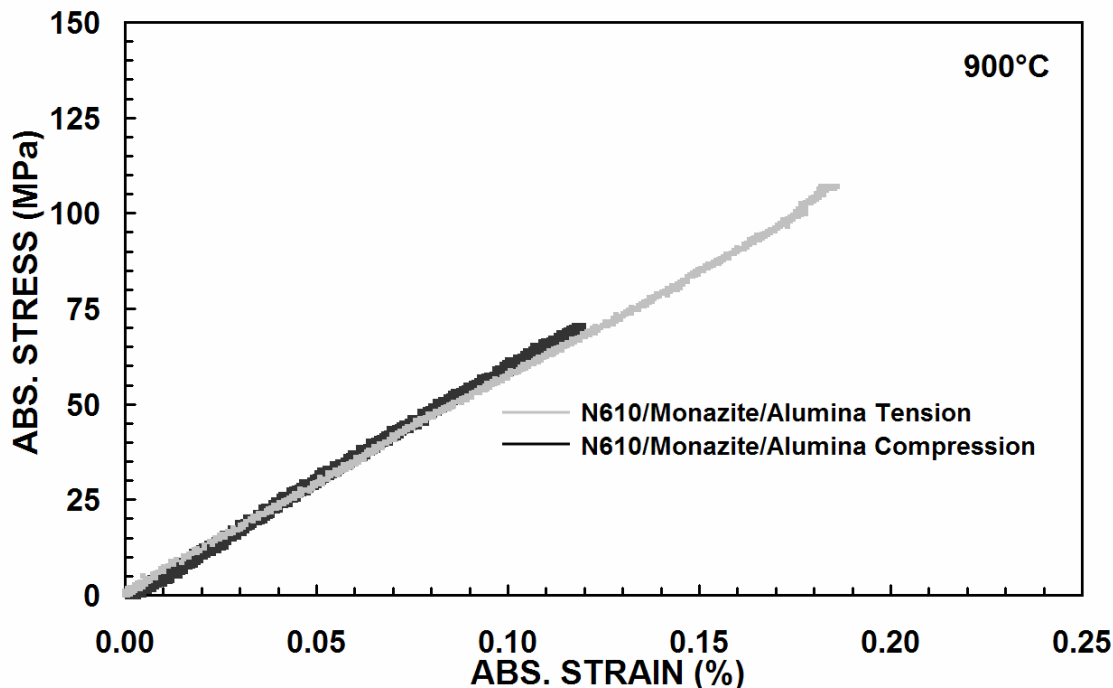


Figure 30. Monotonic Tensile/Compressive Behavior of On-Axis Dogbone-Shaped Specimens at 900 °C

Table 4. Tensile and Compressive Properties of N610/Monazite/Alumina at 900 °C

Specimen	Material	E	UTS	Strain <sub>f</sub>
		(GPa)	(MPa)	(%)
0/90	B1-0-1	N610/LaPO <sub>4</sub> /Al <sub>2</sub> O <sub>3</sub>	55.30	107.00
	B1-0-2	N610/LaPO <sub>4</sub> /Al <sub>2</sub> O <sub>3</sub>	62.70	-69.90

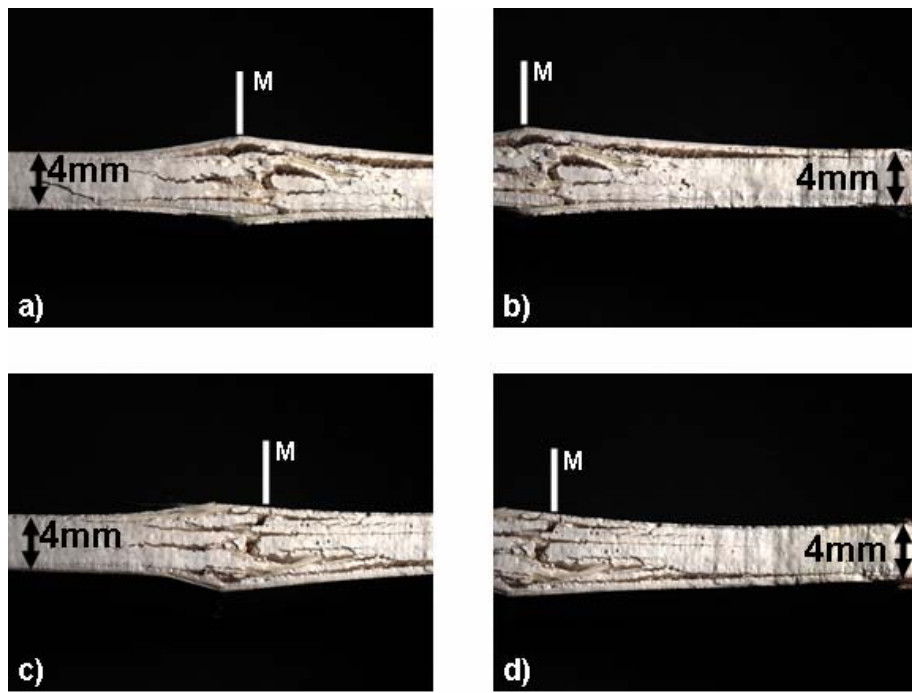


Figure 31. N610/Monazite/Alumina Specimen Tested in Compression at 900 °C Shows an Asymmetric Fracture Surface Suggesting Possible Buckling.

The set of four images in Figure 31 represents the two sides of the specimen; Figure 31a and Figure 31b show one side of the specimen and Figure 31c and Figure 31d the other side. The asymmetric fracture of the specimen, consistent with buckling, is clearly seen in Figure 31. To minimize the possibility of buckling, another compression test was conducted with an anti-buckling device. This test was performed at room temperature, because the anti-buckling device could not withstand 900 °C. A comparison tensile test was also carried out at room temperature. Figure 32 shows the optical micrographs of the specimen tested in compression with the anti-buckling device. The results of the room-temperature tensile and compression tests are presented in Figure 33. Values are shown in Table 5.

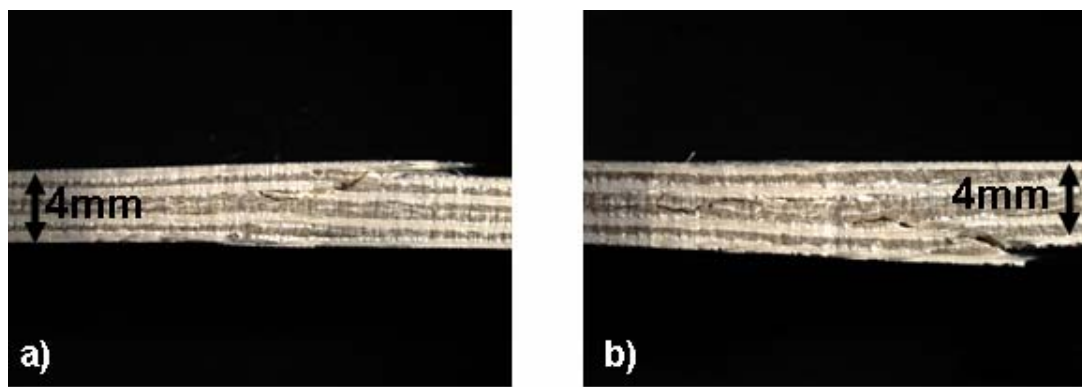


Figure 32. Specimen Tested in Compression with Anti-Buckling Device

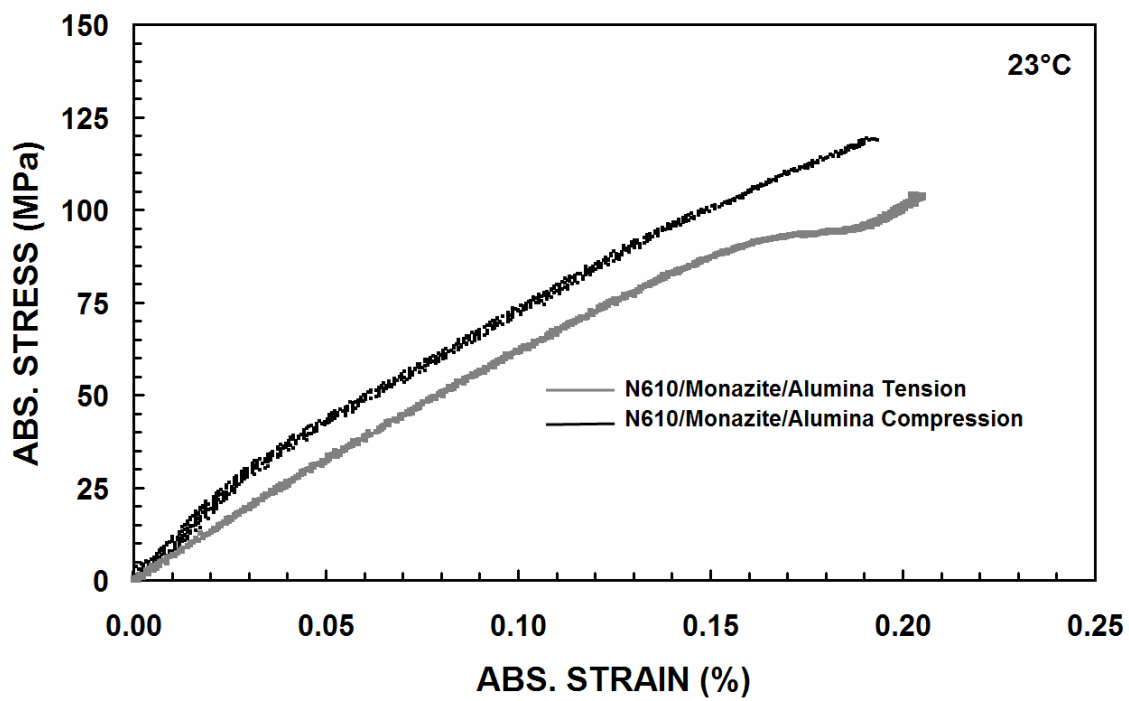


Figure 33. Tensile and Compressive Stress-Strain Curves for N610/Monazite/Alumina at 23 °C. Compression Test Employed Anti-Buckling Device.

Table 5. Tensile and Compressive Properties of N610/Monazite/Alumina at 23 °C.  
Compression Test Employed Anti-Buckling Device.

	Specimen	Material	E	UTS	Strain <sub>f</sub>
			(GPa)	(MPa)	(%)
0/90	B1-0-3	N610/LaPO <sub>4</sub> /Al <sub>2</sub> O <sub>3</sub>	64.10	104.73	0.20
	A1-0-1	N610/LaPO <sub>4</sub> /Al <sub>2</sub> O <sub>3</sub>	61.20	-119.19	-0.19

The room-temperature UTS value of ~105 MPa was consistent with that reported previously. Musil et al [34,38] reported room-temperature UTS for the uncoated fiber composite. However, Keller and Mah [26] reported a 48% increase in UTS for the coated fiber composite. If this increase is applied directly to the UTS value reported by Musil et al [34,38] for the uncoated fiber composite of the coated fiber CMC can be predicted as 173 MPa. Once the fiber volume fraction is adjusted, the UTS value of 98 MPa is obtained. However, of more importance was the compressive strength result. The use of the anti-buckling device resulted in a higher compressive strength confirming that buckling was the cause of low UCS values in previous tests.

#### **5.4 Monotonic Compression – Straight-Sided Specimens, 0°/90° Fiber Orientation**

The following section contains results of monotonic compression of both N610/monazite/alumina and N610/alumina straight-sided specimens at 900 and 1100 °C. These tests were conducted to ensure that the new specimen (shown in Figure 10), straight-sided and of greater width, would withstand buckling.

A total of six compression tests to failure were carried out at 900 and 1100 °C; 3 tests on N610/monazite/alumina specimens and 3 tests on control specimens. Results obtained for both N610/monazite/alumina and N610/alumina CMCs are shown in Figure 34. Note the significantly lower UCS of specimen N1-6. This specimen was cut in the direction perpendicular to that used in cutting other specimens from this panel. The surface layers of this specimen had 90° fiber orientation, while other specimens had surface layers with the 0° fiber orientation.

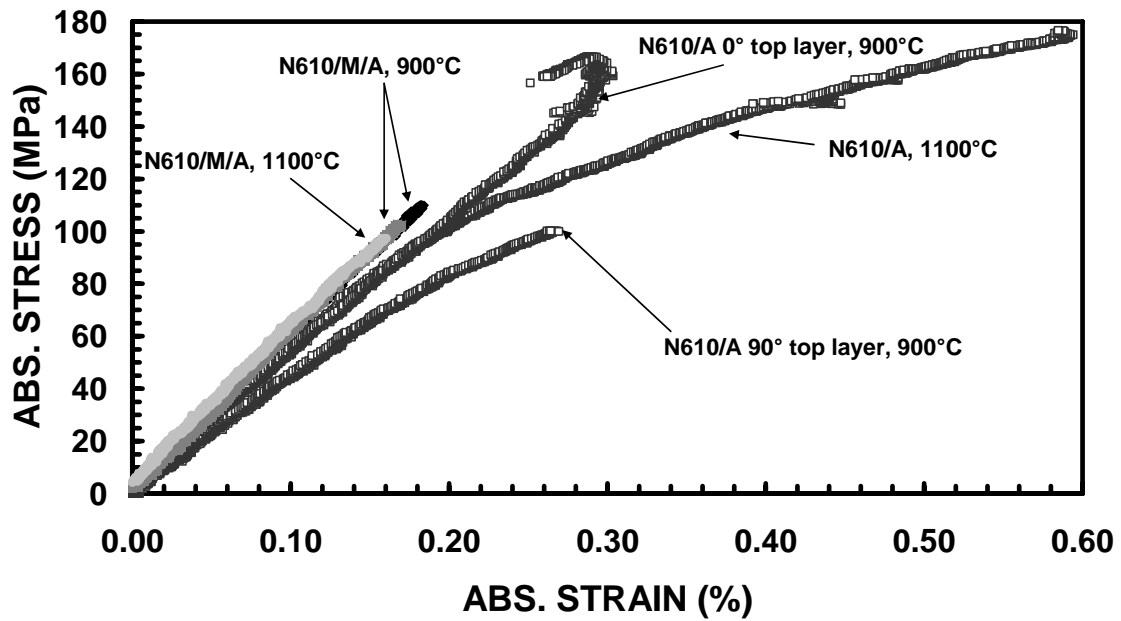


Figure 34. Compression Stress-Strain Curves for N610/Monazite/Alumina and N610/Alumina at 900 °C

The surface layers with the 90° fiber orientation appeared to have compromised the compressive strength of the specimen. The second test at 900 °C produced a much higher UCS. Note that the surface layers of this specimen had 0° fiber orientation. Two tests

were conducted at 900 °C because the first test represented by the black line in Figure 34 exhibited signs of buckling. The asymmetric fracture is noticeable in the optical micrographs Figure 35 and Figure 36. However, as confirmed by the second test at 900 °C, this did not affect the UCS of the specimen. The second test did not show any apparent signs of buckling and produced similar compressive strength values. Monotonic compressive properties of both monazite-containing and control specimens can be seen in Table 6.

Table 6. Compressive Properties of Straight-Sided N610/Monazite/Alumina and N610/Alumina Specimens at 900 and 1100 °C

Specimen	Material	Test Temperature °C	E (GPa)	UCS (MPa)	Strain <sub>UCS</sub> (%)	Strain <sub>f</sub> (%)	Stress <sub>f</sub> (MPa)
M1-1	N610/LaPO <sub>4</sub> /Al <sub>2</sub> O <sub>3</sub>	900	47	110	N/A	N/A	N/A
M1-2	N610/LaPO <sub>4</sub> /Al <sub>2</sub> O <sub>3</sub>	900	58	103	N/A	N/A	N/A
M1-3	N610/LaPO <sub>4</sub> /Al <sub>2</sub> O <sub>3</sub>	1100	63	97	0.16	N/A	N/A
N1-6*	N610/Al <sub>2</sub> O <sub>3</sub>	900	37	100	0.27	N/A	N/A
N1-7*	N610/Al <sub>2</sub> O <sub>3</sub>	1100	53	177	0.59	N/A	N/A
N1-8*	N610/Al <sub>2</sub> O <sub>3</sub>	900	52	166	0.29	0.25	157

\*: Stress adjusted from V<sub>f</sub>=36% to V<sub>f</sub>=26

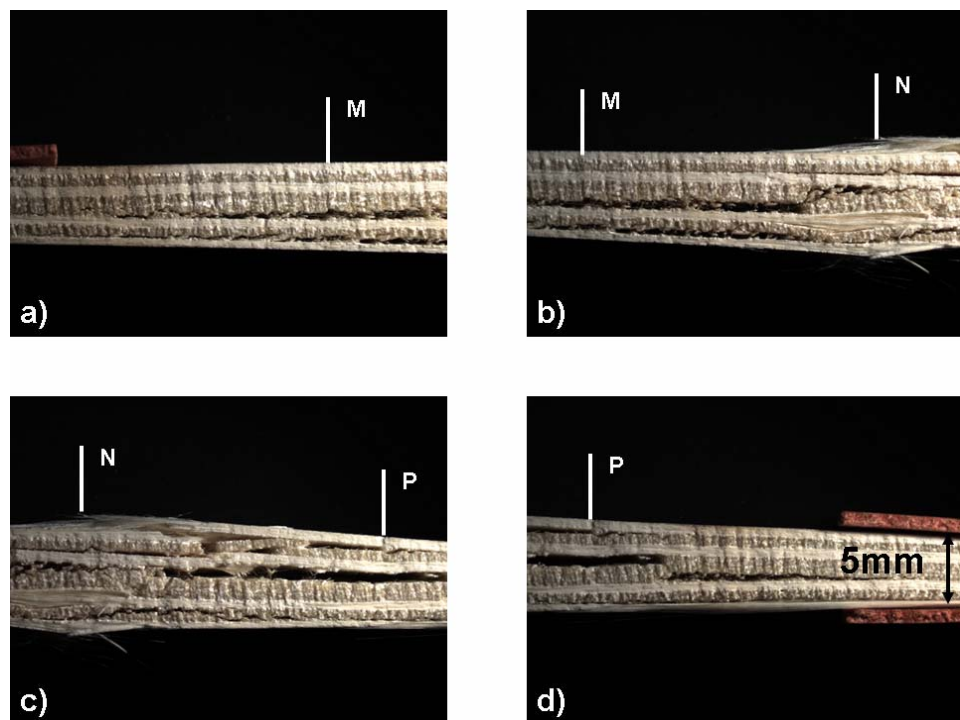


Figure 35. Side 1 of N610/Monazite/Alumina Specimen Asymmetric Fracture Suggests Buckling

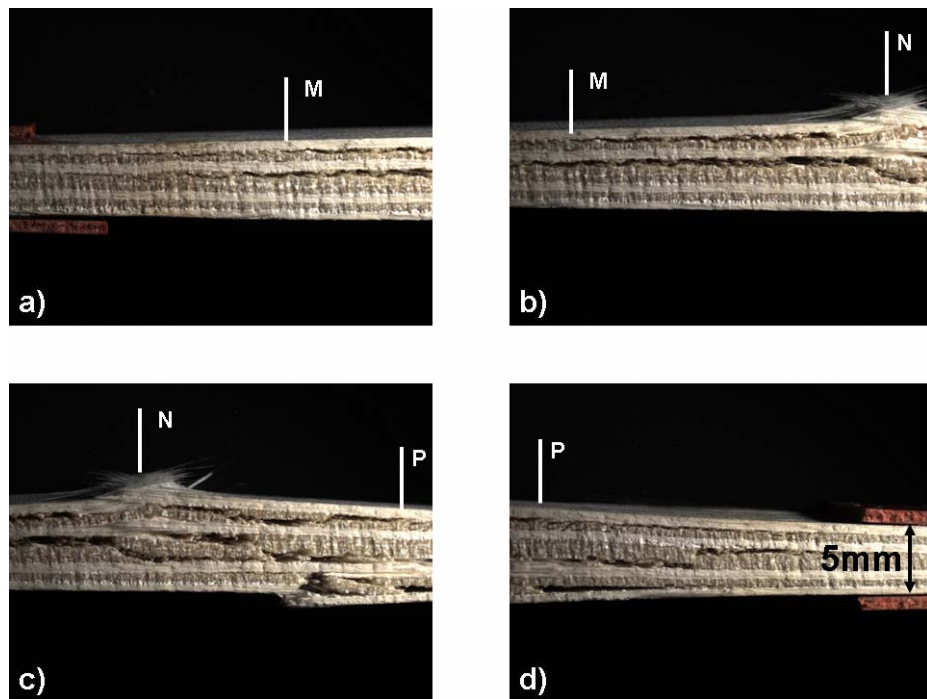


Figure 36. Side 2 of N610/Monazite/Alumina Specimen Asymmetric Fracture Suggests Buckling

## 5.5 Microscopy

This section presents the optical micrographs of all specimens discussed above. It will compare and contrast fracture appearance of various N610/monazite/alumina and N610/alumina specimens focusing on fiber pullout, delamination, and damage zone size.

### 5.5.1 Specimens Tested in Tension

Figure 37 and Figure 38, show one half of a N610/monazite/alumina  $\pm 45^\circ$  tensile specimen and N610/alumina  $\pm 45^\circ$  tensile specimen, respectively. Both were tested in tension at 900 °C.

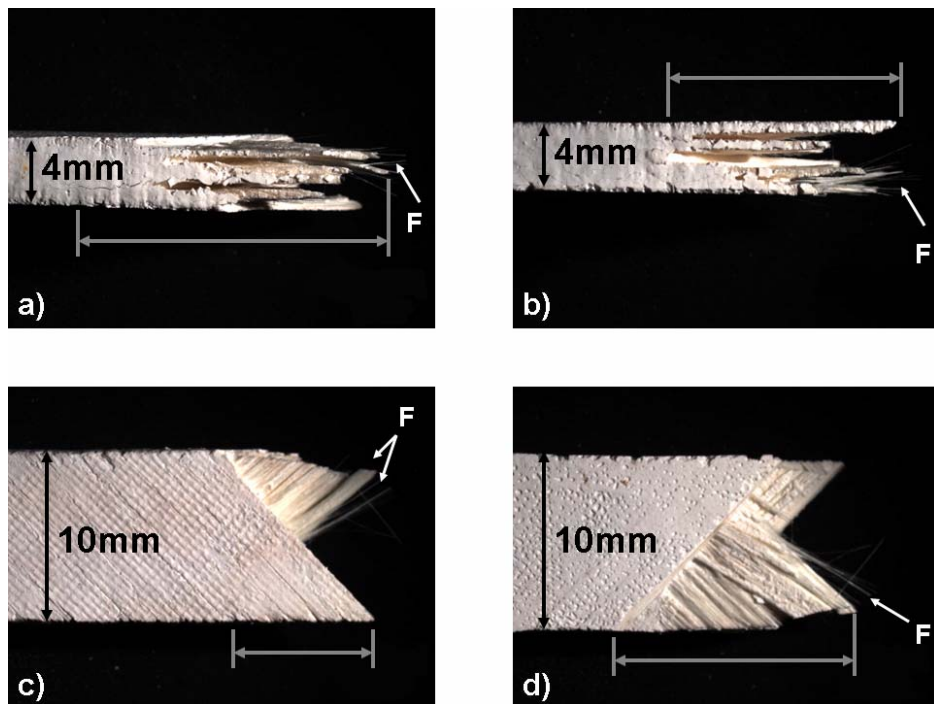


Figure 37. N610/Monazite/Alumina Specimens with  $\pm 45^\circ$  Fiber Orientation Tested in Monotonic Tension at 900 °C

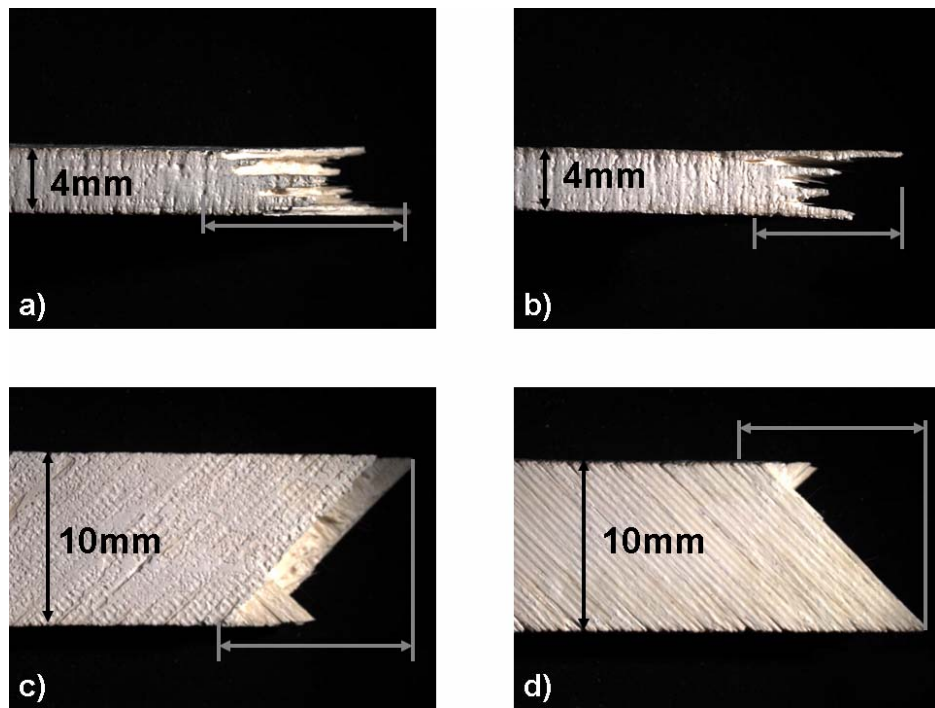


Figure 38. N610/Alumina Specimens with  $\pm 45^\circ$  Fiber Orientation Tested in Monotonic Tension at 900 °C

Both samples showed fracture along the fiber direction as expected. Damage zones were more pronounced in the monazite-containing sample, which also showed visible signs of fiber pullout. Relatively little delamination was observed in the control specimen. It appears that the control specimen failed in a brittle manner along the fiber direction. The more severe delamination and fiber pullout evident in the monazite-containing sample suggested a delayed failure. However, as seen in Figure 29 and in Table 3, the control specimen exhibited higher strength than the monazite-containing specimens. While the contribution of the fibers to the tensile strength of the composite with  $\pm 45^\circ$  fiber orientation is not always readily predicted, it is recognized that the tensile behavior of the  $\pm 45^\circ$  cross-ply is not fiber-dominated and relies considerably more on matrix for strength than the  $0^\circ/90^\circ$  cross-ply. This may explain why the control specimen with  $\pm 45^\circ$  fiber

orientation exhibited higher strength than  $\pm 45^\circ$  monazite-containing specimen. Monazite isolates the fiber from the matrix creating a weak fiber/matrix interface, which lessens the fiber contribution to the composites tensile strength in a given lay-up. Conversely, in a control specimen the fiber is bonded directly to the matrix and is therefore able to contribute to the composite's tensile strength.

Figure 39 shows half of a N610/monazite/alumina specimen with  $0^\circ/90^\circ$  fiber orientation tested in tension at  $900\text{ }^\circ\text{C}$ . The fiber pullout is apparent in Figure 39(c) and (d). This fiber orientation exhibits a lot more fiber pullout than the  $\pm 45^\circ$  specimen. No clear evidence of delamination is seen in Figure 39(c) and (d).

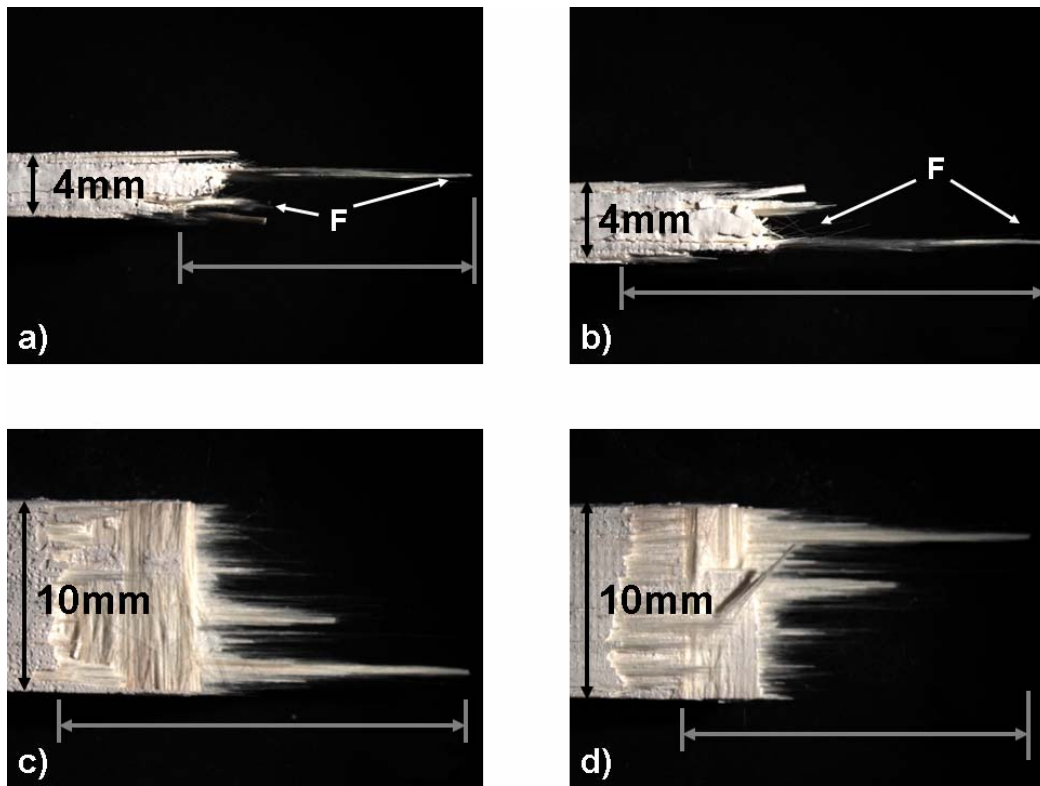


Figure 39. N610/Monazite/Alumina Specimen with  $0^\circ/90^\circ$  Fiber Orientation Tested in Tension at  $900\text{ }^\circ\text{C}$

### 5.5.2 Specimens Tested in Compression

The damage zones produced in compression were more exaggerated, furthermore the delamination was more pronounced. Figure 40 shows a N610/monazite/alumina dogbone-shaped specimen tested in compression at 900 °C without aid of the anti-buckling device.

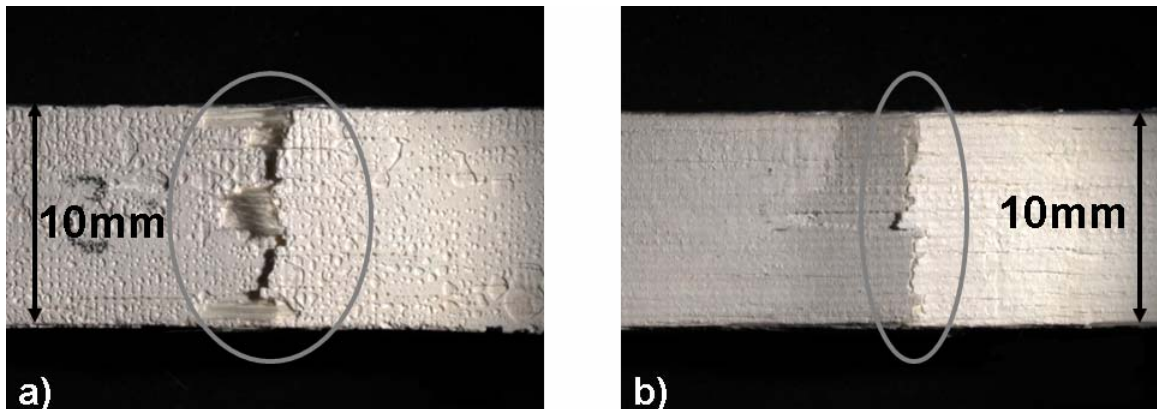


Figure 40. Dogbone-Shaped N610/Monazite/Alumina Specimen with 0°/90° Fiber Orientation Tested in Compression at 900 °C without the Anti-Buckling Device

Surface views in Figure 40(a) and (b), show relatively small damage zones (damage zones are marked with ovals). However, a side-view of the specimen, presented in Figure 41, shows the full extent of the damage. Note that marker ‘M’ identifies the same location in the specimen. Thus, Figure 41(a) and (b) together present a full view of the damage zone on the specimen side. Similarly Figure 41(c) and (d) give a full view of the damage zone on the opposite side of the specimen. The dimension lines in Figure 41(a), (b), (c), and (d) bracket the damage zones.

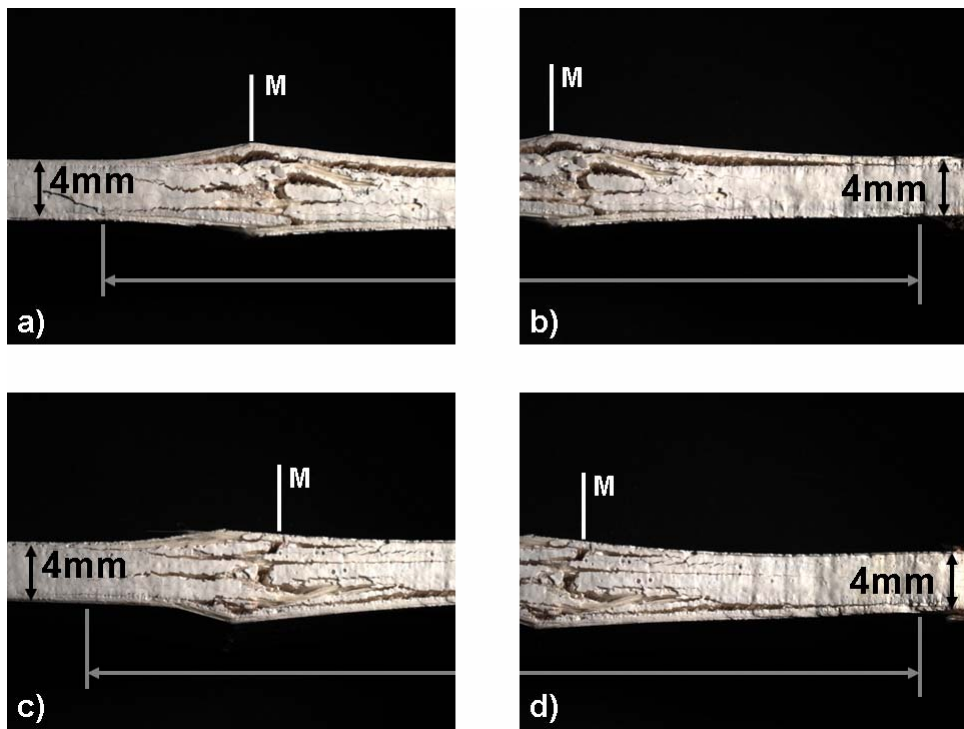


Figure 41. Dogbone-Shaped N610/Monazite/Alumina Specimen with 0°/90° Fiber Orientation Tested in Compression at 900 °C without the Anti-Buckling Device

The damage zones shown in Figure 41(a) and (b) extend for ~34 mm while the damage zone shown in Figure 41(c) and (d) is ~36 mm long. It is noteworthy that the specimen tested in compression at room temperature with an anti-buckling device exhibits a similar amount of damage on the surfaces of the specimen (damage enclosed by gray ovals in Figure 42(c) and (d)). However, the side-views of the specimen, shown in Figure 42(a) and (b), exhibit significantly less delamination and shorter damage zones. The damage zones shown in Figure 42(a) and (b) were approximately 18 mm and 20 mm long, respectively. Both the anti-buckling device and the lower temperature may be the cause of the limited delamination and shorter damage zones.

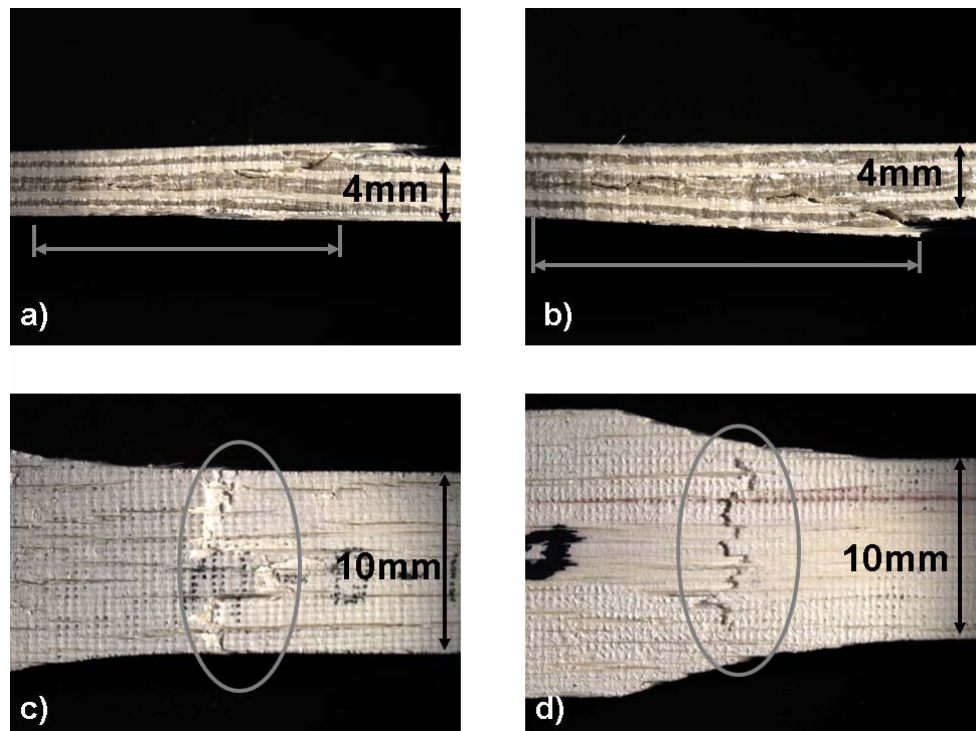


Figure 42. Dogbone-Shaped N610/Monazite/Alumina Specimen with  $0^\circ/90^\circ$  Fiber Orientation Tested in Compression with the Anti-Buckling Device at  $23^\circ\text{C}$ .

Images of the straight-sided  $0^\circ/90^\circ$  specimens of both N610/monazite/alumina and N610/alumina tested in compression at  $900$  and  $1100\text{ }^\circ\text{C}$  are shown in Figure 44 through Figure 48.

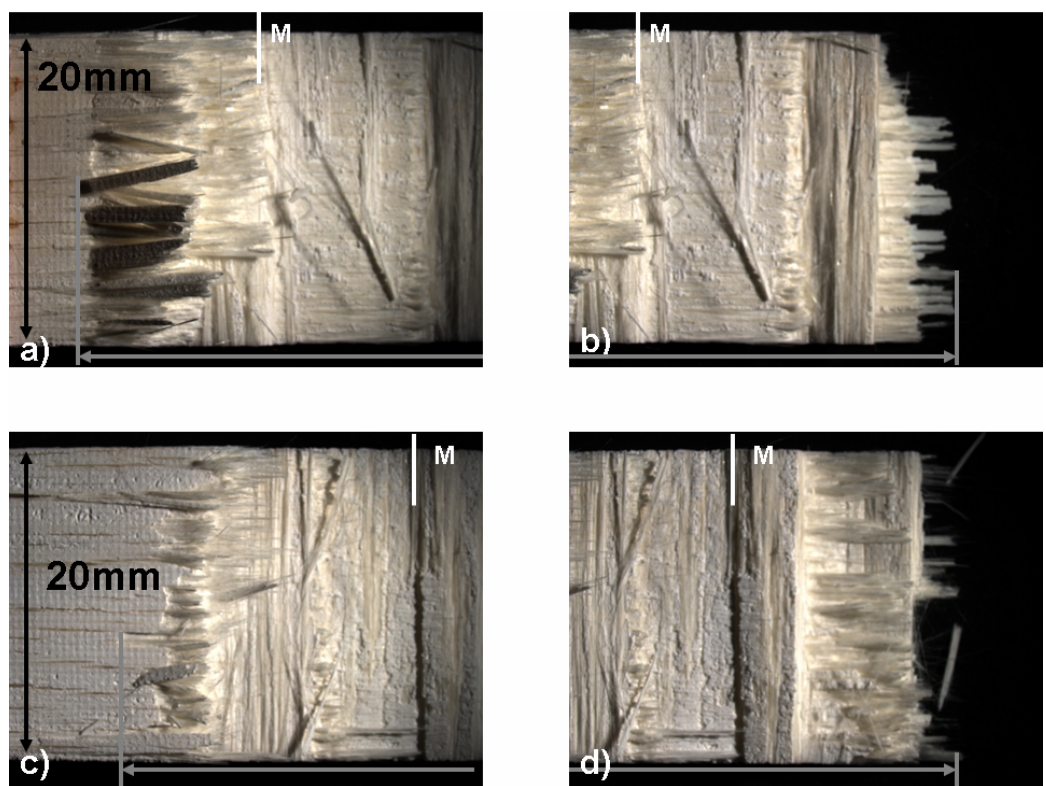


Figure 43. Straight-Sided N610/Monazite/Alumina 0°/90° Specimen Tested in Compression at 900 °C

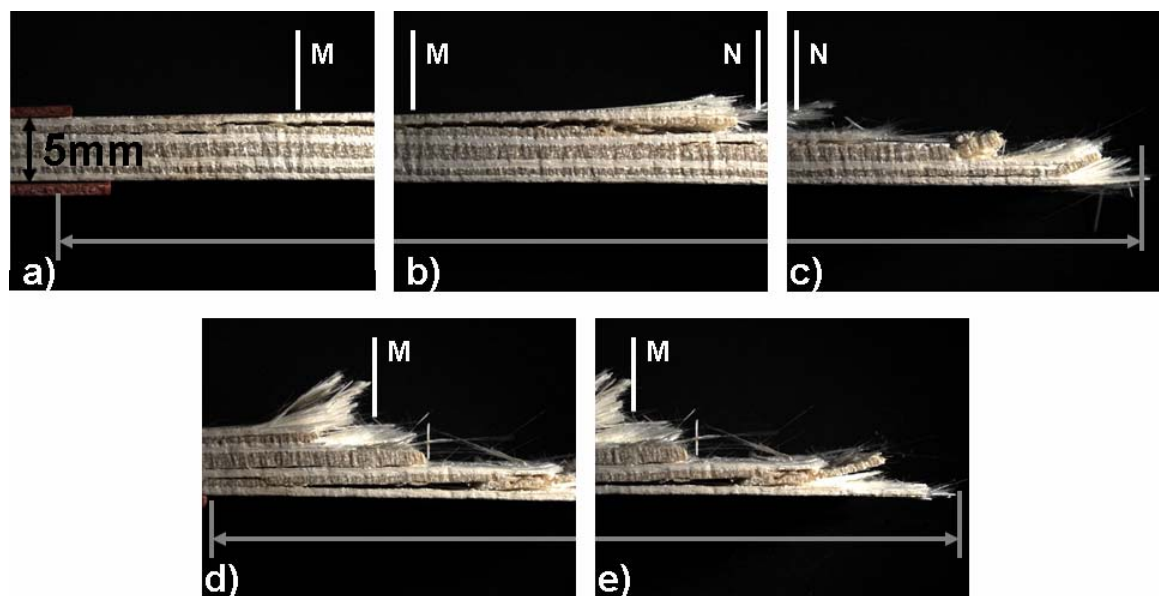


Figure 44. Side Views of a Straight-Sided N610/Monazite/Alumina 0°/90° Specimen Tested in Compression at 900 °C

Shown in Figure 43 is a straight-sided  $0^\circ/90^\circ$  N610/monazite/alumina specimen tested at  $900^\circ\text{C}$  in compression. Figure 43(a) and (b) show one half of the failed specimen and Figure 43(c) and (d), the other half. The damage zones in both halves are approximately 33 mm in length. The fiber pullout is readily seen in both halves of the specimen. The side views of this specimen, shown in Figure 44, reveal the step wise topography of the specimen fracture. Again both the fiber pullout and the extensive delamination are readily seen in these images. In the connected image of Figure 44(a), (b), and (c) the damage zone extends for about 70 mm. The other half of the specimen (see Figure 44(d) and (e)) exhibited a much shorter damage zone of approximately 37 mm.

At  $1100^\circ\text{C}$ , the straight-sided specimen produced shorter damage zones, yet fiber pullout and extensive delamination were still evident (see Figure 45 and Figure 46).

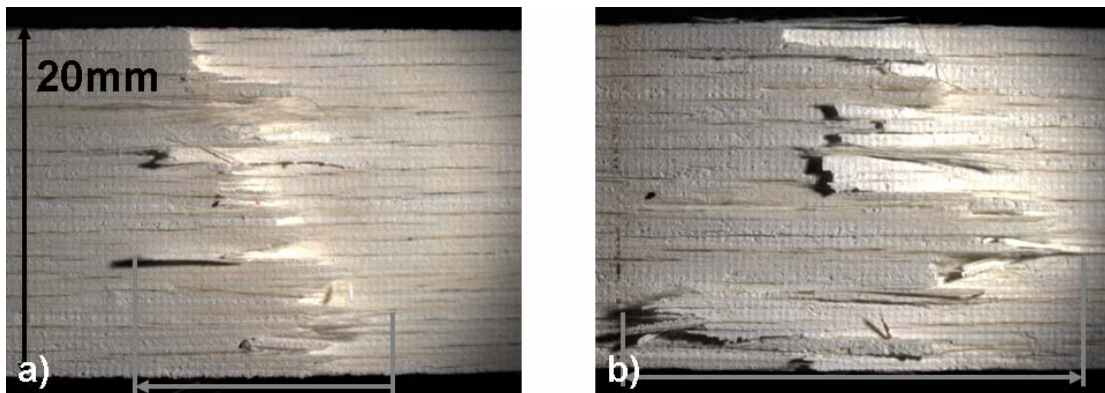


Figure 45. Straight-Sided N610/Monazite/Alumina  $0^\circ/90^\circ$  Specimen Tested in Compression at  $1100^\circ\text{C}$

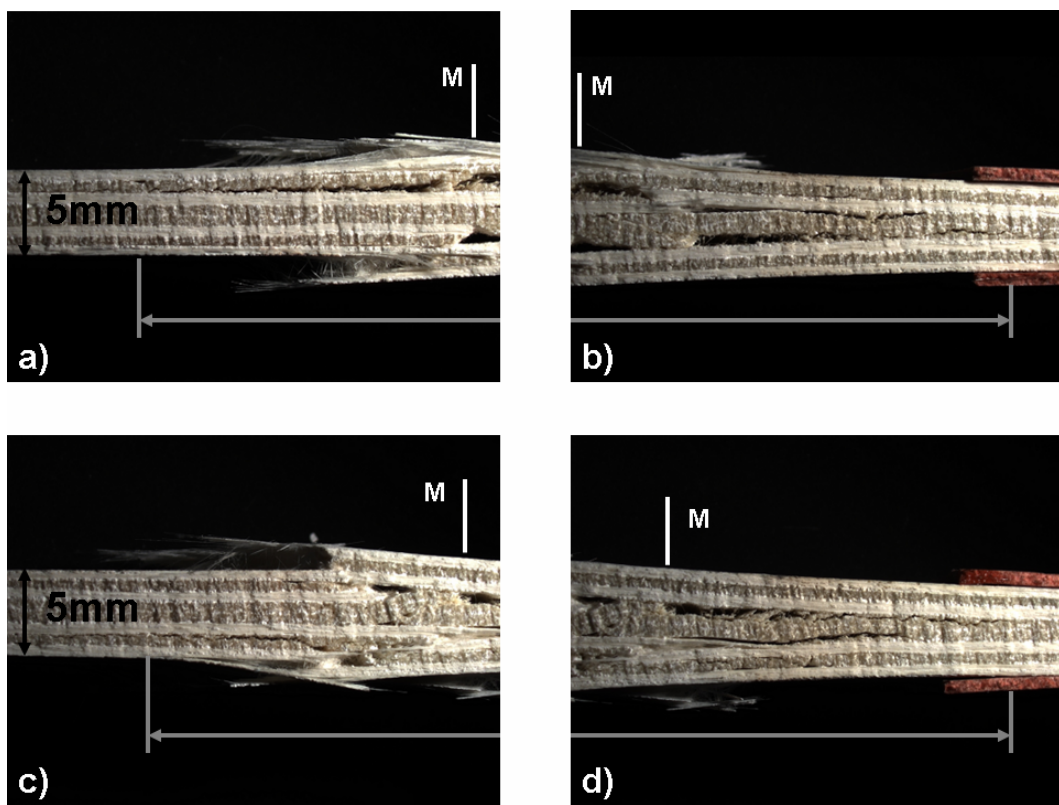


Figure 46. Side Views of the Straight-Sided N610/Monazite/Alumina 0°/90° Specimen Tested in Compression at 1100 °C

Side views of the specimen seen in Figure 46 reveal damage zones between 36 and 42 mm in length. Note that the micrographs of the monazite-containing specimens tested at 900 °C are similar to those produced at 1100 °C.

It is instructive to compare the damage zones and delamination patterns produced in the control and monazite-containing specimens. Figure 47 shows a N610/alumina specimen tested in compression at 900°. Virtually no fiber pullout is seen.

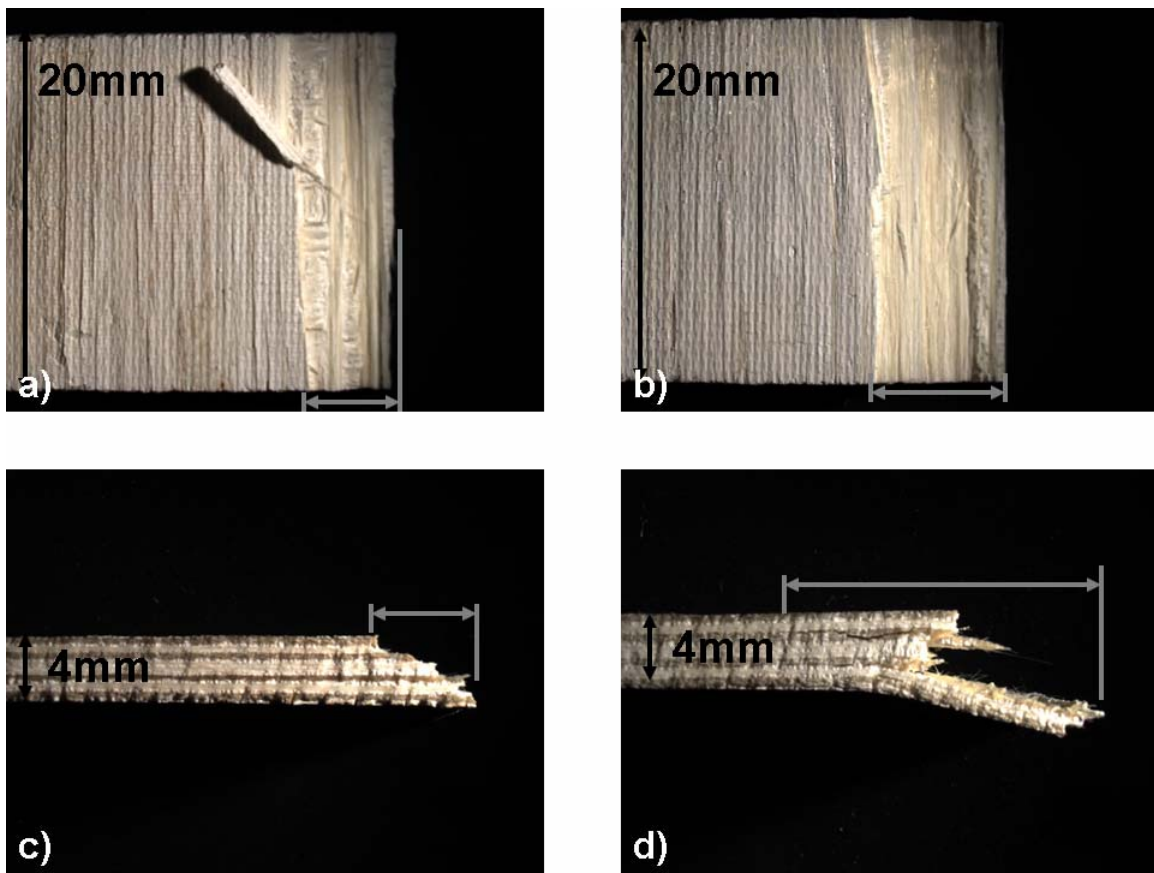


Figure 47. Straight-Sided N610/Alumina 0°/90° Specimen Tested in Compression at 900 °C

Figure 47(a) and (c) show the same half of the specimen. Both views reveal the same short damage zone. No cracks or delamination are seen along the side of the specimen. The damage zone was approximately 6 mm in length. The damage zones seen in Figure 47(b) and (d) were approximately 7.31 and 15 mm, respectively. These damage zones are substantially shorter to those seen in the monazite-containing specimen at both 900 and 1100 °C. In the absence of monazite, the specimen acts more like a monolithic ceramic than a composite.

At 1100 °C, N610/alumina specimens produced fracture topography that was closer to that produced by N610/monazite/alumina specimens tested in compression at both 900

and 1100 °C. As seen in Figure 48, the control specimen tested at 1100 °C exhibited more delamination, more jagged fracture topography, and larger damage zones than the control specimen tested at 900 °C.

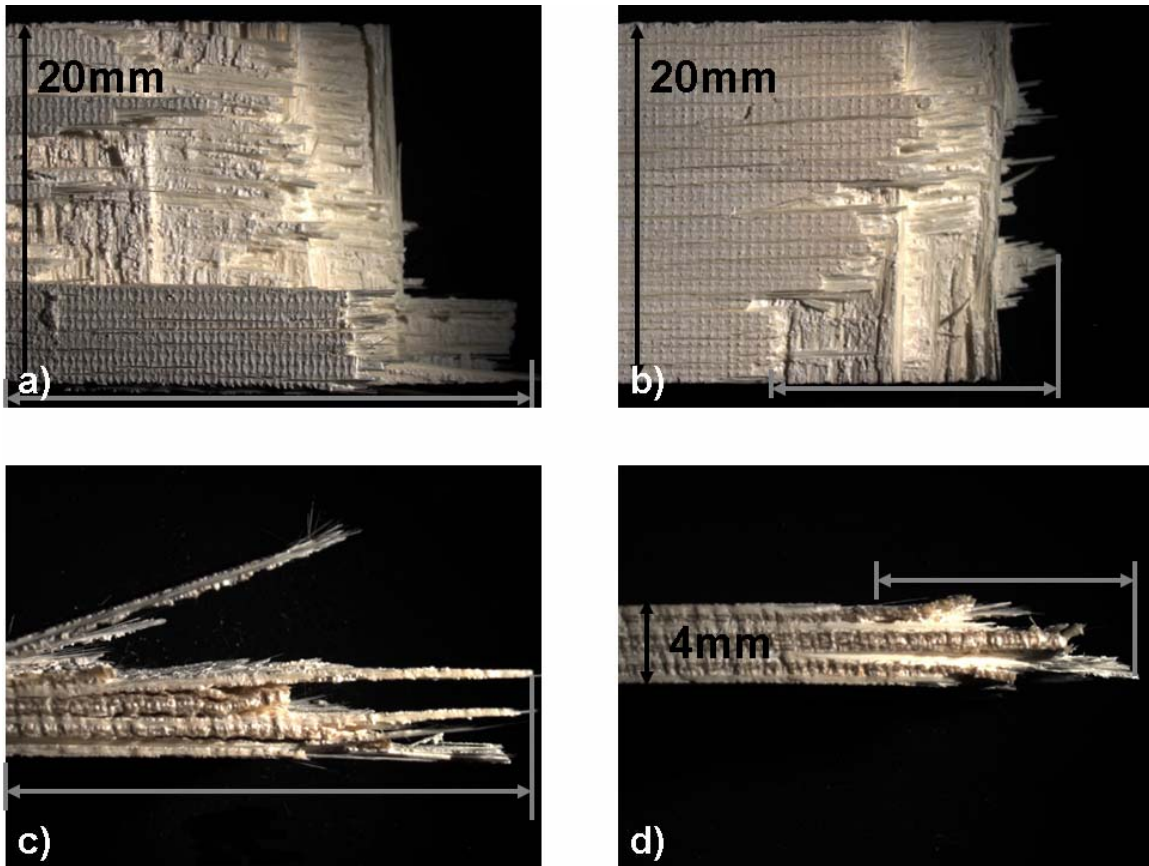


Figure 48. Straight-Sided N610/Alumina 0°/90° Specimen Tested in Compression at 1100 °C

The damage zones shown in Figure 48(a) and (b) were about 27 and 16 mm, respectively. The damage zones seen in the side views in Figure 48(c) and (d) were of the same length as those in Figure 48(a) and (b) because delamination did not extend past the damage on the surface of the specimen. The fracture topography obtained at 1100 °C was less planar than that obtained at 900 °C.

## **5.6 Compressive Creep Behavior**

This section discusses the compression creep tests conducted on N610/monazite/alumina and N610/alumina specimens at 900 and 1100 °C. It will begin with a discussion of the effects of applied stress and temperature on creep response followed by an examination of creep strain rates at various stress levels. Next, the compressive creep behavior will be compared to the tensile creep results reported by Musil et al [34,38]. Retained properties of the material are examined for specimens that achieved a run-out in compressive creep. Finally, microstructure of the composite is examined thoroughly and discussed in detail.

### **5.6.1 Effect of Stress Level and Temperature**

Compression creep tests were conducted at 1100 °C at stress levels of 50, 60, and 75 MPa. These stress levels were chosen as comparable to those used in prior investigation of tensile creep [34,38]. Musil conducted tensile creep tests at 1100 °C at the stress levels of 40, 80, 100, and 120 MPa. These stress values were adjusted for the fiber volume fraction of the monazite-containing specimens used in compression tests to yield 50, 60, and 75 MPa. Results of compressive creep tests are presented in Figure 49 , where creep strain is plotted as a function of time. Note the y-axis shows percent strain in absolute (ABS) value.

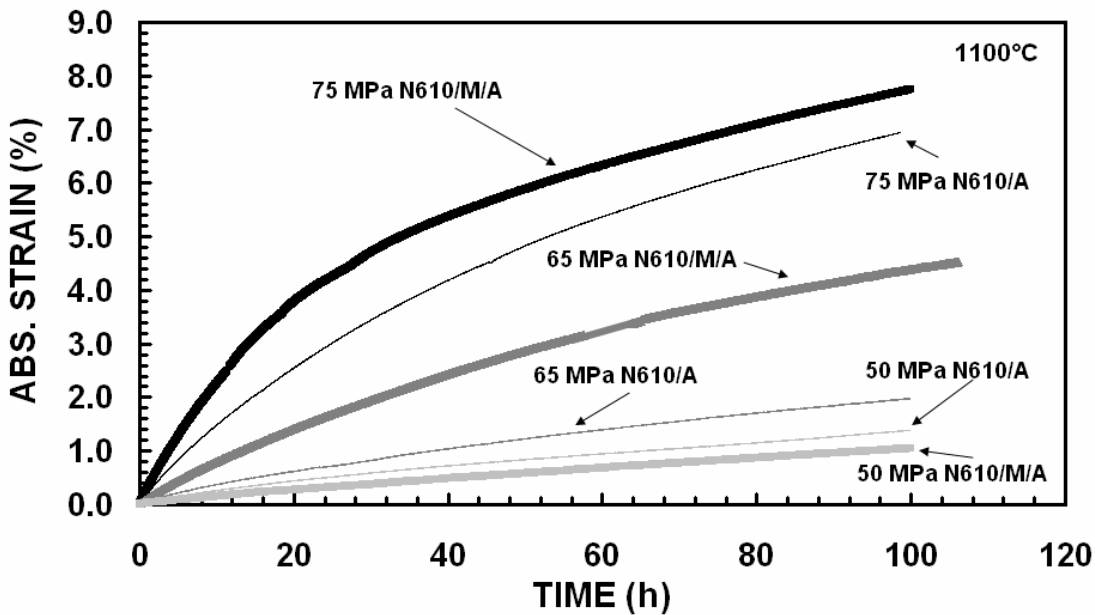


Figure 49. Compressive Creep Strain as a Function of Time for N610/Monazite/Alumina and N610/Alumina Composites at 1100 °C

Specimens tested at all stress levels exhibited extensive amounts of creep. The N610/monazite/alumina CMC accumulated more creep strain at all stress levels than the control composite. Creep strains accumulated at 50 MPa represent an exception. At this stress level the uncoated fiber composite accumulated slightly more creep strain than the monazite-containing CMC. This anomaly may be due to data scatter. While subjected to compressive creep, control specimens with a strong fiber-matrix bond respond more like a monolithic ceramic producing smaller creep strain. Conversely, the weak fiber-matrix interface in the monazite-containing CMC effectively isolates the fibers, leaving the matrix to bear the compressive load, while the fibers are microbuckling (or kinking). Without the reinforcement from the fibers, the matrix responds by progressive cracking and larger creep strains.

Tests conducted at 900 °C revealed that temperature had a major effect on the creep response of these composites. As in the case of 1100 °C tests, creep stress levels were chosen to be consistent with those used in tensile creep testing conducted by Musil et al [34,38] at 900 °C. Musil et al [34,38] conducted tensile creep tests at stress levels of 80, 120, 130, 140, and 150 MPa. These stress levels were adjusted for fiber volume fraction of compression specimens to yield 50, 75, 80, 90, and 95 MPa. Control specimens were subjected to creep at 50, 75, and 95 MPa. One monazite-containing specimen was tested in creep at 50 MPa. Results are presented in Figure 50.

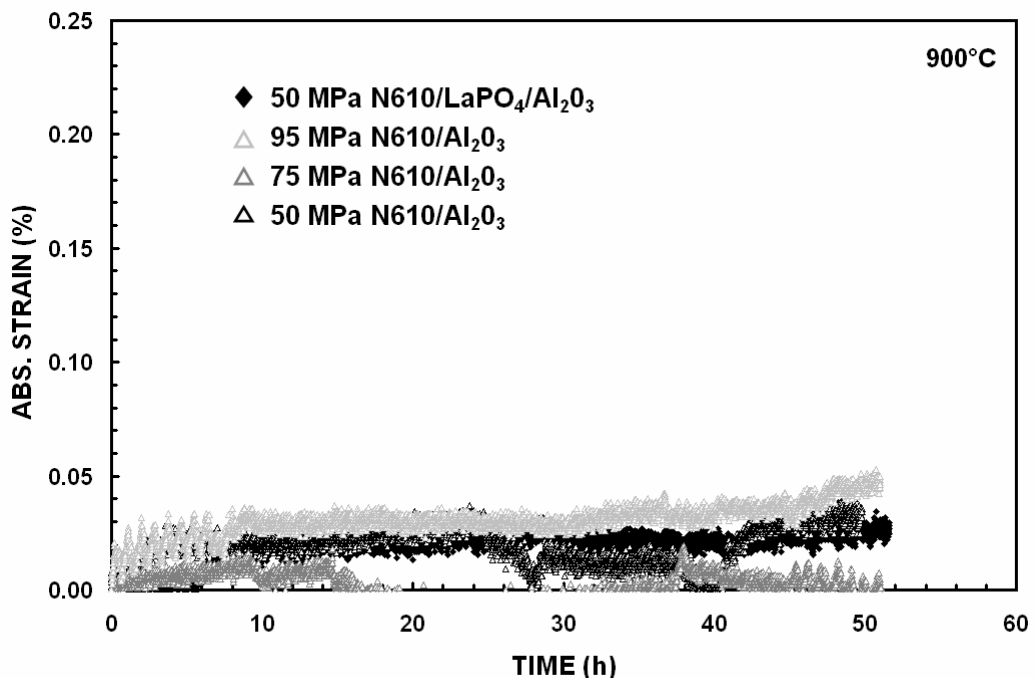


Figure 50. Compressive Creep Strain as a Function of Time for N610/Monazite/Alumina and N610/Alumina Composites at 900 °C

As seen in Figure 50, all tests accumulated only small amounts of strain. All creep strains were no greater than ~0.05%. Tests were terminated after 50 h because of minimal creep strain accumulations and very small creep strain rates.

While no additional N610/monazite/alumina specimens were available for compressive creep testing at 900 °C, the results could be anticipated. Considering the small creep strain produced in all 900 °C tests, it can be conjectured that the monazite-containing samples would accumulate only very low creep strains at 900 °C, regardless of the applied stress level.

### 5.6.2 Creep Strain Rate as a Function of Applied Stress

Figure 51, shows creep strain rate as a function of applied stress at 1100 °C.

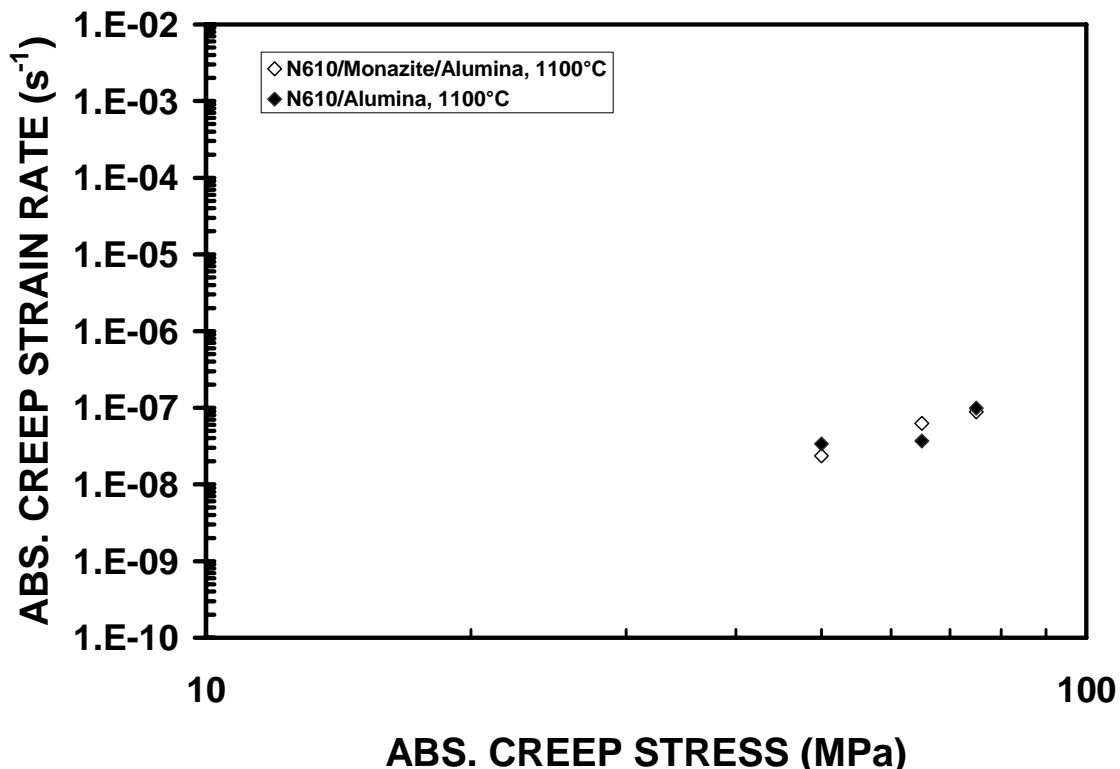


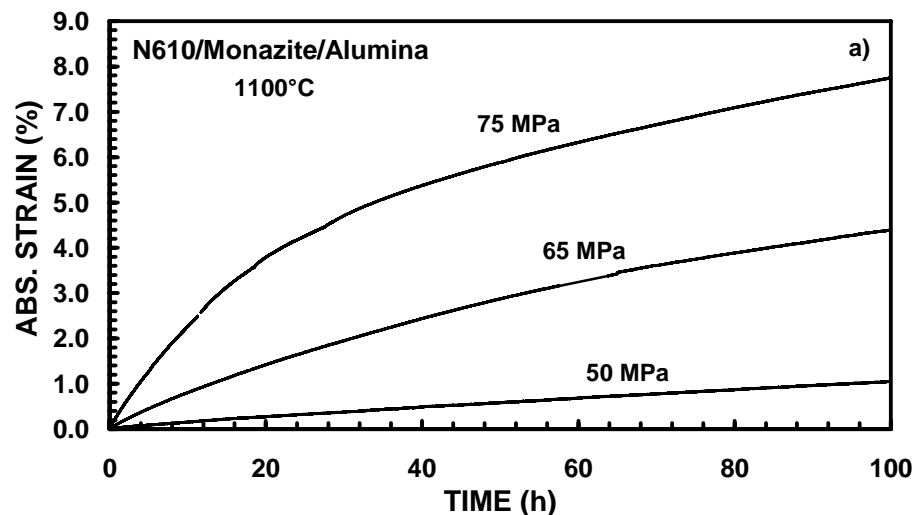
Figure 51. Compressive Creep Strain Rates as a Function of Applied Stress for N610/Monazite/Alumina and N610/Alumina Composites at 1100 °C

Creep strain rates for both N610/monazite/alumina and N610/alumina composites were almost the same at each stress level and increased only slightly with increasing stress.

Creep strain rates at 1100 °C ranged between  $2.36\text{--}9.83 \times 10^{-8} \text{ s}^{-1}$ . Creep strain rates produced in compressive creep tests at 900 °C, were less than  $10^{-10} \text{ s}^{-1}$ . Creep strain rates were obtained by determining the slope of the steady-state portion of each compressive creep curve.

### 5.6.3 Compressive Versus Tensile Creep Behavior

A direct comparison of tensile to compressive creep behavior could not be done because of the different failure mechanisms associated with each. While fibers do not play as vital a role in the strength of the composite material under compression as they do in tension, the results reported by Deng [17] revealed for a SiC fiber-reinforced ceramic matrix composite that specimens with a 0° fiber orientation accumulated less compressive creep strain, had lower creep strain rates at a given stress level, and longer creep lives. Therefore some indirect comparisons can be made between the results presented here and those reported by Musil et al [34,38]. Tensile and compressive creep curves for N610/monazite/alumina composite are shown in Figure 52(a) and (b), respectively.



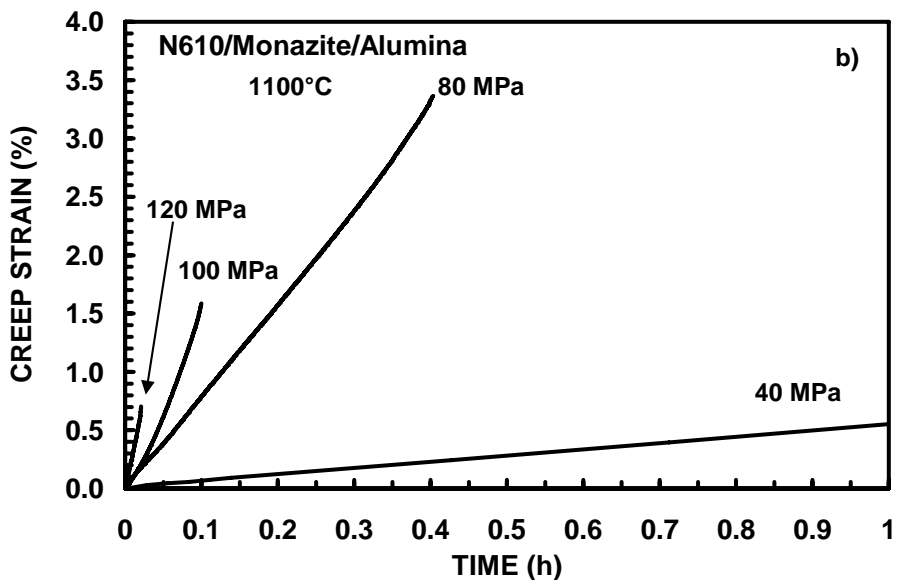


Figure 52. Creep Curves for N610/Monazite/Alumina Composite at 1100 °C: (a) Compressive Creep and (b) Tensile Creep [34,38]

Note that specimens subjected to tensile creep at 1100 °C and creep stresses greater than or equal to 80 MPa ruptured after less than 1 h. Only the 40 MPa tensile creep test survived approximately 14 h. Conversely, all specimens subjected to compressive creep achieved a run-out (defined as 100 h), while accumulating large compressive creep strains. Monazite-containing specimens accumulated lower tensile creep strains than the control CMC, while the exact opposite was observed in compressive creep at 1100 °C. Yet all specimens tested in tensile and compressive creep at 900 °C accumulated small strains. In the case of both tensile creep [34,38] and compressive creep, percent strain accumulation was limited to 0.05.

#### 5.6.4 Retained Properties

Compression tests to failure were performed at 1100 °C on monazite-containing specimens that achieved run-out in 65 and 75 MPa creep tests at 1100 °C. A monazite-

containing specimen that achieved run-out in a 50 MPa creep test at 1100 °C was subjected to a tensile test to failure at 900 °C. Results of compression tests to failure are shown in Figure 53 together with the compressive stress-strain curve obtained for a virgin specimen. Retained compressive strength and stiffness of the specimens, which achieved creep run-out, are summarized in Table 7. It is seen that prior creep had no appreciable effect on compressive strength. Conversely, pre-crept specimens exhibited higher stiffness values.

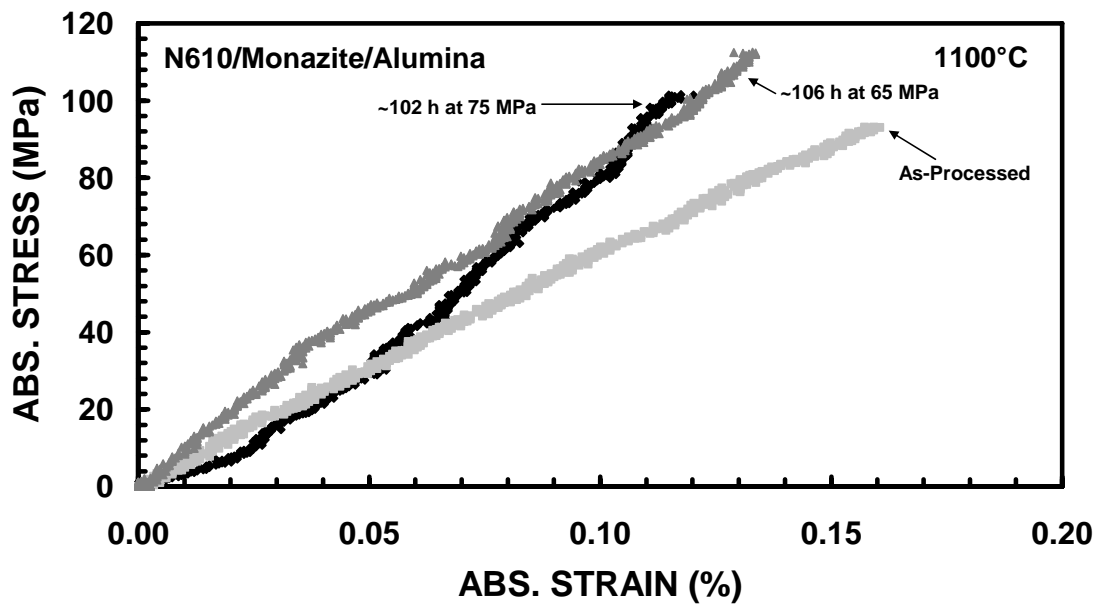


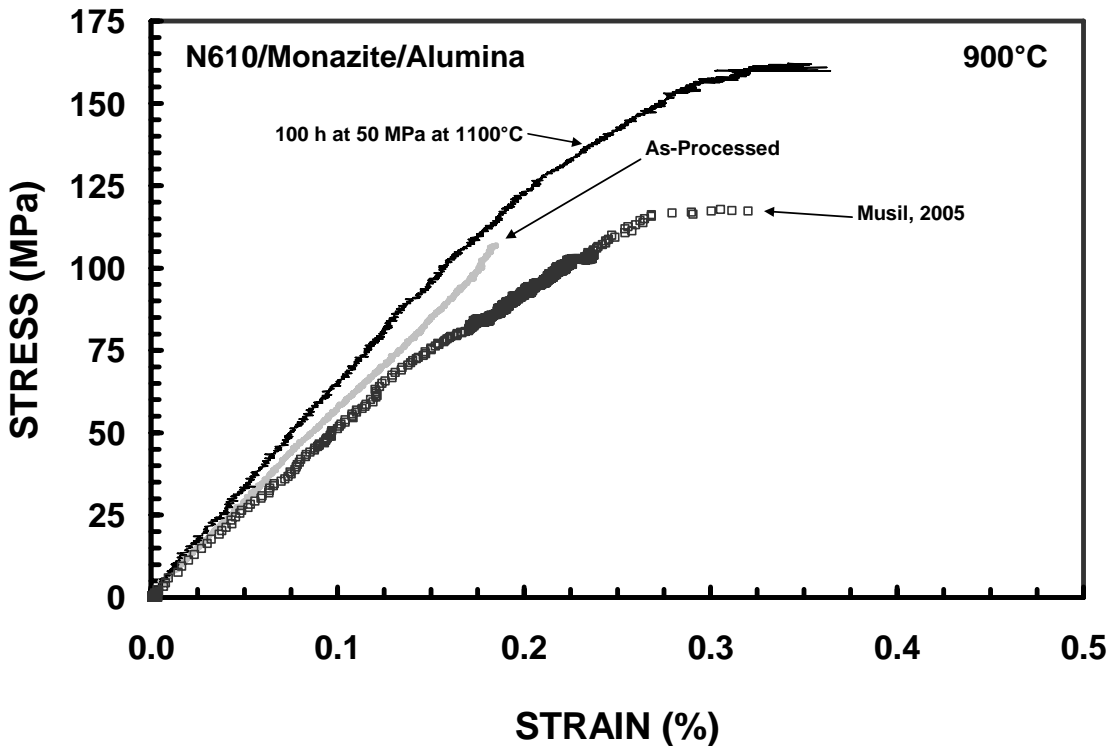
Figure 53. Effects of Prior Compressive Creep at 1100 °C on Compressive Stress-Strain Behavior of N610/Monazite/Alumina Ceramic Composite

Table 7. Retained Properties of N610/Monazite/Alumina Specimens Subjected to Prior Creep at 1100 °C

Specimen	Material	Testing Temperature °C	E (range) (MPa)	E (GPa)	UCS (MPa)	Strain <sub>UCS</sub> (%)	Strain <sub>f</sub> (%)	Stress <sub>f</sub> (MPa)
M1-3	N610/LaPO <sub>4</sub> /Al <sub>2</sub> O <sub>3</sub>	1100	5 to 15	63	97	0.16	N/A	N/A
M1-4*	N610/LaPO <sub>4</sub> /Al <sub>2</sub> O <sub>3</sub>	1100	10 to 20	72	102	0.12	N/A	N/A
M1-5*	N610/LaPO <sub>4</sub> /Al <sub>2</sub> O <sub>3</sub>	1100	10 to 20	89	113	0.13	N/A	N/A

\*: 100 hours of creep at 75 and 65 MPa respectively

As seen in Figure 54, the tensile test at 900 °C conducted on the specimen pre-crept at 50 MPa at 1100 °C also showed a significant increase in stiffness. The retained modulus was 68 GPa for this test, which was significantly higher than modulus value for the virgin material produced in this study (52 GPa) or that reported by Musil et al [34,38] (54 GPa). The pre-crept specimen also exhibited increased tensile strength.



**Figure 54.** Effects of Prior Compressive Creep at 1100 °C on Tensile Stress-Strain Behavior of N610/Monazite/Alumina Ceramic Composite

### 5.7 Microstructural Analysis of N610/Monazite/Alumina Panel M2

The following is an in-depth analysis of monazite-containing panel M2. The noticeably lower strength produced by specimens from this panel compared to strength values obtained for specimens from panel M1 caused much concern over processing. This discussion will begin with examination of the monotonic compression test results obtained for specimens from panel M2, followed by a detailed analysis of panel microstructure, and an analysis of the tensile properties exhibited by specimens from panel M2.

### 5.7.1 Stress-Strain Behavior.

Specimens from panel M2 were initially intended for compressive creep tests at 900 °C at varying stress levels, but only a 50 MPa creep test was successfully completed. Three additional specimens from panel M2 all failed during load-up. Two were intended for creep tests at 75 and 80 MPa. Specimens from panel M3 were subjected to the creep tests, but also failed during load-up. Figure 55, shows the stress-strain curves for specimens from panels M2 and M3. It is seen that specimens from these two panels produced similar values of stiffness and strength.

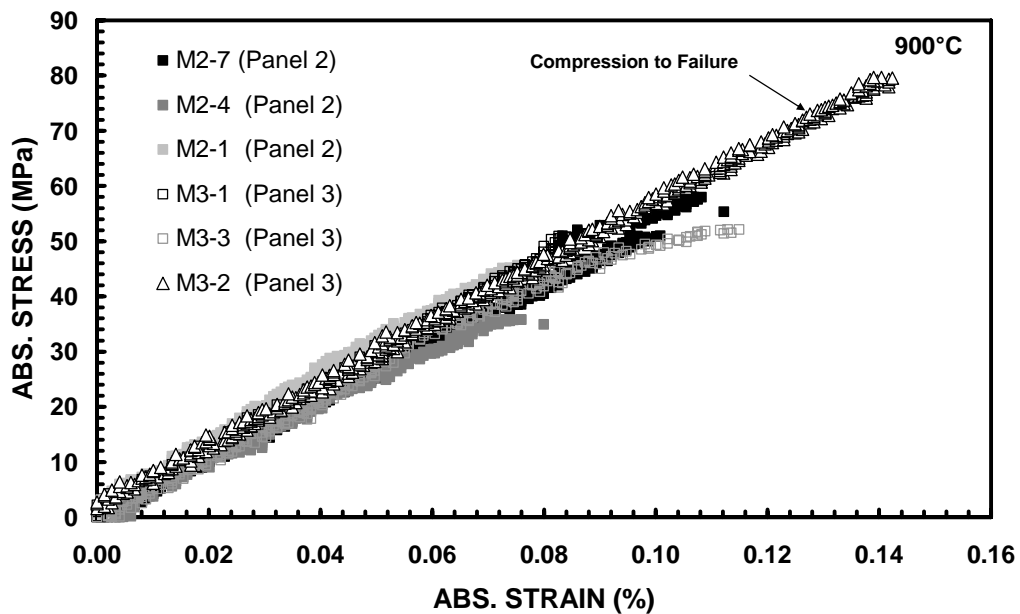


Figure 55. Compressive Stress-Strain Curves for N610/Monazite/Alumina Specimens from Panels M2 and M3 at 900 °C

Note that specimen M3-2 was tested in displacement control with displacement rate of 0.05 mm/s, while all other specimens were tested in load control at the rate of 2200 N/s, which corresponds to stress rates in the 18-32 MPa/s range. Table 8, presents

compressive properties of N610/monazite/alumina obtained in the course of this investigation.

Table 8. Compressive Properties of N610/Monazite/Alumina Ceramic Composites

Specimen	Panel	Testing Temperature °C	E (GPa)	UCS (MPa)	Strain <sub>UCS</sub> (%)
M1-1	Panel 1	900	47	110	N/A
M1-2	Panel 1	900	58	103	N/A
M1-3	Panel 1	1100	63	97	0.16
M2-1*	Panel 2	900	58	46	0.08
M2-4*	Panel 2	900	48	36	0.08
M2-7*	Panel 2	900	51	58	0.11
M3-1*	Panel 3	900	52	53	0.09
M3-2	Panel 3	900	51	80	0.14
M3-3*	Panel 3	900	48	52	0.11

\*: Failed during load-up for compressive creep test

Results in Table 8, demonstrate that while similar stiffness values were obtained for all panels, panels M2 and M3 produced considerably lower strength values than panel M1.

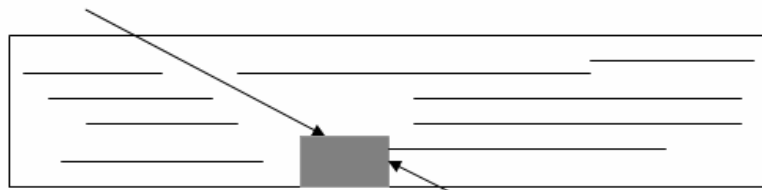
### 5.7.2 Panel M1 and Panel M2 Composite Microstructure.

Unusually low strength values obtained for panels M2 and M3 suggested that composite microstructure may be different from that of panel M1. This directed the investigation to the microstructure of panel M2. Microstructure of panel M1 was also examined for purposes of comparison.

Analysis of the microstructure began with examination of cross-sectional views of the virgin and tested specimens from panels M1 and M2. The two different cross-sectional views examined (schematically shown in Figure 56), will be referred to as parallel and perpendicular. The sections retrieved from the tested material were cut close to the area

of fracture, but also far enough away so that it exhibited no signs of damage visible to the naked eye.

Cross-section view:  
parallel



Cross-section view:  
perpendicular

Figure 56. Schematic of Specimen Showing the Type of Cuts made to View Cross-Sections

Note the specimens examined here were not necessarily subjected to the same test history. Specimens from panel M1 were tested in compressive creep at 65 MPa at 1100 °C. Specimens from panel M2 failed in monotonic compression (i.e. during load-up to an intended creep stress) at 900 °C.

After viewing the cross-sections under optical microscope, an obvious difference in microstructure was detected. In both the virgin and tested cross-sections of panel M2, thick bands of matrix were clearly visible between the fibrous layers (see Figure 57). These rich bands of matrix were also apparent in panel M3. Backscatter SEM images of cross-sections of panel M2 also show the matrix-rich regions as well as large areas void of matrix (see Figure 58). Panel M1 (see Figure 59) showed some matrix rich areas, however no matrix layers were observed akin to those seen in panels M2 and M3.

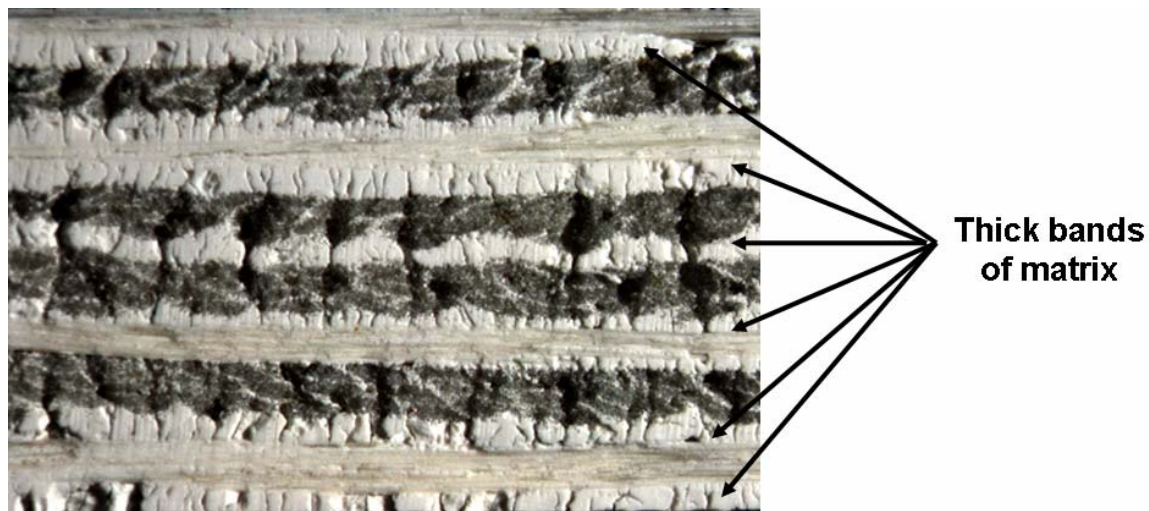


Figure 57. Parallel Cross-Sectional View of Virgin Specimen from Panel M2

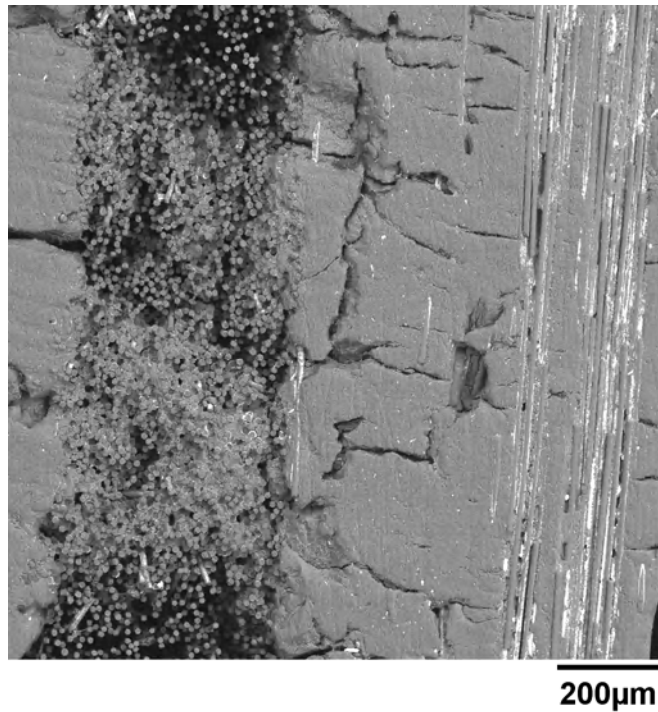


Figure 58. Backscatter SEM Image of Cross-Section of Panel M2 Showing Matrix-Rich Areas and Large Regions Void of Matrix Material in the 90° Fiber Layer. Bright White Areas on Both Fiber Layers are Monazite Coating.

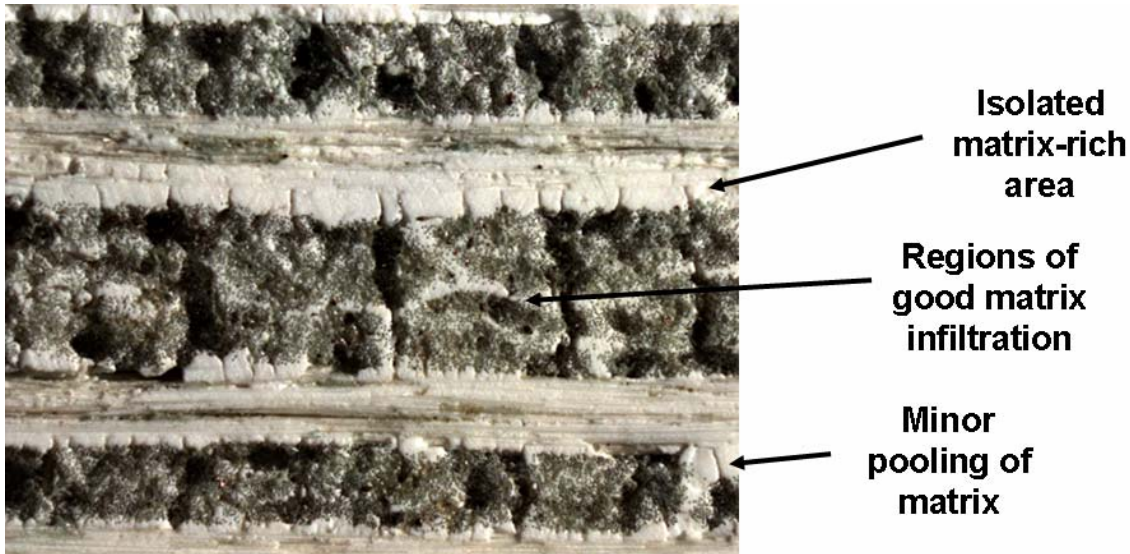


Figure 59. Parallel Cross-Sectional View of Virgin Specimen from Panel M1

The matrix-rich regions in panels M2 and M3 suggest a process control problem.

Furthermore, the matrix-rich layers appeared to be the cause of early failures and low strength observed for panels M2 and M3.

Confirmation that the matrix-rich areas caused early failures in panels M2 and M3 was received by examining optical micrographs and backscatter SEM images of the specimen fracture surfaces.

The fracture surfaces of specimens from panels M1, M2, and M3 displayed different failure mechanisms. Figure 60 shows the fracture surface of a specimen from panel M1. The cracks in this panel initiate between the laminae then propagate at  $\sim 45^\circ$  angle through the  $90^\circ$  fiber layer, where they finally self-arrest. Figure 61 shows a magnified view of the specimen shown in Figure 60. Three separate cracks can be seen initiating between the laminae, which then move along an inconsistent, angled path through the  $90^\circ$  fiber layer, and finally arrest. Also note the absence of matrix-rich areas.

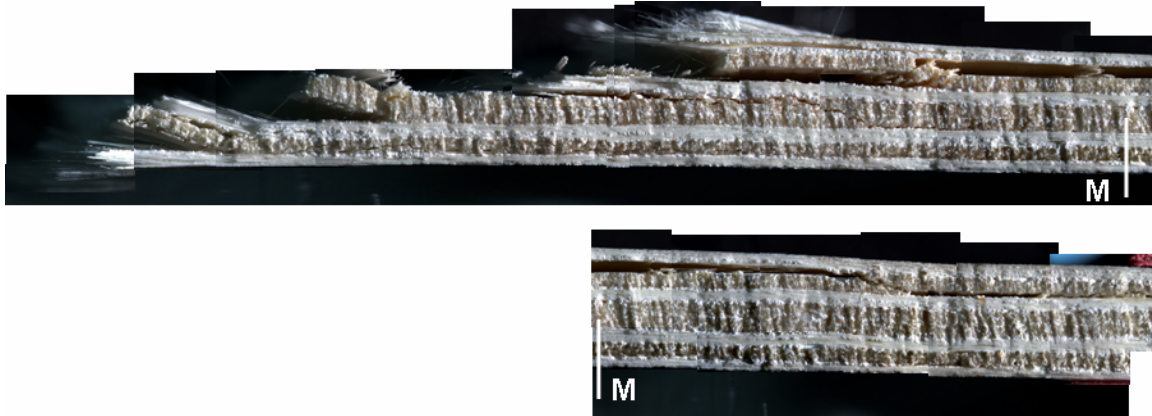


Figure 60. Propagation of Crack through a Specimen from Panel M1



Figure 61. Magnified View of a Fracture Surface from Panel M1 Showing Cracks Initiating and Self-arresting in 90° fiber layers

A much different failure mechanism was apparent in the specimens from panel M2 (see Figure 62). The cracks propagated directly through the 90° fiber layers. Cracks were continuous unlike the cracks observed in panel M1 and propagated for some time before dissipating their energy. The cracks in specimens appear to dissipate little energy

as they grow through the 90° fiber layer, furthermore little to no crack deflection is seen.

Figure 63 presents a magnified view of cracks in panel M2. A backscatter SEM image of the same fracture surface from panel M2 shows the crack and large areas devoid of matrix material (see Figure 64).



Figure 62. Crack Propagation through Fibrous 90° Layers of a Specimen from Panel M2.

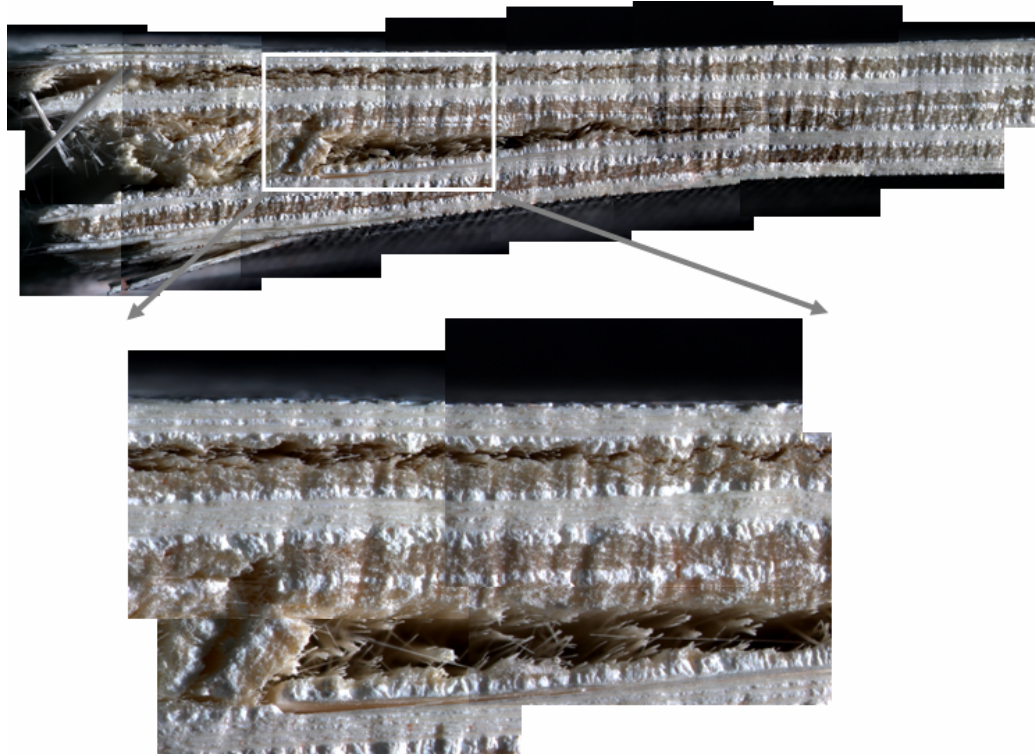


Figure 63. Magnified View of a Fracture Surface from Panel M2 Showing Cracks Propagating through 90° Fiber Layers. No Crack Deflection is Observed.

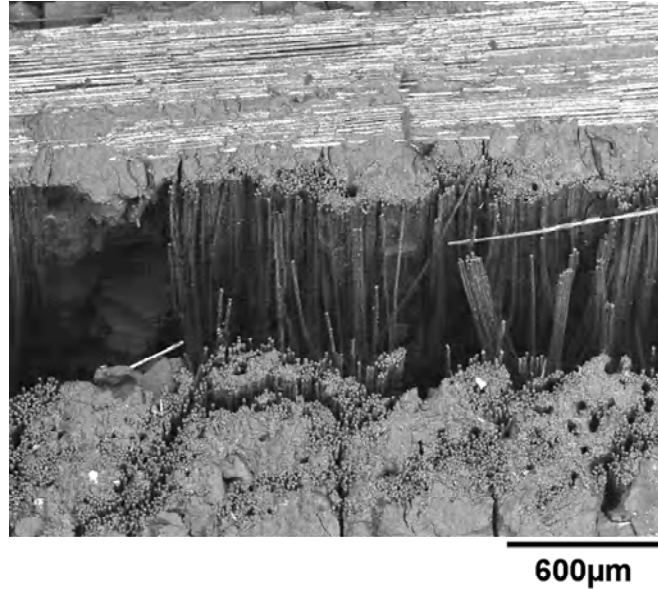


Figure 64. Backscatter SEM Image of Fracture Surface Shown in Figure 62.

Backscatter SEM images of crack fronts propagating through panels M1 and M2 highlight these different failure mechanisms and provide further confirmation that specimens from panel M2 had lower strength due to different microstructure. Figure 65 shows backscatter SEM images of representative crack propagation in specimens from panel M1 and panel M2. Figure 65(a) shows crack propagation in specimens from panel M1, while Figure 65(b) and (c) show crack propagation in panel M2. The cracks in specimens from panel M1 follow the monazite layer as expected; the weak fiber-matrix interface provides for crack deflection. Cracks in specimens from panel M2 either propagated through a thick matrix layer or proceeded through the areas of fibrous layers that were devoid of matrix material.

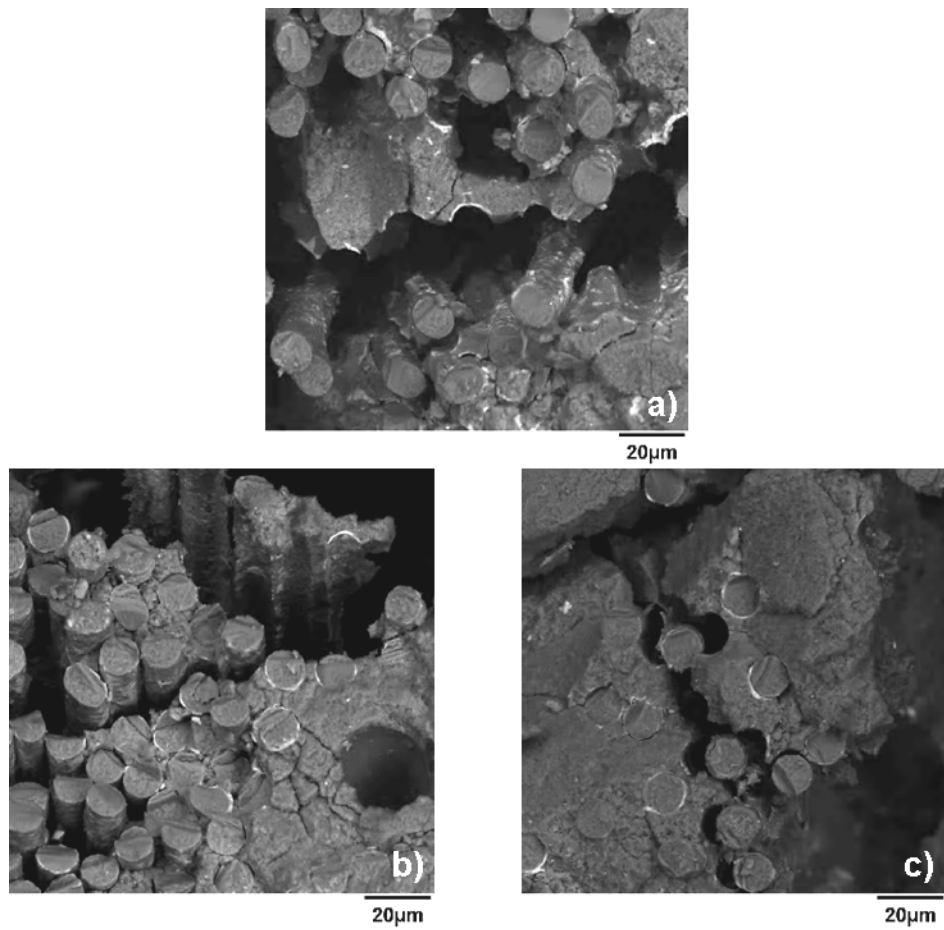


Figure 65. Backscatter SEM Images of Representative Crack Propagation in specimens from Panel M1 (a) and Panel M2 (b and c)

### 5.7.3 Montonic Tensile Behavior

Tensile behavior is a fiber dominated process. For that reason, tensile tests were conducted on specimens from panels M2 and M3 in order to ensure fibers were not degraded during processing. Fiber degradation could be ruled out if the panel exhibited tensile strength and stiffness consistent with those observed earlier.

Tensile tests were conducted at 900 °C on two virgin specimens from panel M3 and one virgin specimen from panel M2. Results are presented in Figure 66.

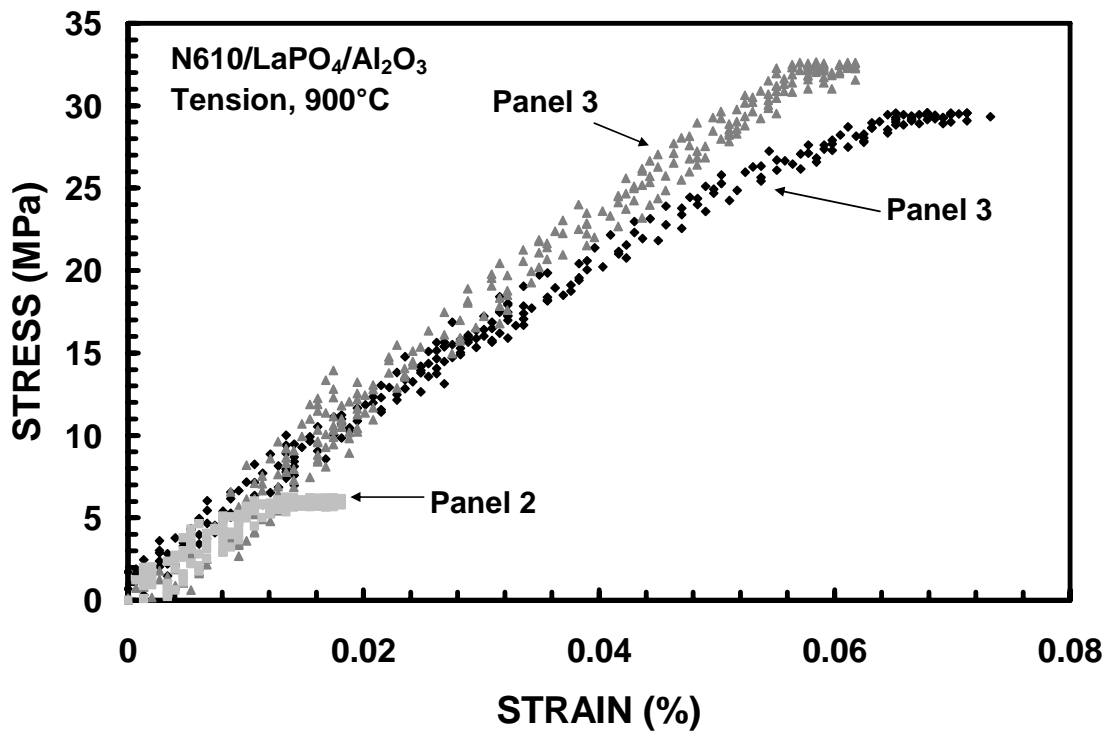


Figure 66. Tensile Stress-Strain Curves for N610/Monazite/Alumina Panels M2 and M3 at 900 °C

Note that the fiber volume fractions of panels M2 and M3 were approximately the same. All three tests experienced failure in the grip section. Failures in the grip section usually suggest that the ultimate strength was compromised. However, modulus value remains unaffected. The panels most likely experienced grip failure because the pressure applied by the wedge grips caused early cracks to form in the specimen before testing began. This assumption is reasonable, considering the low compressive strength of panels M2 and M3.

The tensile test conducted on a specimen from panel M2 did not provide sufficient data to accurately determine the elastic modulus. No other specimens from panel M2 could be tested, due to their excessive thickness the remaining specimens could not fit in

the testing machine. The two specimens from panel M3 produced the modulus values of 52 and 61 GPa. Recall that earlier tensile tests produced a modulus of 52 GPa. Furthermore, Musil et al [34,38] reported a very similar modulus of 54 GPa. This evidence suggests that the fibers were not degraded and did not compromise the strength of the specimens from panels M2 and M3.

### **5.8 Composite Microstructure**

Further microstructural analysis focused on specimens that had achieved a creep run-out at 1100 °C and were subsequently tested in compression to failure.

#### **5.8.1 Fracture Surfaces**

The following fracture surfaces were produced in compression tests to failure conducted on specimens that had achieved run-out in creep at 1100 °C. The fracture surfaces of the two pre-crept specimens exhibited some variation. Prior creep to have had little affect on the fracture surfaces. The fracture surfaces of the specimen pre-crept at 75 MPa at 1100 °C are shown in Figure 67. As is the case with all the monazite-containing specimens, the fiber pullout is apparent in Figure 68. The side views of the specimen seen Figure 68 reveal shear mode of failure (note that the fracture is oriented at an angle of 45° to the specimen axis).

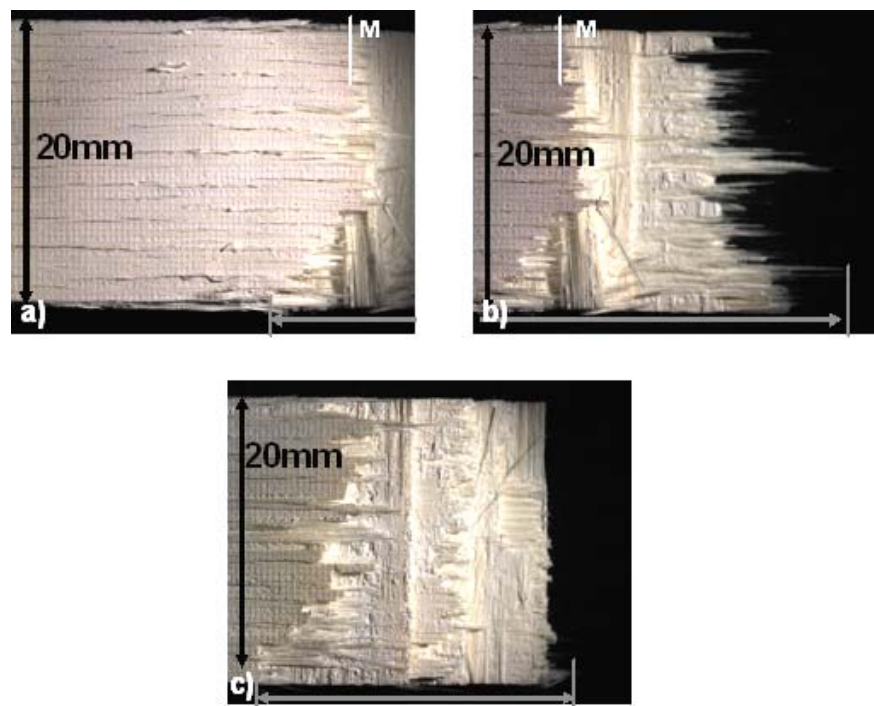


Figure 67. Fracture surfaces of N610/Monazite/Alumina Specimen Tested in Compression-to-Failure at 1100 °C after having achieved a Creep Run-Out at 75 MPa at 1100 °C

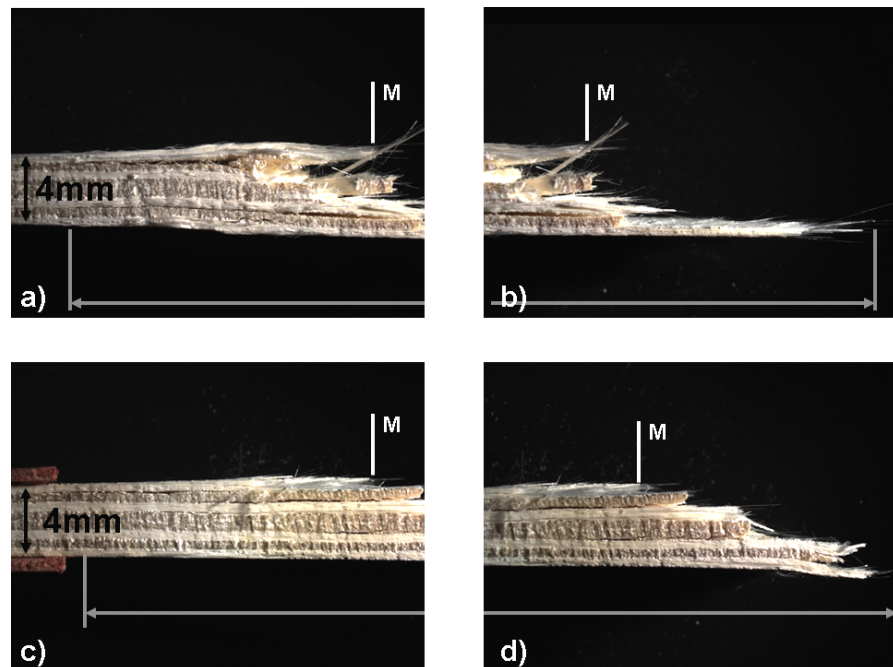


Figure 68. Side View of Fracture Surfaces of a N610/Monazite/Alumina Specimen Tested in Compression-to-Failure at 1100 °C after having achieved a Creep Run-Out at 75 MPa at 1100 °C

The N610/monazite/alumina specimen pre-crept at 65 MPa at 1100 °C did not show distinct layering after failing in monotonic compression, but produced damage of approximately the same length as those produced by the specimens pre-crept at 75 MPa at 1100 °C shown in Figure 69 and Figure 70. The N610/monazite/alumina specimens subjected to prior creep produced damage zones that were different from those produced by a virgin specimen. The damage zones visible on the side of the specimen were about 18mm to 26mm shorter.

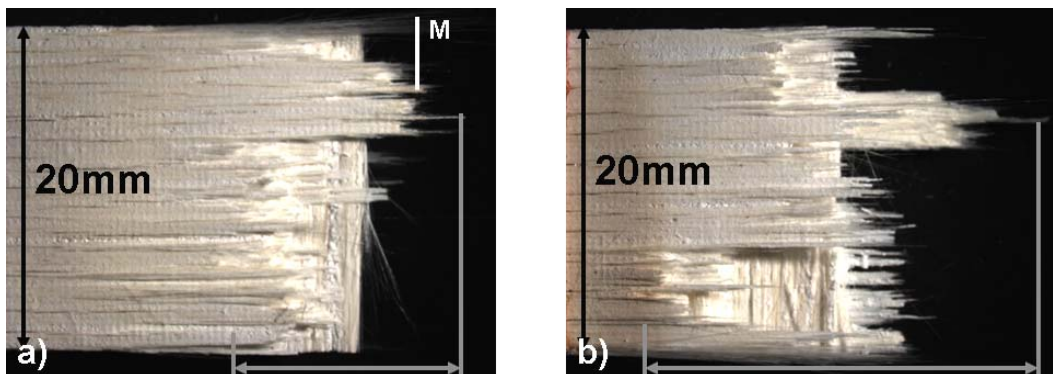


Figure 69. Fracture surfaces of N610/Monazite/Alumina Specimen Tested in Compression-t-Failure at 1100 °C after having achieved a Creep Run-Out at 65 MPa at 1100 °C

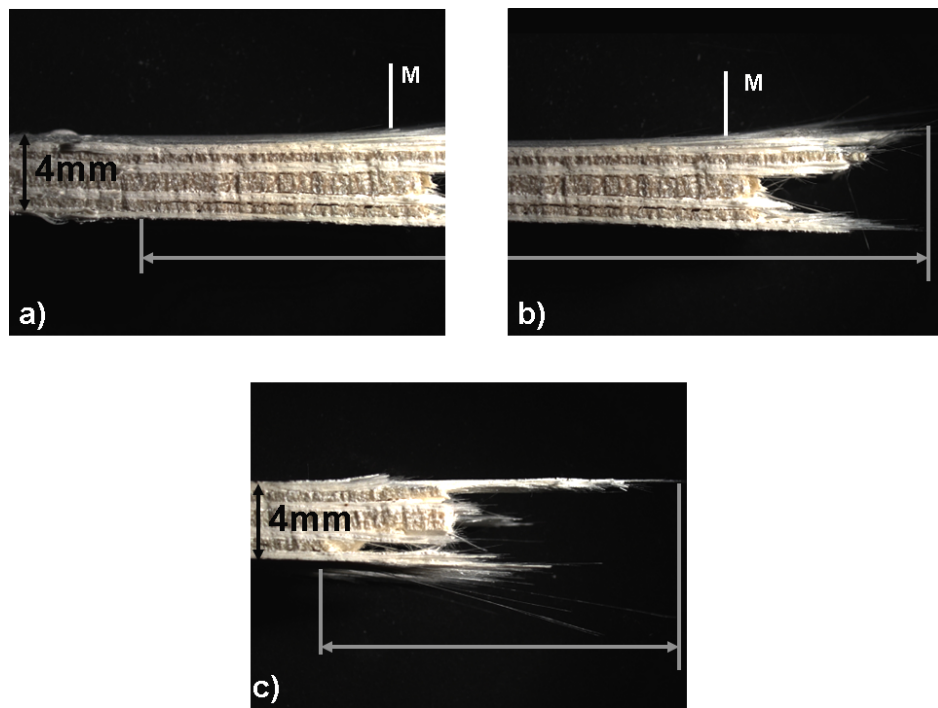


Figure 70. Side View of Fracture Surfaces of a N610/Monazite/Alumina Specimen Tested in Compression-to-Failure at 1100 °C after having achieved a Creep Run-Out at 65 MPa at 1100 °C

### 5.8.2 Microstructure of N610/Alumina Composite

The cross-sections of a N610/alumina specimen tested in compressive creep at 1100 °C were examined in order to determine whether the large accumulated creep strains were accompanied by extensive internal damage. Specimen cross-sections were cut in the manner shown in Figure 71. The sections were placed in a mold so that parallel cross-section (shaded area in Figure 71) could be observed under optical microscope. A sample of virgin material of the same orientation was added to the mold for comparison.

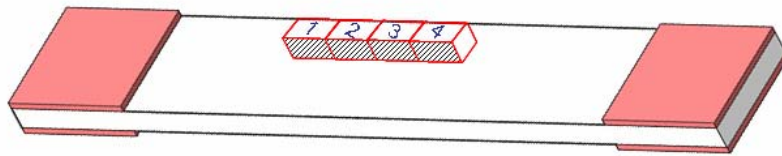


Figure 71. Schematic of Sections Removed from Specimen for Analysis

Results are presented in Figure 72, where the virgin material is on the far left, followed by sections 1, 2, 3, and 4 from the tested specimen. Figure 72 reveals no apparent difference in microstructure of any of the sections. The matrix cracks seen in Figure 72 are shrinkage cracks that occur during the sintering process. No differences in microstructure could be detected using the optical microscope at higher magnifications.

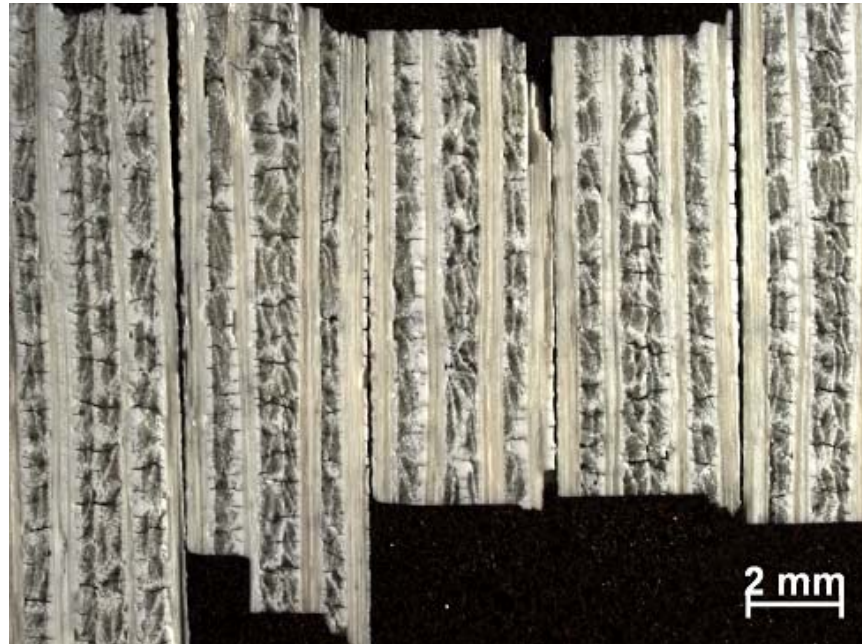


Figure 72. Micrograph of N610/Alumina Ceramic Composite. Virgin Material is on the Far Left Followed by Sections of the Specimen Tested in Compressive Creep at 1100 °C.

## VI. Observations and Conclusions

### 6.1 Observations

In a structural application, a material rarely experiences loads along the axial direction only. The off-axis tensile behavior of both N610/monazite/alumina and N610/alumina composites does not demonstrate high tensile strength required for most applications. The absence of coating appears to improve the off-axis tensile strength. The off-axis tensile creep resistance at elevated temperatures is anticipated to be undesirable, but may improve if fibers, such as N650 or N720, were used [40:1151].

The Nextel<sup>TM</sup>610 alumina composite exhibited high compressive strength at 900 and 1100 °C. However, when subjected to compressive creep at 1100 °C, the CMC accumulated high creep strain over a 100 h period. More creep-resistant fibers may be beneficial to future applications. Nextel<sup>TM</sup>650, a rare-earth doped alumina fiber, has been shown to have 100 times lower creep rate [41]. The addition of mullite to the Nextel<sup>TM</sup>720 alumina fiber provides it with superior creep resistance at temperatures above 1100 °C [20,37,42]. N650 and/or N720 may perform better at 1100 °C under the same compressive creep conditions. N610 fiber is better suited for tensile or compressive creep at 900 °C.

Process control is critical to the fabrication of CMCs. Although all panels were supposedly processed in the same manner, the microstructural investigation revealed that the processing of the monazite-containing panels was different. Apparent differences in microstructure caused early failures in compression. Poor infiltration of the matrix

material into the fibrous layers may have been caused by either fiber bridging due to the application of fiber coating or by high viscosity of the matrix slurry.

## ***6.2 Conclusions***

Results of the monotonic compression tests, as well as the results of compressive creep tests conducted at varying stress levels at 900 and 1100 °C revealed no significant effects of monazite coating in the mechanical response of the composite. In the case of tension, the addition of monazite resulted in considerable increase in tensile strength as well as in improved creep resistance [34,38]. Conversely, when subjected to monotonic compression and to compressive creep, response of the monazite-containing composite was similar to that of the control CMC. Fiber coating appears to be more beneficial for the tensile strength of a composite material than for its compressive strength. Fracture surfaces of the monazite-containing specimens show extensive fiber pullout and more distinctive planes of fracture suggesting delayed failure, which is one advantage offered by the monazite fiber coating under compression.

This investigation further confirmed the importance of processing in the life of a CMC. Microstructural investigation revealed that, the matrix material tended to collect between the laminae, which can either lead to fracture through the matrix rich regions themselves because they provide a weak path between the laminae or to fracture through the weak path within a poorly infiltrated 90° fiber layer. Unlike in the case of panel M1, cracks in panels M2 and M3 were not deflected and did not self-arrest.

## Bibliography

1. “3M Fiber Selection Guide,” in *3M Nextel Textile Notebook*. Product Brochure. St. Paul, MN: 3M Corporation, no date.
2. “3M Ceramic Fiber Typical Properties,” in *3M Nextel Textile Notebook*. Product Brochure. St. Paul, MN: 3M Corporation, no date.
3. *All You Wanted to Know About Electron Microscopy...but Didn't Dare to Ask*. Hillsboro, OR: FEI Company, no date. <http://www.feicompany.com>. 10 Feb 2006.
4. Antti, M-L, and Edgar Lara-Curzio. “Effect of Notches, Specimen Size, and Fiber Orientation on the Monotonic Tensile Behavior of Composites at Ambient and Elevated Temperatures,” in *25<sup>th</sup> Annual Conference on Composites Advanced Ceramics Materials, and Structures*: A. Ed. Mrityunjay Singh and Todd Jensen. Westerville, OH: The American Ceramic Society, 2001.
5. Antti, M-L, E. Lara-Curzio, and R. Warren. “Thermal Degradation of an Oxide Fibre (Nextel 720)/Aluminosilicate Composite,” *Journal of the European Ceramic Society*, 24: 565-578 (2004).
6. Baker, Alan, Stuart Dutton, and Donald Kelly. *Composite Materials for Aircraft Structures* (2<sup>nd</sup> Edition). Virginia: AIAA, 2004.
7. Boakye, E.E., R.S. Hay, P. Mogilevsky, and L.M. Douglas, “Monazite Coatings on Fibers: II, Coating without Strength Degradation,” *Journal of the American Ceramic Society*, 84 [12]: 2793-2801 (2001).
8. Buchanan, Dennis J., Reji John, and Larry P. Zawada. “Creep Rupture Behavior of  $\pm 45^\circ$  Oxide/Oxide Nextel<sup>TM</sup>720/AS Composite,” in *25<sup>th</sup> Annual Conference on Composites Advanced Ceramics Materials, and Structures*: A. Ed. Waltrud M. Kriven and Hau-Tay Lin. Westerville, OH: The American Ceramic Society, 2003.
9. Carrère, N., E. Martin, and J. Lamon. “The Influence of the Interphase and Associated Interfaces on the Deflection of Matrix Cracks in Ceramic Matrix Composites,” *Composites: Part A: Applied Science and Manufacturing*, 31: 1179-1190 (2000).
10. Chawla, K. K. *Composite Materials Science and Engineering* (2<sup>nd</sup> Edition). Boston: Kluwer Academic Publishers, 2003.
11. Cullum, Gail H. “Ceramic Matrix Composite Fabrication and Processing: Sol-Gel Infiltration,” in *Handbook on Continuous Fiber Reinforced Ceramic Matrix Composites*. Ed. Richard L. Lehman, Said K. El-Rahaiby, and John B. Wachtman, Jr. Westerville, OH: The American Ceramic Society, 1995.

12. Daniel, Isaac M. and Ori Ishai. *Engineering Mechanics of Composite Materials*. New York: Oxford University Press, 1994.
13. Davis, J.B., J.P.A. Lofvander, A.G. Evans. "Fiber Coating Concepts for Brittle Matrix Composites," *Journal of the American Ceramic Society*, **76** [5]: 1249-1257 (1993).
14. Davis, J.B., D.B. Marshall and P.E.D. Morgan. "Monazite-Containing Oxide/Oxide Composites," *Journal of the European Ceramic Society*, **20**: 583-87 (2000).
15. Davis, J.B., D.B. Marshall and P.E.D. Morgan. "Oxide Composites of Al<sub>2</sub>O<sub>3</sub> and LaPO<sub>4</sub>," *Journal of the European Ceramic Society*, **19**: 2421-26 (1999).
16. Davis, J.B., D.B. Marshall, R.M. Housely and P. E. D. Morgan. "Machinable Ceramics Containing Rare Earth Phosphates," *Journal of the American Ceramic Society*, **81** [8]: 2169-2175 (1998)
17. Deng, Zhen-Yan. "Effect of Different Fiber Orientations on Compressive Creep Behavior of SiC Fiber-Reinforced Mullite Matrix Composites," *Journal of the European Ceramic Society*, **19**: 2133-2144 (1999).
18. Evans, A.G., F.W. Zok, R.M. McMeeking, and Z.Z. Du. "Models of High-Temperature Environmentally-Assisted Embrittlement in Ceramic Matrix Composites," *Journal of the American Ceramic Society*, **79**: 2345-2352 (1996).
19. Harada, Yoshihisa, Takayuki Suzuki, Kazumi Hirano, and Yoshiharu Waku. "Ultra-high Temperature Compressive Creep Behavior of an In-Situ Al<sub>2</sub>O<sub>3</sub> Single-Crystal/YAG Eutectic Composite," *Journal of the European Ceramic Society*, **24**: 2215-2222 (2004).
20. Harlan, Lee B. *Creep-Rupture Behavior of an Oxide/Oxide Ceramic Matrix Composite at Elevated Temperatures in Air and Steam Environments*. MS thesis, AFIT/GA/ENY/05-M05. School of Engineering and Management, Air Force Institute of Technology (AU), Wright-Patterson AFB OH, March 2005.
21. Haslam, J.J., K.E. Berroth, and F.F. Lange. "Processing and Properties of an All-Oxide Composite with a Porous Matrix," *Journal of the European Ceramic Society*, **20**: 607-618 (2000).
22. Hasselman, D.P.H., and K.Y. Donaldson. "Thermal Conductivity of Continuous Fiber-Reinforced Ceramic Matrix Composites," in *Handbook on Continuous Fiber Reinforced Ceramic Matrix Composites*. Ed. Richard L. Lehman, Said K. El-Rahaiby, and John B. Wachtman, Jr. Westerville, OH: The American Ceramic Society, 1995.

23. Hay, R.S., E. Boakye, and M.D. Petry. "Effect of Coating Disposition Temperature on Monazite Coated Fiber," *Journal of the European Ceramic Society*, **20**:589-597 (2000).
24. Heredia, F.E., J.C. McNulty, F.W. Zok, and A.G. Evans, "Oxidation Embrittlement Probe for Ceramic-Matrix Composites," *Journal of American Ceramic Society*, **78** [8]: 2097-2100 (1995).
25. Kanazawa, C., S.M. Johnson, and J.R. Porter. "Monazite Coating Promotes Fiber Pullout," *Journal of the American Ceramic Society*. **80** [7]: Backcover (1997).
26. Keller, Kristen A. and Tai-II Mah. "Development of Monazite ( $\text{LaPO}_4$ ) Coated-Fiber Reinforced Oxide-Oxide Composites," in *High Temperature Ceramic Matrix Composites 5 – Proceedings of the 5<sup>th</sup> International Conference on High Temperature Ceramic Matrix Composites (HTCMC 5)*. Ed. By M. Singh, R.J. Kerans, E. Lara Curzio, and R. Naslain. Westerville, OH: The American Ceramic Society, 2004.
27. Keller, Kristen A., Tai-II Mah, Triplicane A. Parthasarathy, Emmanuel E. Boakye, Pavel Mogilevsky, and Michael K. Cinibulk. "Effectiveness of Monazite Coatings in Oxide/Oxide Composites after Long-Term Exposure at High Temperature," *Journal of the American Ceramic Society*, **86** [2]: 325-32 (2003).
28. Kerans, Ronald J., Randall S. Hay, Triplicane A. Parthasarathy, and Michael K. Cinibulk. "Interface Design for Oxidation-Resistant Ceramic Composite," *Journal of America Ceramic Society*, **85** [11]: 2599-2632 (2002).
29. Lee, Pengyuan and Toyohiko Yano. "The Influence of Fiber Coating Conditions on the Mechanical Properties of Alumina/Alumina Composites," *Composite Interfaces*, **11** [1]: 1-13 (2004).
30. Levi, Carlos G., James Y. Yang, Brian J. Dagleish, Frank W. Zok, and Anthony G. Evans. "Processing and Performance of an All-Oxide Ceramic Composite," *Journal of the American Ceramic Society*, **81** [8]: 2077-86 (1998).
31. Mackin, T.J., J.Y. Yang, C.G. Levi, and A.G. Evans. "Environmentally Compatible Double Coating Concepts for Sapphire Fiber Reinforced  $\gamma$ -TiAl," *Material Science and Engineering*, **A161**: 285-293 (1993).
32. Morgan, P.E.D., and D.B. Marshall. "Ceramic Composites of Monazite and Alumina," *Journal of the American Ceramic Society*, **78** [61]: 1553-1563 (1995).
33. Morgan, P.E.D., and D.B. Marshall. "Functional Interfaces for Oxide/Oxide Composites," *Material Science and Engineering*, **A162**: 15-25 (1993).

34. Musil, Sean S. *Characterization of Creep Behavior of Oxide/Oxide Composite with Monazite Coating at Elevated Temperature*. MS thesis, AFIT/GAE/ENY/05-M14. School of Engineering and Management, Air Force Institute of Technology (AU), Wright-Patterson AFB OH, March 2005.
35. Ohnabe, Hisaichi, Shoju Masaki, Masakazu Onozuka, Kaoru Miyahara, and Tadashi Sasa. "Potential Application of Ceramic Matrix Composites to Aero-Engine Components," *Composites: Part A: Applied Science and Manufacturing*, **30**: 489-496 (1999).
36. Parlier, Michel, and M.H. Ritti. "State of the Art and Perspectives for Oxide/Oxide Composites," *Aerospace Science and Technology*, **7**: 211-221 (2003).
37. Ruggles-Wrenn, M.B., S. Mall, C.A. Eber, and L.B. Harlan. "Effect of Steam Environment on High-Temperature Mechanical Behavior of Nextel<sup>TM</sup>720/Alumina (N720/A) Continuous Fiber Ceramic Composite," *Composites: Part A: Applied Science and Manufacturing*, in press (2006)
38. Ruggles-Wrenn, M.B., S.S. Musil, S. Mall, and K.A. Keller. "Creep Behavior of Nextel<sup>TM</sup>610/Monazite/Alumina Composite at Elevated Temperatures," *Composites Science and Technology*, in press (2006).
39. Saruhan, Bilge. *Oxide-Based Fiber-Reinforced Ceramic Matrix Composites: Principles and Materials*. Boston: Kluwer Academic Publishers, 2003.
40. Wilson, D.M. and L.R. Visser. "High Performance Oxide Fibers for Metal and Ceramic Composites," *Composites Part A: Applied Science and Manufacturing*, **32**: 1143-1153 (2001).
41. Wilson, D.M. and L.R. Visser. "Nextel<sup>TM</sup> 650 Ceramic Oxide Fiber: New Alumina-Based Fiber for High Temperature Composite Reinforcement," *Ceramic Engineering and Science Proceedings*, **21**: 363-373 (2000).
42. Tompkins, T.L. "Ceramic Oxide Fibers: Building Blocks for New Applications," *Ceramic Industry*, April 1995.
43. Zok, W. and Carlos G. Levi. "Mechanical Properties of Porous-Matrix Ceramic Composites," *Advanced Engineering Materials*, **3**, [1-2]: 15-23 (2001)

<b>REPORT DOCUMENTATION PAGE</b>				<i>Form Approved OMB No. 074-0188</i>
<p>The public reporting burden for this collection of information is estimated to average 1 hour per response, including the time for reviewing instructions, searching existing data sources, gathering and maintaining the data needed, and completing and reviewing the collection of information. Send comments regarding this burden estimate or any other aspect of the collection of information, including suggestions for reducing this burden to Department of Defense, Washington Headquarters Services, Directorate for Information Operations and Reports (0704-0188), 1215 Jefferson Davis Highway, Suite 1204, Arlington, VA 22202-4302. Respondents should be aware that notwithstanding any other provision of law, no person shall be subject to an penalty for failing to comply with a collection of information if it does not display a currently valid OMB control number.</p> <p><b>PLEASE DO NOT RETURN YOUR FORM TO THE ABOVE ADDRESS.</b></p>				
<b>1. REPORT DATE (DD-MM-YYYY)</b> 23 Mar 06		<b>2. REPORT TYPE</b> <b>Master's Thesis</b>		<b>3. DATES COVERED (From – To)</b> Aug 06 – Mar 06
Characterization of Compressive Creep Behavior of Oxide/Oxide Composite with Monazite Coating at Elevated Temperature			<b>4. TITLE AND SUBTITLE</b>  Characterization of Compressive Creep Behavior of Oxide/Oxide Composite with Monazite Coating at Elevated Temperature	<b>5a. CONTRACT NUMBER</b>  F4FB/EY5089J001
			<b>5b. GRANT NUMBER</b>  ENR# 2005-085	
			<b>5c. PROGRAM ELEMENT NUMBER</b>  5d. PROJECT NUMBER F4FB/EY5089J001	
<b>6. AUTHOR(S)</b>  Jackson, Patrick R., 2Lt., USAF			<b>5e. TASK NUMBER</b>  5f. WORK UNIT NUMBER	
			<b>7. PERFORMING ORGANIZATION NAMES(S) AND ADDRESS(S)</b>  Air Force Institute of Technology Graduate School of Engineering and Management (AFIT/EN) 2950 Hobson Way WPAFB OH 45433-7765	<b>8. PERFORMING ORGANIZATION REPORT NUMBER</b>  AFIT/GAE/ENY/06-M17
			<b>9. SPONSORING/MONITORING AGENCY NAME(S) AND ADDRESS(ES)</b>  AFRL/PRTC AFRL/MLLN AFRL/PRTC Attn: Dr. Joseph Zelina Attn: Dr. Ronald Kerans Attn: Dr. Ruth L. Sikorski 1950 5 <sup>th</sup> Street 2230 10 <sup>th</sup> Street 1950 5 <sup>th</sup> Street WPAFB OH 45433 DSN: 785-7487 WPAFB, OH 45433 DSN: 785-9823 WPAFB, OH 45433 DSN: 785-7268	<b>10. SPONSOR/MONITOR'S ACRONYM(S)</b>  11. SPONSOR/MONITOR'S REPORT NUMBER(S)
<b>12. DISTRIBUTION/AVAILABILITY STATEMENT</b>  APPROVED FOR PUBLIC RELEASE; DISTRIBUTION UNLIMITED.				
<b>13. SUPPLEMENTARY NOTES</b>				
<p><b>14. ABSTRACT</b>  The compressive creep behavior of a N610/monazite/alumina composite was investigated in this work. The composite consists of a porous alumina matrix reinforced with Nextel™610 fibers coated with monazite in a symmetric cross-ply (0°/90°/0°/90°)<sub>s</sub> orientation. Compressive stress-strain behavior was investigated as well. The addition of monazite coating resulted in ~ 35% loss in compressive strength at 900 °C and in ~45% loss in compressive strength at 1100 °C. Compressive creep behavior was examined at 900 and 1100°C for creep stresses ranging from 50 to 95 MPa. Primary and secondary creep regimes were observed at both temperatures. Minimum creep rate was reached in all tests. At 900 °C both monazite containing and control specimens produced creep strains ≤ 0.05%. Conversely, at 1100 °C creep strains were significant, approaching 9%, with monazite containing specimens accumulating larger creep strains at a given stress than the control samples. Creep strain rates were on the order of 10<sup>-7</sup> s<sup>-1</sup>. Creep run-out, defined as 100 h at creep stress, was achieved in all tests. The residual strength and modulus of specimens that achieved run-out at 1100 °C were characterized. Composite microstructure, as well as damage and failure mechanisms were investigated. Furthermore, effects of variation in microstructure on mechanical response were examined. While differences in processing and consequently the composite microstructure did not have a significant effect on tensile response of the CMC, effects on the compressive properties were dramatic. </p>				
<b>15. SUBJECT TERMS</b>  Monazite, Nextel 610 Fiber, Compression, Creep, Ceramic Matrix Composite (CMC)				
<b>16. SECURITY CLASSIFICATION OF:</b>  REPORT U		<b>17. LIMITATION OF ABSTRACT</b>  UU	<b>18. NUMBER OF PAGES</b>  111	<b>19a. NAME OF RESPONSIBLE PERSON</b>  Dr. Marina B. Ruggles-Wrenn (ENY) <b>19b. TELEPHONE NUMBER (Include area code)</b> (937) 255-3636, ext 4641; e-mail: marina.ruggles-wrenn @afit.edu

**Standard Form 298 (Rev: 8-98)**

Prescribed by ANSI Std Z39-18